Contributions to Geophysics and Geodesy

Volume 43, Issue 2

Contributions to Geophysics and Geodesy Vol. 43/2, 2013 (83–98)

Inverse problem for the gravimetric modeling of the crust-mantle density contrast

Robert TENZER[1]

[1]Institute of Geodesy and Geophysics, School of Geodesy and Geomatics
Wuhan University, 129 Luoyu Road, Wuhan, 430079 China
e-mail: rtenzer@sgg.whu.edu.cn

Abstract: The gravimetric inverse problem for finding the Moho density contrast is formulated in this study. The solution requires that the crust density structure and the Moho depths are a priori known, for instance, from results of seismic studies. The relation between the isostatic gravity data (i.e., the complete-crust stripped isostatic gravity disturbances) and the Moho density contrast is defined by means of the Fredholm integral equation of the first kind. The closed analytical solution of the integral equation is given. Alternative expressions for solving the inverse problem of isostasy are defined in frequency domain. The isostatic gravity data are computed utilizing methods for a spherical harmonic analysis and synthesis of the gravity field. For this purpose, we define various spherical functions, which define the crust density structures and the Moho interface globally.

Key words: crust, density contrast, gravity, isostasy, Moho interface

1. Introduction

In gravimetric studies of the isostasy, two basic concepts have been commonly adopted, assuming that the topographic mass surplus and the oceanic mass deficiency are compensated either by a variable thickness or density of compensation. In the Pratt–Hayford model, the isostatic mass balance is attained by a variable density of compensation (*Pratt, 1855; Hayford, 1909; Hayford and Bowie, 1912*). The Airy–Heiskanen model assumes that a depth of compensation is variable (*Airy, 1855; Heiskanen and Vening Meinesz, 1958*). *Vening Meinesz (1931)* modified the Airy–Heiskanen theory by introducing a regional instead of local compensation. *Moritz (1990)* generalized Vening Meinesz's inverse problem for a global isostatic compensation mechanism and applied a spherical approximation to the problem. *Sjöberg (2009)* formulated Moritz's problem, called herein the Vening

Meinesz-Moritz (VMM) problem of isostasy, as that of solving a non-linear Fredholm integral equation of the first kind. The seismic studies revealed that not only the Moho depth but also the Moho density contrast varies significantly (cf. *Geiss, 1987; Martinec, 1994; Kaban et al., 2003; Sjöberg and Bagherbandi, 2011*). The isostatic model should then be formulated based on assumption that both these quantities (i.e., Moho depth and density contrast) are variable. Following this concept, *Sjöberg and Bagherbandi (2011)* generalized the VMM problem. They developed and applied a least-squares approach, which combined seismic and gravity data in the isostatic inverse scheme for a simultaneous estimation of the Moho depth and density contrast. Later, they also presented and applied the non-isostatic correction to model for discrepancies between the isostatic and seismic models (cf. *Bagherbandi and Sjöberg, 2012*).

In gravimetric studies, the anomalous density structure not only within the crust but essentially within the whole lithosphere should be modeled (cf. e.g., *Kaban et al., 1999; Tenzer et al., 2009a, 2012c*). Moreover, large portion of the isostatic mass balance is attributed to variable sub-lithosphere mantle density structure, which has significant effect especially on a long-wavelength part of the isostatic gravity spectra and consequently on the respective Moho geometry (cf. *Sjöberg, 2009*). The gravitational field generated by all known anomalous density structures should thus be modeled and subsequently removed from observed gravity field prior to solving the gravimetric inverse problem.

In this study, the gravimetric inverse problem for finding the Moho density contrast is formulated using available models of the crust density structure and the Moho geometry. The solution is numerically realized in two steps. First, the gravimetric forward modeling is applied to compute the isostatic gravity data. These isostatic gravity data are then used to find the Moho density contrast based on solving the inverse problem of isostasy. In the absence of a reliable global mantle density model, the gravimetric problem is here formulated only for the crust mass balance.

2. Functional model

We formulate the functional model for finding the Moho density contrast (by means of Newton's volumetric integral) in the following form

$$\delta g^{cs}(r,\Omega) = -\mathrm{G} \iint\limits_{\Omega' \in \Phi} \Delta\rho^{\mathrm{c/m}}(\Omega') \int_{r'=\mathrm{R}-D(\Omega')}^{\mathrm{R}} \frac{\partial\, \ell^{-1}(r,\psi,\, r')}{\partial\, r}\, r'^2\, \mathrm{d}r'\mathrm{d}\Omega', \quad (1)$$

where $\mathrm{G} = 6.674 \times 10^{-11}$ m^3 kg^{-1} s^{-2} is Newton's gravitational constant; $\mathrm{R} = 6371 \times 10^3$ m is the Earth's mean radius (which approximates the geocentric radii of the geoid surface); ℓ is the Euclidean spatial distance of two points (r,Ω) and (r',Ω'), ψ is the respective spherical distance; and $\mathrm{d}\Omega' = \cos\phi' \mathrm{d}\phi' \mathrm{d}\lambda'$ is the infinitesimal surface element on the unit sphere. The 3-D position is defined in the system of spherical coordinates (r,Ω); where r is the spherical radius, and $\Omega = (\phi,\lambda)$ denotes the spherical direction with the spherical latitude ϕ and longitude λ. The full spatial angle is denoted as $\Phi = \{\Omega' = (\phi',\lambda') : \phi' \in [-\pi/2,\, \pi/2] \wedge \lambda' \in [0,\, 2\pi)\}$. The geocentric radius r of the observation surface point is computed as $r \cong \mathrm{R} + H$, where H is the topographic height. The Moho depths D' are taken relative to the sphere of radius R.

The unknown parameter in Eq. (1) is the laterally varying Moho density contrast $\Delta\rho^{\mathrm{c/m}}$, while it is assumed that the Moho depths D' are a priori known (for instance, from results of seismic surveys). The consolidated crust-stripped gravity disturbances δg^{cs} on the left-hand side of Eq. (1) are obtained from the gravity disturbances δg after applying the topographic and stripping gravity corrections of major known anomalous crust density structures. The global results of the topographic and crust components stripping gravity corrections and the step-wise consolidated crust-stripped gravity data were presented and discussed in *Tenzer et al. (2009b, 2012c)*. *Tenzer et al. (2011)* demonstrated that these gravity data have a correlation with the Moho geometry of 0.96; see also *Tenzer et al. (2009b)*.

The volumetric integral on the right-hand side of Eq. (1) is further divided into two constituents, which are defined for the average (constant) value of the Moho density contrast $\Delta\rho^{\mathrm{c/m}}$ and the correction term $\delta\Delta\rho^{\mathrm{c/m}}(\Omega') = \Delta\rho^{\mathrm{c/m}}(\Omega') - \Delta\rho^{\mathrm{c/m}}$. Hence,

$$\delta g^{cs}(r,\Omega) = -\,\mathrm{G}\,\Delta\rho^{\mathrm{c/m}} \iint\limits_{\Omega' \in \Phi} \int_{r'=\mathrm{R}-D(\Omega')}^{\mathrm{R}} \frac{\partial\, \ell^{-1}(r,\psi,\, r')}{\partial\, r}\, r'^2\, \mathrm{d}r'\mathrm{d}\Omega' -$$
$$-\,\mathrm{G} \iint\limits_{\Omega' \in \Phi} \delta\Delta\rho^{\mathrm{c/m}}(\Omega') \int_{r'=\mathrm{R}-D(\Omega')}^{\mathrm{R}} \frac{\partial\, \ell^{-1}(r,\psi,\, r')}{\partial\, r}\, r'^2\, \mathrm{d}r'\mathrm{d}\Omega'. \quad (1a)$$

The first constituent on the right-hand side of Eq. (1a) is the complete-crust stripped gravitational correction g^i. Subtracting this term from the consolidated crust-stripped gravity disturbances δg^{cs}, we arrive at

$$\delta g^m(r,\Omega) = -\,\mathrm{G}\iint\limits_{\Omega'\in\Phi} \delta\Delta\rho^{\mathrm{c/m}}(\Omega')\int_{r'=\mathrm{R}-D(\Omega')}^{\mathrm{R}} \frac{\partial\,\ell^{-1}(r,\psi,\,r')}{\partial\,r} r'^{\,2}\,\mathrm{d}r'\mathrm{d}\Omega', \quad (1\mathrm{b})$$

where $\delta g^m = \delta g^{cs} - g^i$ is the complete crust-stripped (relative to the upper mantle density) isostatic gravity disturbance. These isostatic gravity disturbances describe the gravity field generated by the regularized Earth of which topography is removed and the actual crust structures (beneath the geoid surface down to the Moho interface) are replaced by a homogeneous crust model of the adopted (constant) reference density of the upper(most) mantle (see *Tenzer et al., 2009a*). For the reference crust density of 2670 kg/m^3, the average value of the Moho density contrast $\Delta\rho^{\mathrm{c/m}}$ of 485 kg/m^3 can be recommended. This value was estimated based on minimizing the correlation between the gravity and Moho depth data (cf. *Tenzer et al., 2011*). It closely agrees with the value of 480 kg/m^3 adopted in the definition of the Preliminary Reference Earth Model (*Dziewonski and Anderson, 1981, Table 1*), which was derived based on results of seismic studies. The isostatic gravity disturbances δg^m on the right-hand side of Eq. (1b) are used as the input gravity data. The unknown parameters to be estimated are the correction terms $\delta\Delta\rho^{\mathrm{c/m}}$. The expressions for the gravimetric forward modeling of δg^{cs} and δg^m are reviewed in Appendices A and B, respectively. In Sections 3 and 4, we derive the solution to the gravimetric inverse problem (Eq. 1b) in spatial and spectral domains.

The definition of the complete crust-stripped isostatic gravity disturbances δg^m has analogy with the definition of the isostatic gravity data in the VMM model (see *Sjöberg, 2009*). The principal difference between these two definitions is in using the gravity disturbances instead of gravity anomalies. Moreover, the definition of δg^m is based on minimizing their correlation with the Moho geometry. *Tenzer and Bagherbandi (2012e)* reformulated the VMM inverse problem of isostasy for the isostatic gravity disturbances. They also demonstrated that the results obtained using the isostatic gravity disturbances have a better agreement with the seismic Moho model. *Sjöberg (2013)* summarized the definitions of the isostatic gravity field quantities for

the potential and gravity data types. He also gave a theoretical explanation to the numerical results of *Tenzer and Bagherbandi (2012e)*.

3. Spatial form

Let us first define the radial integral kernel function K as

$$K\left(r,\psi,r'\right) = -\int_{r'=\mathrm{R}-D(\Omega')}^{\mathrm{R}} \frac{\partial\,\ell^{-1}\left(r,\psi,\,r'\right)}{\partial\,r}\,r'^{2}\,\mathrm{d}r'. \tag{2}$$

Substitution from Eq. (2) back to Eq. (1b) then yields

$$\delta g^{m}\left(r,\Omega\right) \cong \mathrm{G}\iint\limits_{\Omega'\in\Phi} \delta\Delta\rho^{\mathrm{c/m}}\left(\Omega'\right)\;K\left(r,\psi,r'\right)\;\mathrm{d}\Omega'. \tag{3}$$

The expression in Eq. (3) is a Fredholm integral equation of the first kind. The closed analytical form of K reads (*Martinec, 1998, Eq. 3.54*)

$$K\left(r,\psi,r'\right) = \Bigg|\;\left[\left(r'^{2}+3r^{2}\right)\;t+\left(1-6t^{2}\right)\;r\,r'\right]\ell^{-1}\left(r,\psi,\,r'\right)+$$
$$+\;r\;(3t-1)\;\ln\left|\,r'-rt+\ell\left(r,\psi,\,r'\right)\right|\Bigg|_{r'=\mathrm{R}}^{\mathrm{R}-D'}, \tag{4}$$

where $D(\Omega')\equiv D'$; $t=\cos\psi$, and $\cos\psi=\sin\phi\sin\phi'+\cos\phi\cos\phi'\cos(\lambda'-\lambda)$.

Substitution of the integral limits in Eq. (4) yields

$$K\left(r,\psi,r'\right) = \left[\left(\mathrm{R}^{2}-2\mathrm{R}D'+D'^{2}+3r^{2}\right)\;t+r\;\left(1-6t^{2}\right)\;\;\left(\mathrm{R}-D'\right)\right]\times$$
$$\times\;\ell^{-1}\left(r,\psi,\,\mathrm{R}-D'\right)-\left[\left(\mathrm{R}^{2}+3r^{2}\right)\;t+\;r\mathrm{R}\;\left(1-6t^{2}\right)\right]\ell^{-1}\left(r,\psi,\,\mathrm{R}\right)+$$
$$+\;r\;(3t-1)\;\ln\left|\frac{\mathrm{R}-D'-r\,t+\ell\;\left(r,\psi,\,\mathrm{R}-D'\right)}{\mathrm{R}-r\,t+\ell\left(r,\psi,\,\mathrm{R}\right)}\right|, \tag{5}$$

where $\ell(r,\psi,\,\mathrm{R}-D')$ and $\ell(r,\psi,\,\mathrm{R})$ are given by

$$\ell\left(r,\psi,\,\mathrm{R}-D'\right)=\sqrt{r^{2}+\left(\mathrm{R}-D'\right)^{2}-2\,r\;\left(\mathrm{R}-D'\right)\;t}\quad, \tag{6}$$

$$\ell\left(r,\psi,\,\mathrm{R}\right)=\sqrt{r^{2}+\;\mathrm{R}^{2}-2\mathrm{R}\,r\,t}. \tag{7}$$

A weak singularity of Newton's integral kernel for $\psi \to 0$ can, for instance, be solved by finding the closed analytical solution for the inner-zone integration domain according to the procedure described by *Sjöberg (2009)*.

4. Spectral form

To define the solution of Eq. (1b) in spectral domain, the fundamental harmonic function ℓ^{-1} for the external convergence domain $r \geq \mathrm{R}$ (and $r' < \mathrm{R}$) is presented in the following form (e.g., *Heiskanen and Moritz, 1967*)

$$\ell^{-1}\left(r, \psi, r'\right) = \frac{1}{r}\sum_{n=0}^{\infty}\left(\frac{r'}{r}\right)^{n} P_n\left(t\right), \tag{8}$$

where $\mathrm{P_n}$ is the Legendre polynomial of degree n. From Eq. (8), the radial derivative of ℓ^{-1} is found to be

$$\frac{\partial\, \ell^{-1}\left(r, \psi, r'\right)}{\partial\, r} = -\frac{1}{r'^2}\sum_{n=0}^{\infty}\left(\frac{r'}{r}\right)^{n+2}\left(n+1\right)\ \mathrm{P_n}\left(t\right). \tag{9}$$

The substitution from Eq. (9) to Eq. (2) yields

$$K\left(r, \psi, r'\right) = \int_{r'=\mathrm{R}-D'}^{\mathrm{R}}\sum_{n=0}^{\infty}\left(\frac{r'}{r}\right)^{n+2}\left(n+1\right)\ \mathrm{P_n}\left(t\right)\,\mathrm{d}r'\,. \tag{10}$$

Solving the integral of K in Eq. (10), we get

$$K\left(r, \psi, r'\right) = r\sum_{n=0}^{\infty}\left(\frac{r'}{r}\right)^{n+3}\frac{n+1}{n+3}\mathrm{P_n}\left(t\right)\Bigg|_{r'=\mathrm{R}-D'}^{\mathrm{R}}. \tag{11}$$

Substituting for the integral limits in Eq. (11), we arrive at

$$\begin{aligned} K\left(r, \psi, r'\right) &= \sum_{n=0}^{\infty}\left(\frac{1}{r}\right)^{n+2}\frac{n+1}{n+3}\left[\mathrm{R}^{n+3} - \left(\mathrm{R}-D'\right)^{n+3}\right]\ \mathrm{P_n}\left(t\right) = \\ &= r\sum_{n=0}^{\infty}\left(\frac{\mathrm{R}}{r}\right)^{n+3}\frac{n+1}{n+3}\left[1 - \left(1-\frac{D'}{\mathrm{R}}\right)^{n+3}\right]\mathrm{P_n}\left(t\right). \end{aligned} \tag{12}$$

The term $(1 - D'/\mathrm{R})^{n+3}$ on the right-hand side of Eq. (12) is further expressed by means of the binomial theorem as follows

$$\left(1-\frac{D'}{\mathrm{R}}\right)^{n+3} \cong \sum_{k=0}^{n+3}\binom{n+3}{k}\frac{(-1)^k}{\mathrm{R}^k}D'^k. \tag{13}$$

After substituting from Eq. (13) to Eq. (12), the spectral representation of K is found to be

$$K\left(r,\psi,r'\right) = -r\sum_{n=0}^{\infty}\left(\frac{\mathrm{R}}{r}\right)^{n+3}\frac{n+1}{n+3}\sum_{k=1}^{n+3}\binom{n+3}{k}\frac{(-1)^k}{\mathrm{R}^k}D'^k\,\mathrm{P_n}\left(t\right). \tag{14}$$

From Eqs. (14) and (3), we have

$$\begin{aligned}\delta g^m\left(r,\Omega\right) = \mathrm{G}\sum_{n=0}^{\infty}\left(\frac{\mathrm{R}}{r}\right)^{n+2}(n+1)\iint\limits_{\Omega'\in\Phi}\delta\Delta\rho^{\mathrm{c/m}}\left(\Omega'\right)\,D'\left(\Omega'\right)\,\mathrm{P_n}\left(t\right)\,\mathrm{d}\Omega' - \\ -\mathrm{G}\,\mathrm{R}\sum_{n=0}^{\infty}\left(\frac{\mathrm{R}}{r}\right)^{n+2}\frac{n+1}{n+3}\sum_{k=2}^{n+3}\binom{n+3}{k}\frac{(-1)^k}{\mathrm{R}^k}\times \\ \times\iint\limits_{\Omega'\in\Phi}\delta\Delta\rho^{\mathrm{c/m}}\left(\Omega'\right)\,D'^k\left(\Omega'\right)\,\mathrm{P_n}\left(t\right)\,\mathrm{d}\Omega'.\end{aligned} \tag{15}$$

Since the expansion of the integral kernel K into a series of spherical functions converges uniformly for the external domain $r > \mathrm{R}$, the interchange of summation and integration in Eq. (15) was permitted.

We define the spherical Moho density-depth function M_n of degree n as

$$\begin{aligned}M_\mathrm{n}\left(\Omega\right) &= \frac{2n+1}{4\pi}\iint\limits_{\Omega'\in\Phi}\Delta\rho^{\mathrm{c/m}}\left(\Omega'\right)\,D\left(\Omega'\right)\,\mathrm{P_n}\left(t\right)\,\mathrm{d}\Omega' = \\ &= \sum_{\mathrm{m}=-\mathrm{n}}^{\mathrm{n}}M_{\mathrm{n,m}}\,\mathrm{Y_{n,m}}\left(\Omega\right).\end{aligned} \tag{16}$$

The corresponding higher-order terms $\left\{\, M_\mathrm{n}^{(\mathrm{k})} :\ k = 2,\,3,\,4,\,...\,\right\}$ read

$$\begin{aligned}M_\mathrm{n}^{(\mathrm{k})}\left(\Omega\right) &= \frac{2n+1}{4\pi}\iint\limits_{\Omega'\in\Phi}\Delta\rho^{\mathrm{c/m}}\left(\Omega'\right)\,D^k\left(\Omega'\right)\,\mathrm{P_n}\left(t\right)\,\mathrm{d}\Omega' = \\ &= \sum_{\mathrm{m}=-\mathrm{n}}^{\mathrm{n}}M_{\mathrm{n,m}}^{(\mathrm{k})}\,\mathrm{Y_{n,m}}\left(\Omega\right).\end{aligned} \tag{17}$$

The spherical coefficients $M_{\mathrm{n,m}}$ describe globally the Moho geometry scaled by the Moho density contrast. The same definitions are given for the correction term $\delta\Delta\rho^{\mathrm{c/m}}$. Hence

$$\delta M_{\mathrm{n}}^{(\mathrm{k})}\left(\Omega\right) = \frac{2n+1}{4\pi} \iint\limits_{\Omega'\in\Phi} \delta\Delta\rho^{\mathrm{c/m}}\left(\Omega'\right)\, D^{k}\left(\Omega'\right)\, \mathrm{P_n}\left(t\right)\, \mathrm{d}\Omega' =$$

$$= \sum_{\mathrm{m}=-\mathrm{n}}^{\mathrm{n}} \delta M_{\mathrm{n,m}}^{(\mathrm{k})}\, \mathrm{Y_{n,m}}\left(\Omega\right) \quad (k = 1,\, 2,\, 3,\, ...)\,. \tag{18}$$

Substitution from Eq. (18) back to Eq. (15) yields

$$\delta g^{m}\left(r,\Omega\right) = 4\pi\,\mathrm{G}\sum_{n=0}^{\infty}\left(\frac{\mathrm{R}}{r}\right)^{n+2}\frac{n+1}{2n+1}\sum_{\mathrm{m}=-\mathrm{n}}^{\mathrm{n}}\delta M_{\mathrm{n,m}}\,\mathrm{Y_{n,m}}\left(\Omega\right) -$$

$$- \;4\pi\,\mathrm{G\,R}\sum_{n=0}^{\infty}\left(\frac{\mathrm{R}}{r}\right)^{n+2}\frac{1}{2n+1}\frac{n+1}{n+3}\;\times$$

$$\times\sum_{k=2}^{n+3}\binom{n+3}{k}\frac{(-1)^{k}}{\mathrm{R}^{k}}\sum_{\mathrm{m}=-\mathrm{n}}^{\mathrm{n}}\delta M_{\mathrm{n,m}}^{(\mathrm{k})}\,\mathrm{Y_{n,m}}\left(\Omega\right). \tag{19}$$

To relate the spherical functions M_{n} and δM_{n} (and their higher-order terms) with spherical harmonics, which describe the Earth's gravity field, the constituents on the right-hand side of Eq. (19) are scaled by the geocentric gravitational constant $\mathrm{GM} = 3986005 \times 10^{8}\ \mathrm{m^{3}\ s^{-2}}$.

For the spherical approximation, the geocentric gravitational constant is given by (e.g., *Novák, 2010*)

$$\mathrm{GM} = \frac{4\pi}{3}\,\mathrm{G\,R}^{3}\,\bar{\rho}^{\mathrm{Earth}}, \tag{20}$$

where $\bar{\rho}^{\mathrm{Earth}} = 5500\ \mathrm{kg\ m^{-3}}$ is the Earth's mean mass density.

Combining Eqs. (19) and (20) and limiting the spectral resolution up to the maximum degree $\bar{n}$ of spherical harmonics, we arrive at

$$\delta g^{m}\left(r,\Omega\right) = -\frac{\mathrm{GM}}{\mathrm{R}^{2}}\sum_{n=0}^{\infty}\left(\frac{\mathrm{R}}{r}\right)^{n+2}\sum_{\mathrm{m}=-\mathrm{n}}^{\mathrm{n}}F_{\mathrm{n,m}}^{\delta M}\,\mathrm{Y_{n,m}}\left(\Omega\right). \tag{21}$$

The numerical coefficients $F_{\mathrm{n,m}}^{\delta M}$ in Eq. (21) read

$$F_{\mathrm{n,m}}^{\delta M} = \frac{1}{2n+1}\,\frac{3}{\bar{\rho}^{\mathrm{Earth}}}\frac{n+1}{n+3}\sum_{k=1}^{n+3}\binom{n+3}{k}\frac{(-1)^k}{\mathrm{R}^{k+1}}\delta M_{\mathrm{n,m}}^{(\mathrm{k})}\,. \tag{22}$$

The system of observation equations is formed for the correction terms $\delta\mathrm{M}_{\mathrm{n,m}}$ according to Eq. (21). The solution is carried out iteratively using, for instance, a condition of the convergence between results of two successive steps (k and k+1) as follows: $\left\|\delta\mathrm{M}_{\mathrm{n,m}}^{\mathrm{k+1}} - \delta\mathrm{M}_{\mathrm{n,m}}^{\mathrm{k}}\right\|_2 \leq c$, where c is a limit of convergence.

5. Discussion

Tenzer et al. (2012c) estimated that the relative errors in the computed values of δg^{cs} could reach as much as 10% mainly due to large uncertainties of currently available global crust structure models. Since these errors propagate proportionally to the Moho density contrast errors, the same relative uncertainties can be expected in the estimated values of the Moho density contrast especially over areas with variable crustal density structures. Large errors in the estimated values of the Moho density contrast are also expected due to uncertainties within the Moho geometry. Most of the errors in the Moho depth data are linearly related with the errors in the Moho density contrast. These errors propagate to the computed values of δg^{m} (and subsequently to $\delta\mathrm{M}_{\mathrm{n,m}}$) through uncertainties of the coefficients $D_{\mathrm{n,m}}$ (see Eq. B4), which are generated from discrete values of the Moho depths.

Grad et al. (2009), for instance, demonstrated that the Moho depths uncertainties (estimated based on processing the seismic data) under the Europe regionally exceed 10 km with the average error of more than 4 km. Much larger Moho depth uncertainties are expected over large parts of the world where the seismic data are absent or insufficient. Additional errors in the estimated Moho density contrast are due to the unmodeled gravitational signal from the variable density structures within the mantle lithosphere and sub-lithosphere mantle and eventually also from the geometry of the core-mantle interface. If known, the gravitational signal of anomalous density structures within the mantle should be treated in the same way as the crustal density structures. This can be done by applying the additional

gravity stripping correction of the anomalous mantle density structures. However, our current knowledge of spatial mantle density structures is restricted by the lack of reliable global data. A possible way how to partially overcome this problem is to remove the long-wavelength spherical harmonic terms from the isostatic gravity field. The principle of this procedure is based on finding the representative depth of gravity signal attributed to each spherical harmonic degree term (cf. *Eckhardt, 1983*). The spherical harmonics which have the depth below a certain limit (chosen, for instance, as the maximum Moho depth) are removed from the gravity field. Nonetheless, the complete subtraction of the gravity signal of mantle density structures using this procedure is still questionable, because there is hardly any unique spectral distinction between the long-wavelength gravity signal from the mantle and the expected higher-frequency signal of the Moho geometry.

Sjöberg and Bagherbandi (2011) applied the least-square method to simultaneously estimate the Moho depth and density contrast globally using the gravimetric and seismic models. *Tenzer et al. (2012a, 2012b)* used to same method to determine the Moho density contrast under oceans and continents.

6. Conclusions

The gravimetric inverse problem for finding the Moho density contrast was formulated by means of a Fredholm integral equation of the first kind. This method utilizes the direct functional relation between the isostatic gravity data and the Moho density contrast. The observation equations were described using the spatial and spectral representations of the integral kernel.

The gravimetric inverse model directly incorporated the seismic models into the solution. This was done through the gravimetric forward modeling of the gravity data corrected for the gravitational contributions of the topographic and anomalous density structures within the Earth's crust. Moreover, the information on the Moho depths was required in forming the observation equations, which define the relation between the isostatic gravity data and the Moho density contrast.

A principal theoretical advantage of this method is that the relation between the unknown (and sought) Moho density contrast and isostatic gravity disturbances can be readily reformulated for all known Earth's density

structures. The realistic estimation of the Moho density contrast is possible only when global crust (and essentially also mantle) density model is available with a sufficient accuracy.

References

Airy G. B., 1855: On the computations of the effect of the attraction of the mountain masses as disturbing the apparent astronomical latitude of stations in geodetic surveys. Trans. Roy. Soc. (London), ser. B, **145**.

Bagherbandi M., Sjöberg L. E., 2012: Non-isostatic effects on crustal thickness: A study using CRUST2.0 in Fennoscandia. Phys. Earth Planet. Inter., **200-201**, 37–44.

Dziewonski A. M., Anderson D. L., 1981: Preliminary earth reference model. Phys. Earth Planet. Inter., **25**, 297–356.

Eckhardt D. H., 1983: The gains of small circular, square and rectangular filters for surface waves on a sphere. Bull. Geod., **57**, 394–409.

Geiss E., 1987: A new compilation of crustal thickness data for the Mediterranean area. Ann. Geophys., **5B**, 623–630.

Grad M., Tiira T., 2009: ESC Working Group: The Moho depth map of the European Plate. Geophys. J. Int., **176**, 1, 279–292.

Hayford J. F., 1909: The figure of the earth and isostasy from measurements in the United States, USCGS.

Hayford J. F., Bowie W., 1912: The effect of topography and isostatic compensation upon the intensity of gravity. USCGS, Spec. Publ., No. 10.

Heiskanen W. A., Moritz H., 1967: Physical Geodesy. Freeman W. H., New York.

Heiskanen W. A., Vening Meinesz F. A., 1958: The Earth and its Gravity Field. McGraw-Hill Book Company, Inc.

Kaban M. K., Schwintzer P., Tikhotsky S. A., 1999: Global isostatic gravity model of the Earth. Geophys. J. Int., **136**, 519–536.

Kaban M. K., Schwintzer P., Artemieva I. M., Mooney W. D., 2003: Density of the continental roots: compositional and thermal contributions. Earth Planet. Sci. Lett., **209**, 53–69.

Martinec Z., 1994: The minimum depth of compensation of topographic masses. Geophys. J. Int., **117**, 545–554.

Martinec Z., 1998: Boundary value problems for gravimetric determination of a precise geoid. Lecture Notes in Earth Science, 73, Springer-Verlag.

Moritz H., 1990: The figure of the Earth. Wichmann H., Karlsruhe.

Novák P., 2010: High resolution constituents of the Earth gravitational field. Surv. Geoph., **31**, 1, 1–21.

Pratt J. H., 1855: On the attraction of the Himalaya Mountains and of the elevated regions beyond upon the plumb-line in India. Trans. Roy. Soc. (London), Ser. B, **145**.

Sjöberg L. E., 2009: Solving Vening Meinesz-Moritz inverse problem in isostasy. Geophys. J. Int., **179**, 3, 1527–1536.

Sjöberg L. E., Bagherbandi M., 2011: A method of estimating the Moho density contrast with a tentative application by EGM08 and CRUST2.0. Acta Geophys., **58**, 1–24.

Sjöberg L. E., 2013: On the isostatic gravity anomaly and disturbance and their applications to Vening Meinesz-Moritz gravimetric inverse problem. Geophys. J. Int., doi:10.1093/gji/ggt008.

Tenzer R., Hamayun, Vajda P., 2009a: Global maps of the CRUST2.0 crustal components stripped gravity disturbances. J. Geophys. Res., **114**, B, 05408.

Tenzer R., Hamayun, Vajda P., 2009b: A global correlation of the step-wise consolidated crust-stripped gravity field quantities with the topography, bathymetry, and the CRUST2.0 Moho boundary. Contrib. Geophys. Geod., **39**, 2, 133–147.

Tenzer R., Hamayun, Novák P., Gladkikh V., Vajda P., 2011: Global crust-mantle density contrast estimated from EGM2008, DTM2008, CRUST2.0, and ICE-5G. Pure Appl. Geophys.; doi:10.1007/s00024-011-0410-3.

Tenzer R., Bagherbandi M., Vajda P., 2012a: Depth-dependant density change within the continental upper mantle. Contrib. Geophys. Geod., **42**, 1, 1–13.

Tenzer R., Bagherbandi M., Gladkikh V., 2012b: Signature of the upper mantle density structure in the refined gravity data. Comput. Geosc., doi:10.1007/s10596-012-9298-y.

Tenzer R., Gladkikh V., Vajda P., Novák P., 2012c: Spatial and spectral analysis of refined gravity data for modelling the crust-mantle interface and mantle-lithosphere structure. Surv. Geophys., **33**, 5, 817–839.

Tenzer R., Novák P., Vajda P., Gladkikh V., Hamayun, 2012d: Spectral harmonic analysis and synthesis of Earth's crust gravity field. Comput. Geosc., doi:10.1007/s10596-011-9264-0.

Tenzer R., Bagherbandi M., 2012e: Reformulation of the Vening-Meinesz Moritz inverse problem of isostasy for isostatic gravity disturbances. Special Issue on Advances in Mathematical and Computational Geosciences, Int. J. Geosc. (in print).

Vening Meinesz F. A., 1931: Une nouvelle méthode pour la réduction isostatique régionale de l'intensité de la pesanteur. Bull. Geod., **29**, 33–51.

Appendix A: Consolidated crust-stripped gravity disturbances

The consolidated crust-stripped gravity disturbances δg^{cs} are obtained from the corresponding gravity disturbances δg after applying the topographic and crust density contrasts stripping gravity corrections. The computation is realized according to the following scheme (*Tenzer et al., 2012d*)

$$\delta g^{cs} = \delta g - g^t + g^b + g^i + g^s + g^c, \tag{A.1}$$

where g^t, g^b, g^i, g^s, and g^c are, respectively, the gravitational attractions generated by the topography and density contrasts of the ocean (bathymetry), ice, sediments and remaining anomalous density structures within the consolidated crystalline crust. The spectral representation of δg^{cs} reads (*ibid.*)

$$\delta g^{cs}\,(r,\Omega) = \frac{\mathrm{GM}}{\mathrm{R}^2}\sum_{n=0}^{\bar{n}}\sum_{m=-n}^{n}\left(\frac{\mathrm{R}}{r}\right)^{n+2}(n+1)\;\mathrm{T}^{\mathrm{cs}}_{\mathrm{n,m}}\,Y_{\mathrm{n,m}}\,(\Omega), \tag{A.2}$$

where $\mathrm{T}^{\mathrm{cs}}_{\mathrm{n,m}}$ are the coefficients of the consolidated crust-stripped disturbing potential. These coefficients are computed as follows

$$\mathrm{T}^{\mathrm{cs}}_{\mathrm{n,m}} = \mathrm{T}_{\mathrm{n,m}} - \mathrm{V}^{\mathrm{t}}_{\mathrm{n,m}} + \mathrm{V}^{\mathrm{b}}_{\mathrm{n,m}} + \mathrm{V}^{\mathrm{i}}_{\mathrm{n,m}} + \mathrm{V}^{\mathrm{s}}_{\mathrm{n,m}} + \mathrm{V}^{\mathrm{c}}_{\mathrm{n,m}}, \tag{A.3}$$

where $\mathrm{T}_{\mathrm{n,m}}$ are the (fully normalized) numerical coefficients which describe the disturbing potential T (i.e., difference between the Earth's gravity potential W and the normal gravity potential U); and $\mathrm{V}^{\mathrm{t}}_{\mathrm{n,m}}$, $\mathrm{V}^{\mathrm{b}}_{\mathrm{n,m}}$, $\mathrm{V}^{\mathrm{i}}_{\mathrm{n,m}}$, $\mathrm{V}^{\mathrm{s}}_{\mathrm{n,m}}$ and $\mathrm{V}^{\mathrm{c}}_{\mathrm{n,m}}$ are, respectively, the gravitational potential coefficients of topography and density contrasts of the ocean, ice, sediments and consolidated crystalline crust.

The coefficients $V_{\mathrm{n,m}}$ in Eq. (A.3) for the topography and crust density contrasts components read

$$V_{\mathrm{n,m}} = \frac{3}{2n+1}\frac{1}{\bar{\rho}^{\mathrm{Earth}}}\sum_{i=0}^{I}\left(Fl^{(\mathrm{i})}_{\mathrm{n,m}} - Fu^{(\mathrm{i})}_{\mathrm{n,m}}\right). \tag{A.4}$$

The numerical coefficients $\{Fl^{(\mathrm{i})}_{\mathrm{n,m}}, Fu^{(\mathrm{i})}_{\mathrm{n,m}} :\ i = 0,\ 1,\ ...,\ I\}$ are defined as follows

$$Fl^{(\mathrm{i})}_{\mathrm{n,m}} = \sum_{k=0}^{n+2}\binom{n+2}{k}\frac{(-1)^k}{k+1+i}\frac{L^{(k+1+i)}_{\mathrm{n,m}}}{\mathrm{R}^{\mathrm{k+1}}}, \tag{A.5}$$

and

$$Fu^{(\mathrm{i})}_{\mathrm{n,m}} = \sum_{k=0}^{n+2}\binom{n+2}{k}\frac{(-1)^k}{k+1+i}\frac{U^{(k+1+i)}_{\mathrm{n,m}}}{\mathrm{R}^{\mathrm{k+1}}}. \tag{A.6}$$

The terms $\sum_{\mathrm{m=-n}}^{\mathrm{n}} \mathrm{L_{n,m}\,Y_{n,m}}$ and $\sum_{\mathrm{m=-n}}^{\mathrm{n}} \mathrm{U_{n,m}\,Y_{n,m}}$ in Eqs. (A.5) and (A.6) define the spherical lower-bound and upper-bound laterally distributed radial density variation functions $\mathrm{L_n}$ and $\mathrm{U_n}$ of degree n. These spherical functions and their higher-order terms $\{L_{\mathrm{n}}^{(\mathrm{k+1+i})}, U_{\mathrm{n}}^{(\mathrm{k+1+i})} : \ k = 0, 1, \ldots ; \ i = 1, 2, \ldots, I\}$ are defined as follows

$$L_{\mathrm{n}}^{(k+1+i)}(\Omega) = \begin{cases} \frac{4\pi}{2n+1} \iint_{\Phi} \rho\,(D_U, \Omega')\ D_L^{k+1}\,(\Omega')\, P_n\,(t)\ \mathrm{d}\Omega' = \\ = \sum_{\mathrm{m=-n}}^{\mathrm{n}} L_{\mathrm{n,m}}^{(k+1)} \mathrm{Y_{n,m}}\,(\Omega) \qquad\qquad i = 0 \\ \\ \frac{4\pi}{2n+1} \iint_{\Phi} \beta\,(\Omega')\ a_i\,(\Omega')\ D_L^{k+1+i}\,(\Omega')\, P_n\,(t)\ \mathrm{d}\Omega' = \\ = \sum_{\mathrm{m=-n}}^{\mathrm{n}} L_{\mathrm{n,m}}^{(k+1+i)} \mathrm{Y_{n,m}}\,(\Omega) \qquad\qquad i = 1, 2, \ldots, I \end{cases} \tag{A.7}$$

and

$$U_{\mathrm{n}}^{(k+1+i)}(\Omega) = \begin{cases} \frac{4\pi}{2n+1} \iint_{\Phi} \rho\,(D_U, \Omega')\ D_U^{k+1}\,(\Omega')\, P_n\,(t)\ \mathrm{d}\Omega' = \\ = \sum_{\mathrm{m=-n}}^{\mathrm{n}} U_{\mathrm{n,m}}^{(k+1)} \mathrm{Y_{n,m}}\,(\Omega) \qquad\qquad i = 0 \\ \\ \frac{4\pi}{2n+1} \iint_{\Phi} \beta\,(\Omega')\ a_i\,(\Omega')\ D_U^{k+1+i}\,(\Omega')\, P_n\,(t)\ \mathrm{d}\Omega' = \\ = \sum_{\mathrm{m=-n}}^{\mathrm{n}} U_{\mathrm{n,m}}^{(k+1+i)} \mathrm{Y_{n,m}}\,(\Omega) \qquad\qquad i = 1, 2, \ldots, I \end{cases} \tag{A.8}$$

For a specific volumetric layer, the mass density ρ is either constant ρ, laterally-varying $\rho(\Omega')$ or – in the most general case – approximated by the laterally distributed radial density variation model using the following polynomial function (for each lateral column)

$$\rho\,(r', \Omega') = \rho\,(D_U, \Omega') + \beta\,(\Omega') \sum_{i=1}^{I} a_i\,(\Omega')\ (\mathrm{R} - r')^i,$$
$$\text{for} \quad \mathrm{R} - D_U\,(\Omega') \geq r' > \mathrm{R} - D_L\,(\Omega')\,, \tag{A.9}$$

where $\rho\,(D_U, \Omega')$ is the nominal value of the lateral density stipulated at the depth D_U of the upper bound of the volumetric mass layer. This density distribution model describes the radial density variation within the volumetric

mass layer at the location Ω'. Alternatively, when modeling the gravitational field of the anomalous mass density structures within the Earth's crust, the density contrast $\Delta\rho\,(r', \Omega')$ of the volumetric mass layer relative to the reference crustal density ρ^{c} is defined as

$$\Delta\rho\,(r', \Omega') = \rho^{\mathrm{c}} - \rho\,(r', \Omega') = \Delta\rho\,(D_U, \Omega') - \beta\,(\Omega') \sum_{i=1}^{I} a_i\,(\Omega') \;\left(\mathrm{R} - r'\right)^i,$$
$$\text{for} \quad \mathrm{R} - D_U\,(\Omega') \geq r' > \mathrm{R} - D_L\,(\Omega')\,, \tag{A.10}$$

where $\Delta\rho(D_U, \Omega')$ is the nominal value of the lateral density contrast.

The coefficients $\mathrm{L_{n,m}}$ and $\mathrm{U_{n,m}}$ combine the information on the geometry and density (or density contrast) distribution of volumetric layer. The coefficients $\mathrm{L_{n,m}}$ and $\mathrm{U_{n,m}}$ are generated to a certain degree of spherical harmonics using the discrete data of the spatial density distribution (i.e., typically provided by means of density, depth, and thickness data) of a particular structural component of the Earth's interior. Since the summation in Eq. (A.7) is finite, the validation of the expressions for computing the gravitational field quantities is not restricted to the outer space of the Brillouin sphere. We note that the expressions in Eqs. (A.7) and (A.8) can directly be used if the volumetric mass layer is distributed above and below the sphere of radius R with only one set of the coefficients $\mathrm{L_{n,m}}$ and $\mathrm{U_{n,m}}$ for describing the geometry of the lower and upper bounds of this volumetric layer.

Appendix B: Complete crust-stripped isostatic gravity disturbances

The computation of the complete crust-stripped isostatic gravity disturbances δg^m is based on subtracting the isostatic compensation attraction g^i(i.e., the complete-crust stripped gravity correction) from the consolidated crust-stripped gravity disturbances δg^{cs}. The upper bound of the homogeneous crust (density contrast) layer is given by the geoid surface while the lower bound is identical with the (model) Moho density interface. Then we have

$$\delta g^m\,(r, \Omega) = \delta g^{cs}\,(r, \Omega) - g^i =$$

$$= \frac{\mathrm{GM}}{\mathrm{R}} \sum_{n=0}^{\bar{n}} \sum_{m=-n}^{n} \left(\frac{\mathrm{R}}{r}\right)^{n+2} (n+1) \left(\mathrm{T}^{\mathrm{cs}}_{\mathrm{n,m}} - V^{\mathrm{i}}_{\mathrm{n,m}} \right) Y_{\mathrm{n,m}}(\Omega). \quad \text{(B.1)}$$

The potential coefficients $V^{\mathrm{i}}_{\mathrm{n,m}}$ are given by

$$V^{\mathrm{i}}_{\mathrm{n,m}} \cong \frac{3}{2n+1} \frac{\Delta\rho^{\mathrm{c/m}}}{\bar{\rho}^{\mathrm{Earth}}} F^{\mathrm{Moho}}_{\mathrm{n,m}}, \quad \text{(B.2)}$$

where $F^{\mathrm{Moho}}_{\mathrm{n,m}}$ read

$$F^{\mathrm{Moho}}_{\mathrm{n,m}} = \sum_{k=0}^{n+2} \binom{n+2}{k} \frac{(-1)^k}{k+1} \frac{D^{(k+1)}_{\mathrm{n,m}}}{\mathrm{R}^{\mathrm{k+1}}}. \quad \text{(B.3)}$$

The spherical Moho-depth function D_{n} of degree n reads

$$D_{\mathrm{n}}(\Omega) = \frac{2n+1}{4\pi} \iint_{\Phi} D(\Omega') \; P_n(\cos\psi) \; \mathrm{d}\Omega' = \sum_{\mathrm{m=-n}}^{\mathrm{n}} D_{\mathrm{n,m}} \, \mathrm{Y}_{\mathrm{n,m}}(\Omega), \quad \text{(B.4)}$$

and

$$D^{(\mathrm{i})}_{\mathrm{n}}(\Omega) = \frac{2n+1}{4\pi} \iint_{\Phi} D^{i}(\Omega') \; P_n(\cos\psi) \; \mathrm{d}\Omega' = \sum_{\mathrm{m=-n}}^{\mathrm{n}} D^{(\mathrm{i})}_{\mathrm{n,m}} \, \mathrm{Y}_{\mathrm{n,m}}(\Omega), \quad \text{(B.5)}$$

where D is the Moho depth, and $D_{\mathrm{n,m}}$ are the coefficients of the global Moho model.

Contributions to Geophysics and Geodesy Vol. 43/2, 2013 (99–123)

Solving ill-posed magnetic inverse problem using a Parameterized Trust-Region Sub-problem

Maha ABDELAZEEM Mohamed[1]

[1] National Research Institute of Astronomy and Geophysics (NRIAG)
Helwan, Cairo, Egypt; e-mail: maazeem03@yahoo.com

Abstract: The aim of this paper is to find a plausible and stable solution for the inverse geophysical magnetic problem. Most of the inverse problems in geophysics are considered as ill-posed ones. This is not necessarily due to complex geological situations, but it may arise because of ill-conditioned kernel matrix. To deal with such ill-conditioned matrix, one may truncate the most ill part as in truncated singular value decomposition method (TSVD). In such a method, the question will be where to truncate? In this paper, for comparison, we first try the adaptive pruning algorithm for the discrete L-curve criterion to estimate the regularization parameter for TSVD method. Linear constraints have been added to the ill-conditioned matrix. The same problem is then solved using a global optimizing and regularizing technique based on Parameterized Trust Region Sub-problem (PTRS). The criteria of such technique are to choose a trusted region of the solutions and then to find the satisfying minimum to the objective function. The ambiguity is controlled mainly by proper choosing the trust region. To overcome the natural decay in kernel with depth, a specific depth weighting function is used. A Matlab-based inversion code is implemented and tested on two synthetic total magnetic fields contaminated with different levels of noise to simulate natural fields. The results of PTRS are compared with those of TSVD with adaptive pruning L-curve. Such a comparison proves the high stability of the PTRS method in dealing with potential field problems. The capability of such technique has been further tested by applying it to real data from Saudi Arabia and Italy.

Key words: inversion, ill-posed problem, ill-conditioned, Tikhonov regularization, Trust Region Sub-problem, TRS, Parameterized Trust Region Sub-problem, PTRS, depth weighting

1. Introduction

Inverse potential field problems, which we aim to solve here, represent typical ill-posed problems. This is due to the invariable contamination of data with

noise and such data is acquired in a limited number of observation points. These problems are said to be ill-posed or ill-conditioned, which means that the solutions are non-unique and unstable. Most literature reformulated such problems into a system of equations having better condition by adding different kinds of constraints to control the results as much as possible. For example, *Last and Kubik (1983)* imposed a condition that the volume of the causative body to be minimum and have a definite upper boundary for the unknown physical property. *Guillen and Menichetti (1984)* constrained the source to have minimal moment of inertia with respect to the center of gravity or to an axis of given dip passing through it. *Abdelazeem et al. (1998)* used a quadratic programming with both equality and inequality constraints to invert the gravity anomalies.

We investigated the synthetic models of *Last and Kubik (1983)* carefully and it is found that all data kernel matrices have low condition numbers. When the same subsurface models were taken in different numbers of rows and/or columns, their technique failed to invert; this is because such matrices have higher condition numbers than the original ones. Such cases can now be classified as ill-posed/ill-conditioned problems. Thence, it is obvious that in ill-posed problems, a proper solution will not be achieved even when using constraints if traditional techniques are utilized.

Therefore, to solve these problems we need special strategies known as regularization techniques. To regularize such a problem, at first, the ill-posedness of the problem has to be tested by calculating the condition number of the kernel matrix. The higher the condition number, the higher the ill-posedness of the problem. Secondly, any conventional regularization tool can be used in order to have acceptable trusted solutions (*Tikhonov and Arsenin, 1977*). Recently, such a problem is tackled using different forms (*Zhdanov, 1993*). *Tezkan et al. (2000)* used regularization with conjugate gradient to invert radiomagnetotelluric field to delineate industrial and domestic waste sites in Germany. *Portniaguine and Zhdanov (2002)* developed a regularization technique, based on the traditional Tikhonov regularization theory, by using a weighted model parameters based on sensitivity analysis and fine focused inversion and applied it to 3-D magnetic problems. However, they didn't mention what will be the case if data were contaminated with high levels of noise. *Fedi et al. (2005)* presented a new tool, the Depth Resolution Plot (DRP) for regularizing inverse potential

field problems. *Silva et al. (2007)* used the entropic regularization to estimate the density contrast of elongated prismatic cell with known tops and bottoms. *Abdelazeem et al. (2007)* used TSVD with adaptive pruning L-curve technique to invert the ill-posed gravity problem. *Blaschek et al. (2008)* used a new regularization scheme based on the Minimum Gradient Support (MGS) and active constraint balancing to invert the induced polarization data. *Ardalan et al. (2011)* used an alternative method for density variation modeling of the crust from constrained inversion of the terrestrial gravity data. *Pašteka et al. (2012)* used Tikhonov regularization for stable downward continuation of geophysical potential fields.

To summarize, the magnetic inverse problem is, intrinsically, non-unique and its numerical solution is unstable. This means that any small perturbation in the data (noise) causes large variation in the solution. Such problem is a highly ill-posed one. We applied (*Grodzevich, 2004*) regularization technique for formulating generalized solutions that are stable even with perturbed data. The method is an extension to the traditional trust-region approach combined with L-curve. The regularization parameter is deduced during inversion. The radius of the trust region is changed during iteration; to improve the solution. The method has been applied to invert two synthetic examples with different levels of noise in order to test its stability in highly perturbed data condition. The method is compared to TSVD with adaptive pruning L-curve (*Hansen et al., 2007*), which was applied successfully to invert the gravity inverse problem (*Abdelazeem, 2007*). Finally, the method has been applied to a total field anomaly from Saudi Arabia and a vertical gradient field from Italy in order to test its validity.

2. Ill-posed problem

To clarify the source of ill-posedness of our problem and why the regular inversion tools are not the optimum choice, let us begin from the initial description of the magnetic field. The magnetic field is expressed (*Blakley, 1996*) in an integral equation of the form

$$f(P) = \int_R s(Q)\,\psi(P,Q)\,\mathrm{d}v \tag{1}$$

where $f(P)$ is the magnetic field at P (the observation point), $s(Q)$ describes the magnetization at Q, $\psi(P,Q)$ is a function that depends on the geometric placement of observation point P and source point Q. R is the volume/area occupied by the causative source and Q is the point of integration within R. This equation is known as Fredholm integral of the first kind (*Morse and Feshbach, 1953*). Now to study this problem, the subsurface domain is divided into a set of M rectangular prismatic cells. Each cell has a constant susceptibility of s value, assuming that there is no remnant magnetization and the demagnetization effect is negligible. Thus, only the induced magnetization is considered. Using the discrete quadrature rule for discretizing such integration (*Baker, 1977*), the above integral equation is approximated as follows:

$$\int_a^b \int_c^d \psi(P,Q)\, s(Q) \mathrm{d}P \mathrm{d}Q \cong \sum_{i=1}^{N} \sum_{j=1}^{M} w_i w_j^{'}\, \psi(P_i, Q_j) s(Q_j) = f(p_i), \tag{2}$$

where $s(Q_j)$, $\psi(P_i, Q_j)$ and $f(P_i)$ are the approximation of *s(Q), ψ(P,Q)* and $f(P)$ respectively, $w_i = \frac{b-a}{N}$ and $w_j^{'} = \frac{d-c}{M}$, where $[a,b]$ is the outer integral interval, $[c,d]$ is the inner integral interval, N is the number of data points and M is the number of prisms. When equation (2) is written in matrix notation, one obtains the system: $G_{N\times M} s_M = D_N$, where $G_{N\times M}$ is an $N \times M$ matrix, which quantifies the effect of the j^{th} cell on the i^{th} data point. The elements of G, s and D are given by $g_{ij} = w_i w_j^{'} \psi_{ij}(P_i, Q_j)$, $D_i = f(P_i)$,$s_j = s(Q_j)$, i=1,2,., N and j=1,2,.., M. As data is always contaminated with noise, we will consider the measured data $\overline{D} = D + \eta$, where η is a random vector of uncorrelated noise. Then, the problem to be solved is:

$$\min_{\mathrm{s}} \left\| Gs - \overline{D} \right\|^2 \tag{3}$$

Using a reasonably accurate discretization to obtain G will result in a highly ill-conditioned matrix with a singular spectrum that decays to zero gradually, a large cluster of small singular values, and high-frequency components of the singular vectors associated with small singular values (*Rojas and Sorensen, 2002*). If, in addition, the Discrete Picard Condition (*Hansen, 1990*) holds, the expansion coefficients of the exact data vector D will decay to zero faster than the singular values of G, while the expansion coefficients

of the noise vector η remains constant. Therefore, the solutions corresponding to small singular values are magnified by the noise. As a consequence of the ill conditioning of the matrix G and the presence of noise in data, applying standard numerical methods such as those discussed in *Dennis and Schnabel (1983)* to Eq. 3 will produce meaningless solutions with very large norm. Therefore, to solve these problems, we need special techniques known as regularization or smoothing methods. Such methods focus on recovering information about the desired solution from the solution of a better conditioned problem that is related to the problem with noisy data but incorporates additional information about the desired solution. The formulation of the new problem involves a special parameter (the regularization parameter), used to control the effect of the noise on the solution. The conditioning of the new problem depends on the choice of the regularization parameter. Good surveys on regularization methods can be found for example in (*Zhdanov, 1993* and *Hansen, 1998*).

In the next two sections, we will give a brief introduction to the concepts of regularization strategies employed for solving our ill-posed problem.

3. Method

In order to introduce the method applied in this paper, we have to mention some essential concepts used. Firstly, the classical Tikhonov regularization form, which is the base for most regularizing tools. Secondly, the trust region sub-problem (TRS) form, which is the base also for many regularizing tools and for the main tool used here. Thirdly, the L-curve criterion which is sometimes implemented with other tools to choose the optimum regularized solution. Lastly, we will mention the Picard condition and its use in testing the ill-posedness of the problem. Then, the main tool used, Parameterized Trust Region Sub-problem, PTRS method (*Grodzevich, 2004*) is presented. Another method is presented to be applied here, in order to clarify the strength of the PTRS, named TSVD with adaptive pruning L-curve (*Hansen et al., 2007*).

3.1. Tikhonov and TRS forms

The classical Tikhonov regularization approach is one of the most popular regularization approaches for solving discrete forms of ill-conditioned linear

algebraic system given in Eq. 3. Tikhonov regularization problem takes the form

$$(G^T G + \alpha^2 I)s_\alpha = G^T \bar{D}, \tag{4}$$

where α is the regularization parameter and s_α is the regularized solution. The success of the Tikhonov regularization technique depends on making a good choice of the regularization parameter α, which is not easy to find. The reason is that the solution s_α is too sensitive to perturbations in D, i.e., a small change in D may produce a large change in s_α.

On the other hand, it is well known that a trust-region sub-problem (TRS) method is quite attractive optimization technique, which finds a direction and a step size in an efficient and reliable manner with the help of a quadratic model of the objective function (*Gander, 1978*). In general, the trust-region methods define a region around the current iteration within which they trust the model to be an adequate representation of the objective function, and then choose the step to be the approximate minimizer of the model in this trust-region. In effect, they choose the direction and length of the step simultaneously. If a step is not acceptable, they reduce the size of the region and find a new minimizer. The step direction changes whenever the size of the trust-region is altered. To approach the TRS form, we should begin with the constrained least-squares problem, which takes the form

$$\min_s \| Gs - \bar{D} \|_2, \text{ subject to } \| s \|_2 \leq \varepsilon. \tag{5}$$

Regularization depends here on choosing the parameter ε. The problem can be re-formulated as $\mu(A, a, \varepsilon)$ the so called trust-region sub-problem TRS (*Fortin and Wolkowics, 2004*) as:

$$\mu(A, a, \varepsilon) \quad \min\ q(s) := s^T A s - 2a^T s, \text{ subject to} \| s \|_2^2 \leq \varepsilon^2, \tag{6}$$

where $A := G^T G$ is a $M \times M$ symmetric ($m > 2$), $a := G^T \bar{D}$ is an m-vector. ε is the trust-region's fixed radius (positive scalar), and s is the m-vector of unknowns. All matrix and vector entries are real.

3.2. L-curve criterion and Picard condition

The L-curve criterion is based on a log-log plot of the corresponding values of the residual and solution norms $(\log \|Gs_k - \bar{D}\|_2,\ \log \|s_k\|_2),\ k = 1, \ldots, p.$

The optimal regularization parameter corresponds to a point near the corner. Singular Value Decomposition (SVD) of the matrix G is a tool that helps in understanding the L-curve analysis. It can be written as:

$$\mathrm{G{=}USV^T}, \tag{7}$$

where matrix S is a diagonal $n \times n$ matrix consisting of singular values σ_i of G, $\sigma_1 \geq ... \geq \sigma_\mathrm{n}$ and U, V are orthogonal matrices, i.e:

$$U^T U = I, \;\; V^T V = I. \tag{8}$$

So, the Tikhonov regularized solution s_α can be written by substituting the SVD of matrix G into Eq. 4 as:

$$\|s_\alpha\|_2^2 = \bar{D}^T U (S(S^2 + \alpha^2 I))^2 U^T \bar{D} \;=\; \sum_{i=1}^{n} (f_i \frac{U_i^T \bar{D}}{\sigma_i})^2. \tag{9}$$

So,

$$\|Gs_\alpha - \bar{D}\|_2^2 = \sum_{i=1}^{n} ((1 - f_i)\; U_i^T \bar{D})^2, \tag{10}$$

where f_i is the so called Tikhonov filter factors, defined as:

$$f_i = \frac{\sigma_i^2}{\sigma_i^2 + \alpha^2} \quad . \tag{11}$$

Such expressions (Eq. 9 and 10) can be used to illustrate what happens to the solution in the presence of noise. So, when adding uncorrelated noise η, this would result in extra contribution to the solution caused by noise components. Then, the true solutions s_o can be expressed as (*Fortin and Wolkowics, 2004*):

$$\|s_o\|_2^2 = \sum_{i=1}^{n} \left(\frac{U_i^T D}{\sigma_i} + \frac{U_i^T \eta}{\sigma_i}\right)^2, \tag{12}$$

assuming that both G and s are invertible.

So, for small singular values these contributions will be very large, whenever the noise vector is not orthogonal to the corresponding singular vectors, U_i. This simply clarifies why the naive least squares solution is not meaningful and a regularized solution should be sought instead. Even if there

is no noise, the problem is still there if the matrix has very small singular values (close to zero). It is required that $\left|U_i^T D\right|$ should decay faster than σ_i. This is known as a Picard condition. It is guaranteed that if such condition is satisfied, the least squares solution has a reasonable norm and is thus physically meaningful (*Hansen, 1999)*. Then, TRS can be used to form the L-curve (*Fortin and Wolkowics, 2004*) as:

$$L(G,\bar{D}) := \left\{ \left(\log(\varepsilon), \log \| Gs_\varepsilon - \bar{D} \| \right) : \varepsilon > 0, \quad s_\varepsilon \text{ is optimal for TRS} \right\}. \quad (13)$$

As we are now familiar with the TRS and L-curve concepts, it is time to demonstrate in details the proposed PTRS method and briefly the well known TSVD with L-curve pruning.

3.3. PTRS and TSVD regularization techniques

PTRS method is an extension of the traditional TRS approach. *Grodzevich (2004)* has explained the PTRS method as an effective tool that can be used in conjunction with the L-curve maximum curvature criterion. The classical algorithm for solving TRS, with a given trust-region radius ε, is based on solving Eq. 4 for various choices of α, and using a Cholesky factorization of $G^T G + \alpha^2 I$ (*Moré and Sorensen, 1983*). More recently, a parameterized trust-region approach to find the regularized solution x_ε, has been used by *Rojas and Sorensen (2002)*. Then, *Grodzevich and Wolkowics (2009)* have extended the traditional TRS approach that makes use of L-curve maximum curvature criterion, which is applied here to solve our problem. It is assumed that the easy case holds, and that the optimum point lies on the boundary of the feasible region, i.e. $\| s^* \| = \varepsilon$. *Grodzevich and Wolkowics (2009)* also showed that the TRS algorithm visits, each iteration, a point on the L-curve. Therefore, the trust-region radius ε can be dynamically changed to steer the algorithm to the elbow of the L-curve. For further details on the method, the reader can refer to *Grodzevich and Wolkowics (2009)*.

As the kernel function decays with the inverse squared depth, the inverted model will mostly be concentrated near the surface. This tendency can be overcome by introducing a depth weighting to counteract the natural geometric decay. *Li and Oldenberg (1998)* have shown that it was reasonable to approximate the decay with depth by a function of the form $w(z) =$

$1/(z+z_0)^{\beta/2}$, where β is usually equal to 2 and z_0 depends upon a reference level. We used the diagonal matrix:

$$W_{m_i} = 1/(z_{m_i} + \varepsilon)^{\beta}, \tag{14}$$

where $\beta = 0.9$ (*Boulanger and Chouteau, 2001*) and a small ε to prevent singularity when z is close to 0.

To compare the inverted solutions (magnetic susceptibilities) to the true ones in synthetic examples; the Pearson correlation coefficient (r) of two set of observations $\{(x_i,y_i)$: i=1,..,n$\}$ is used where

$$r_{corr} = \frac{\sum_{i=1}^{n} (x_i - \overline{x}) \ (y_i - \overline{y})}{\sqrt{\sum_{i=1}^{n} (x_i - \overline{x})^2 \sum_{i=1}^{n} (y_i - \overline{y})^2}}, \tag{15}$$

$\overline{x}$ and $\overline{y}$ are the mean values of x and y, which represent synthetic and inverted susceptibilities in our case. When the two sets of data are identical, r is unity, while they differ when $r << 1$.

The above method is used to invert the Earth's magnetic field. The inverted profile is assumed to be taken over an array of prismatic cells with different unknown magnetic susceptibilities. The complete code is written in Matlab 2009a and the function of the PTRS regularization tool, *Grodzevich (2004)*, is implemented. The inputs are the number of rows and columns of the subsurface model, the width of each cell, vector of true susceptibilities for synthetic example, noise ratio is introduced to synthetic data as well as the magnetic parameters like the inclination, declination, total field etc. The code calculates the magnetic field of the synthetic model and adds also the required noise. The output is the inverted susceptibilities of the subsurface cells. The number of data points in real examples is usually less than the number of unknowns. Therefore, an interpolation function is used to increase the data in order to get an even or over-determined problem. Finally, the inverted model is drawn using a color scale to present the distribution of subsurface susceptibilities.

For the sake of comparison, the L-curve pruning with adaptive L-curve method is chosen to invert the same earth models as a robust tool described by *Hansen et al. (2007)*. It has been applied successfully on gravity ill-posed inverse problem (*Abdelazeem et al., 2007*). Its idea simply is to locate

the corner of a discrete L-curve using truncated singular value decomposition (TSVD). A sequence of pruned L-curves is used to capture the global features of the curve. The main idea was to remove the right amount of points from the discrete L-curve, so the corner can easily be found using the remaining set of points. For more details refer to the above two papers.

4. Synthetic examples

The new PTRS method (*Grodzevich and Wolkowics, 2009*) is tested using two synthetic examples contaminated with different noise levels. The TSVD method with L-curve pruning (*Hansen et al., 2007*) is also applied to the same examples for comparison.

4.1. Example 1

The first synthetic example (Model 1) consists of 160 square cells arranged in 8 rows and 20 columns. The ambient field is assumed to be 40 000 nT with a direction of inclination 60° (same as inclination of cell magnetization) and declination 3°. The Azimuth of the measured data is taken as zero. The data points are 160, i.e. our problem is an even-determined one. The condition number of matrix G is found to be $1.6932 \cdot 10^{12}$. As the noise free data is not an actual case, we start with low perturbed data (Signal to Noise Ratio, SNR = 90 dB). The Picard condition is tested for noise free data (Fig. 1a) and also for highly perturbed one (Fig. 1b), 15 dB, to illustrate the effect of noise on Picard plot. The Picard condition is satisfied till the first 80 prisms (in noise free case) and till the first 60 prisms (when 15 dB noise is added), where the singular values σ decay faster than the Fourier coefficients. The singular values decay from the order of 10^5 to the order of 10^{-7} causing the condition number to be of the order of 10^{12}.

Different noise levels have been added to the data and the problem is solved using both the proposed PTRS method and TSVD with pruning L-curve for comparison. The inverted earth models together with the observed and inverted magnetic fields are shown in Figs. 2 and 3. The Earth's model is dramatically distorted using TSVD with pruning L-curve, when SNR = 60 dB, is added to data. On the other hand, the PTRS method has

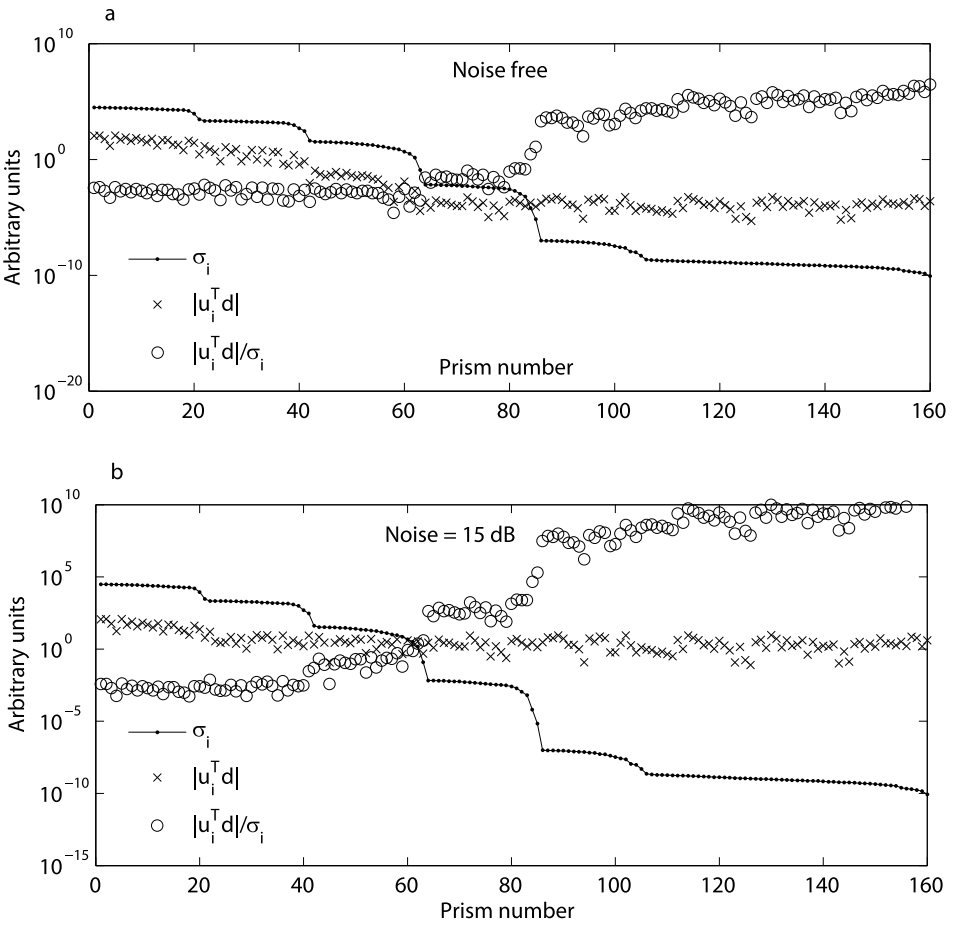

Fig. 1. The Picard plot for synthetic example 1, a) for noise free and b) for 15 dB noise level implemented.

been applied successfully to the same model with noise ratio varying from 80 dB to 15 dB, i.e. higher noise has been added. Subsequently, the Pearson correlation coefficient r_{corr} calculated between the inverted and actual data are nearly complete coincidence (0.99 to 0.98) for both methods. Also, the correlation coefficient is calculated between the inverted susceptibilities (solutions) and the actual values, which is presented in Table 1 for different noise ratios. It slightly decreases with increasing noise using the PTRS

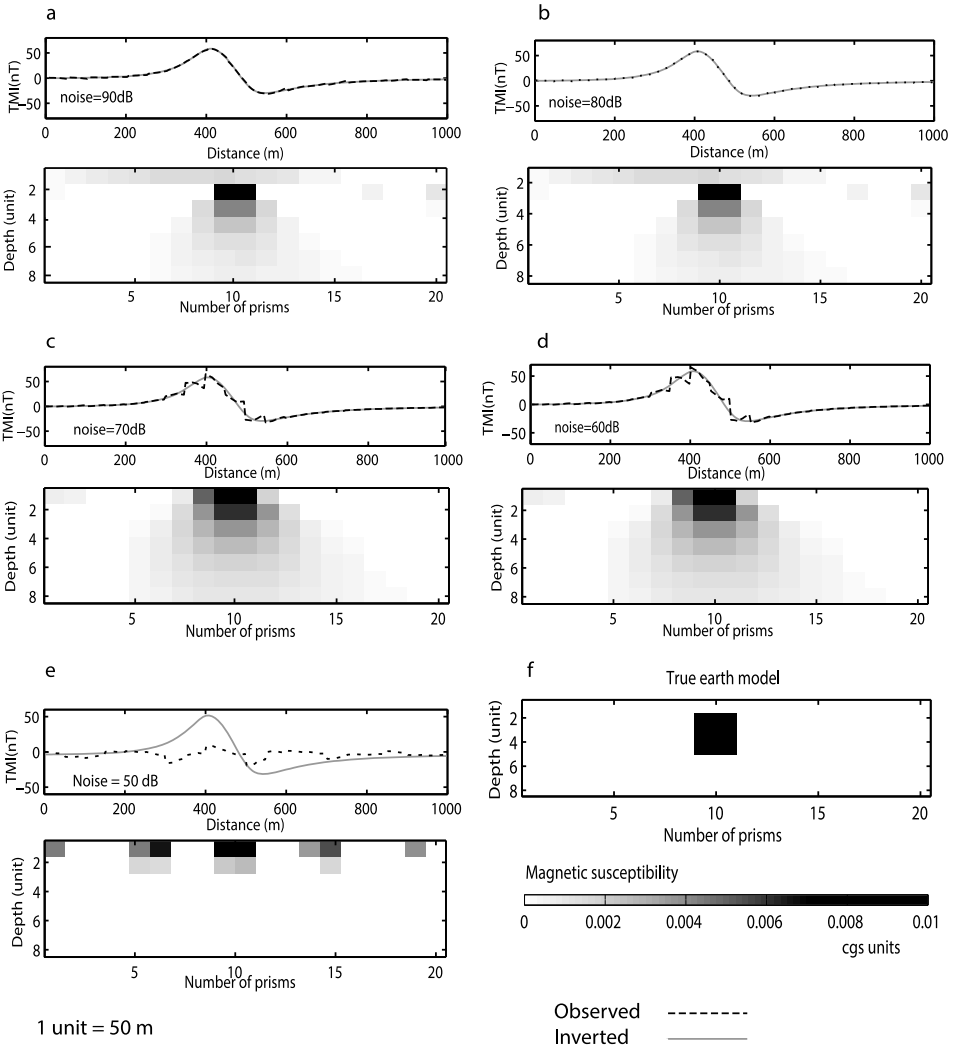

Fig. 2. Inverted earth models, using TSVD with L-curve pruning, together with true and inverted magnetic fields when adding different noise levels to data, a) 90 dB, b) 80 dB, c) 70 dB, d) 60 dB to data, e) 50 dB and f) True model.

method. When the same model was inverted using TSVD with adaptive pruning L-curve (*Hansen et al., 2007* and *Abdelazeem et al., 2007*), the inverted model was acceptable, nevertheless the two bottom rows of prisms

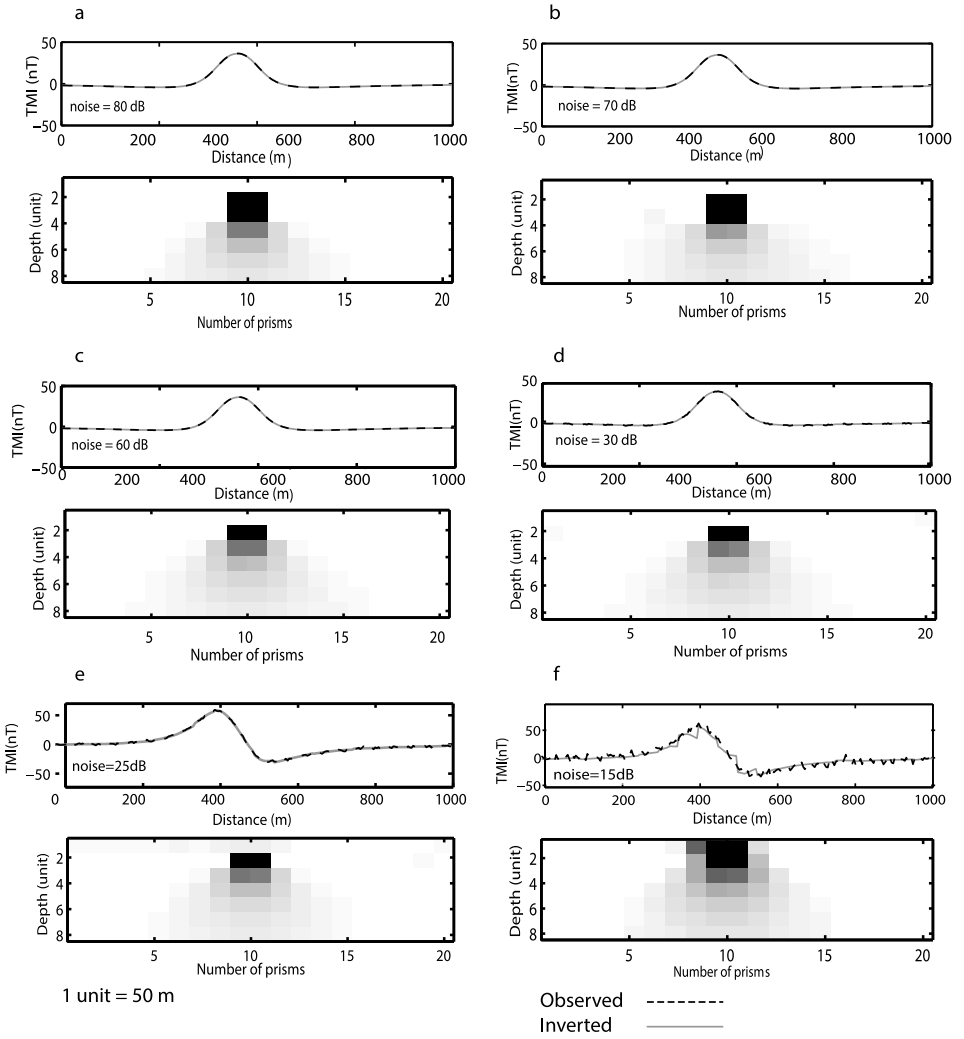

Fig. 3. Inverted earth models, using PTRS, together with true and inverted magnetic fields when adding different noise levels to data, a) 80 dB, b) 70 dB, c) 60 dB and d) 30 dB e) 25 dB, f) 15 dB to data and g) the true earth model.

attain very high susceptibilities, which dominated the rest of the plausible model. The correlation factors between inverted susceptibilities using PTRS and TSVD with pruning L-curve and true ones are presented also in Table 1.

Table 1. The Pearson correlation coefficient between true and inverted vectors of magnetic susceptibilities resulted from PTRS and TSVD with pruning L-curve for model 1, using different SNR

SNR (dB)	r_{corr} **between inverted and true susceptibilities**	
	PTRS	**TSVD**
90	0.90	0.75
80	0.90	0.75
70	0.89	0.45
60	0.80	0.09
50	0.80	0.09
30	0.79	–
25	0.78	–
15	0.58	–

Notice the dramatic decrease in the correlation factor with increasing noise, i.e. when decreasing SNR.

4.2. Example 2

The second synthetic example (Model 2) represents two bodies, an outcropping inclined dike and a buried massive body. The number of square cells (M) is 160 and the data points (N) are 200. The ambient field F is assumed to be 40 000 nT, the inclination of the field is 60°, and the declination is 2°. The inclination of all prisms is assumed to be identical and equal to the field inclination. Magnetization is assumed to be induced, but the program is designed to hold the remnant magnetization if it exists. The condition number of the kernel matrix is found to be $5.4879\,10^{14}$. The Picard plot is shown in Fig. 4 for both noise free and contaminated data, 15 dB. Figs. 5a, b, c and d show the TSVD solutions for data contaminated with SNR of 90 dB to 60 dB. True model is shown in Fig. 5e. On the other hand, the PTRS method is applied using SNR from 80 dB to 15 dB on the same data. The results (Fig. 6) are accepted till 20 dB noise level, as the depth to top is accepted. When 15 dB has been added to the data, the depth to top becomes nearer to surface. Table 2 shows that the correlation coefficient

between true and inverted models by PTRS are closer to unity, while those inverted by TSVD with pruning L-curve ranges from 0.75 for 90 dB SNR to 0.09 for 60 dB SNR. These results prove the stability of PTRS with higher levels of noise.

Table 2. Summarizes the results of model 2 through different noise levels and the corresponding change in Pearson correlation factor between true and inverted vectors (magnetic susceptibilities) using PTRS and TSVD with L-curve pruning

SNR (dB)	**Correlation between inverted and true magnetic susceptibility vectors**	
	PTRS	**TSVD (pruning)**
90	0.91	0.75
80	0.91	0.75
70	0.90	0.45
60	0.88	0.09
50	0.81	0.09
40	0.81	–
25	0.80	–
20	0.79	–
15	0.63	–

5. Field examples

PTRS method has been further applied to a real total magnetic field data from Saudi Arabia over Al Ji'lani basic intrusion (example 1), and a vertical gradient magnetic field of an archeological site in Italy (example 2).

5.1. Field example 1

The Precambrian Al Ji'lani basic intrusion forms an oval outcrop (9×6 km) over 50 km^2 of relatively flat well-exposed country, 10 km southwest of Ad Dawadimi district, Kingdom of Saudi Arabia. Within the oval-shaped outcrop area of the intrusion, there is a total exposed thickness of 2,600 m of rock which dips inward, and consists of amphibolitized and fresh gabbros,

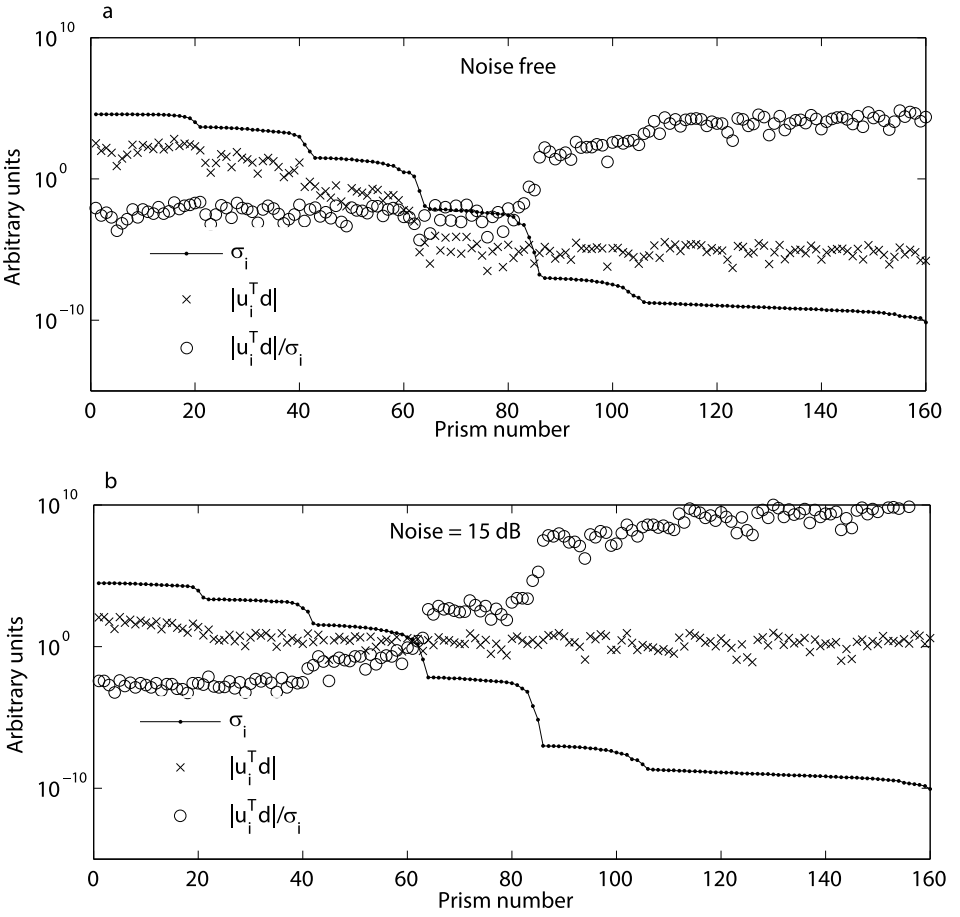

Fig. 4. Picard plot for example 2, (a) for noise free data, and b) for 15 dB noise level implemented.

troctolites, norites, and anorthosites (*Al Shanti, 1974*). The Al Ji'lani layered intrusion has its major axis trends N 42° W. The intrusion is made up of rather uniform concentric layers dipping radially inward. Dips are generally steep, the marginal layers dipping 50–70° and the central layers dipping about 20°. Local distortions in dips and layering are due to later dike and granitic intrusions as displayed in the central area.

The layered intrusion has a marked, well defined, aeromagnetic signa-

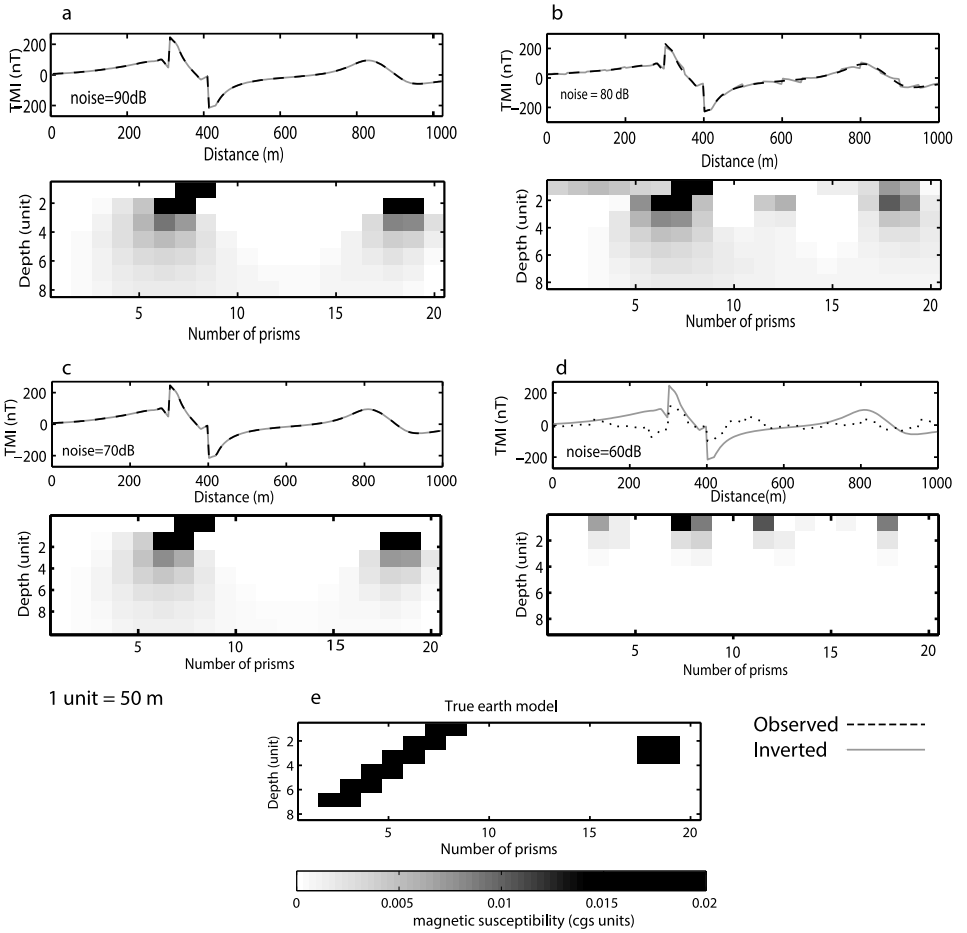

Fig. 5. Inverted earth models, using TSVD with adaptive pruning L-curve, together with true and inverted magnetic fields when adding different noise levels to data, a) 90 dB, b) 80 dB, c) 70 dB, d) 60 dB to data and e) the true earth model.

ture within the surrounding area of low magnetic relief, as shown in Fig. 7. *Lambolez (1968)* qualitatively interpreted the magnetic pattern to indicate a deep-rooted basic mass with a rather sharp and steeply dipping contact and noted the presence of marked subsidiary anomalies within the structure. The suggested structure of a steep-sided mass is important relative to the alternative possibility that the intrusion has a shallow lopolithic floor ad-

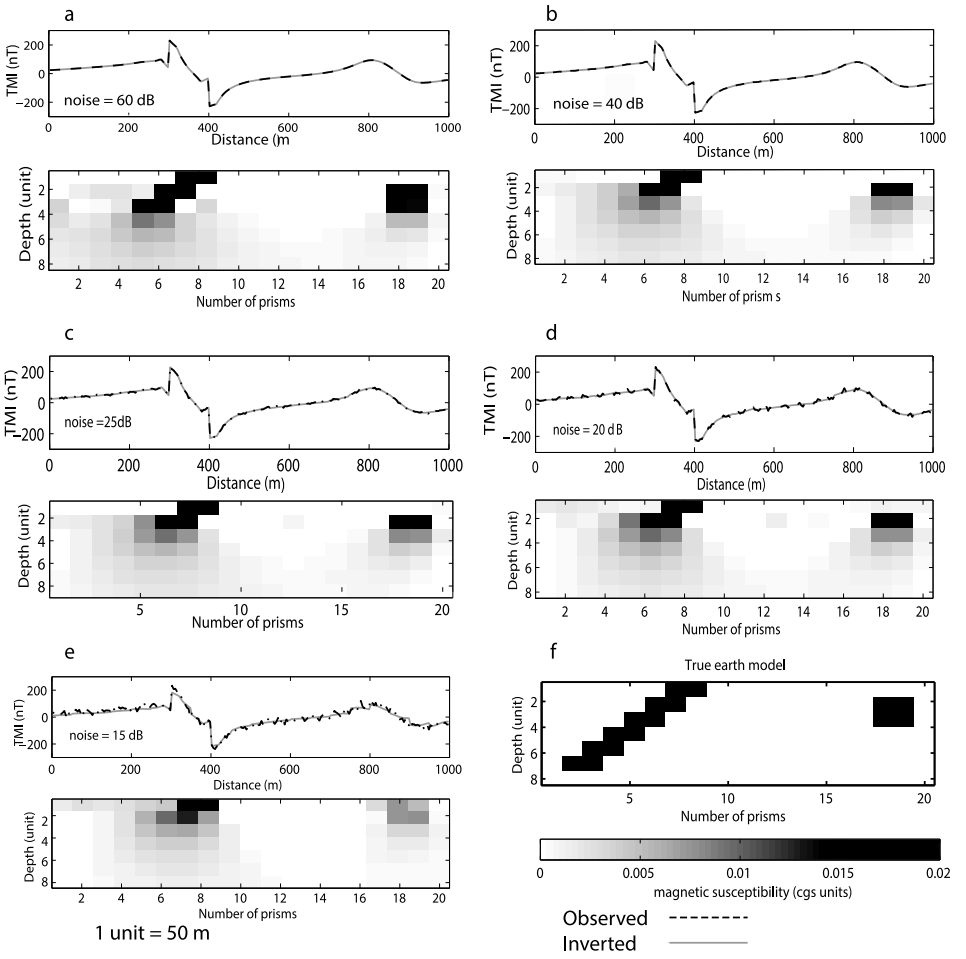

Fig. 6. Inverted earth models, using PTRS method, together with true and inverted magnetic fields when adding different noise levels, a) 60 dB, b) 40 dB, c) 25 dB and d) 20 dB e) 15 dB to data and f) The true model with color scale used for susceptibility.

jacent to the outermost ring of basic rock. Present geologic investigations suggest roof pendent intrusion instead of deep rooted mass. The PTRS technique has been applied to reveal the present doubt.

The area of study and the studied profiles A-A' and B-B' are shown in Fig. 7. Declination of the area is 2°35′ and the total field is 40 000 nT.

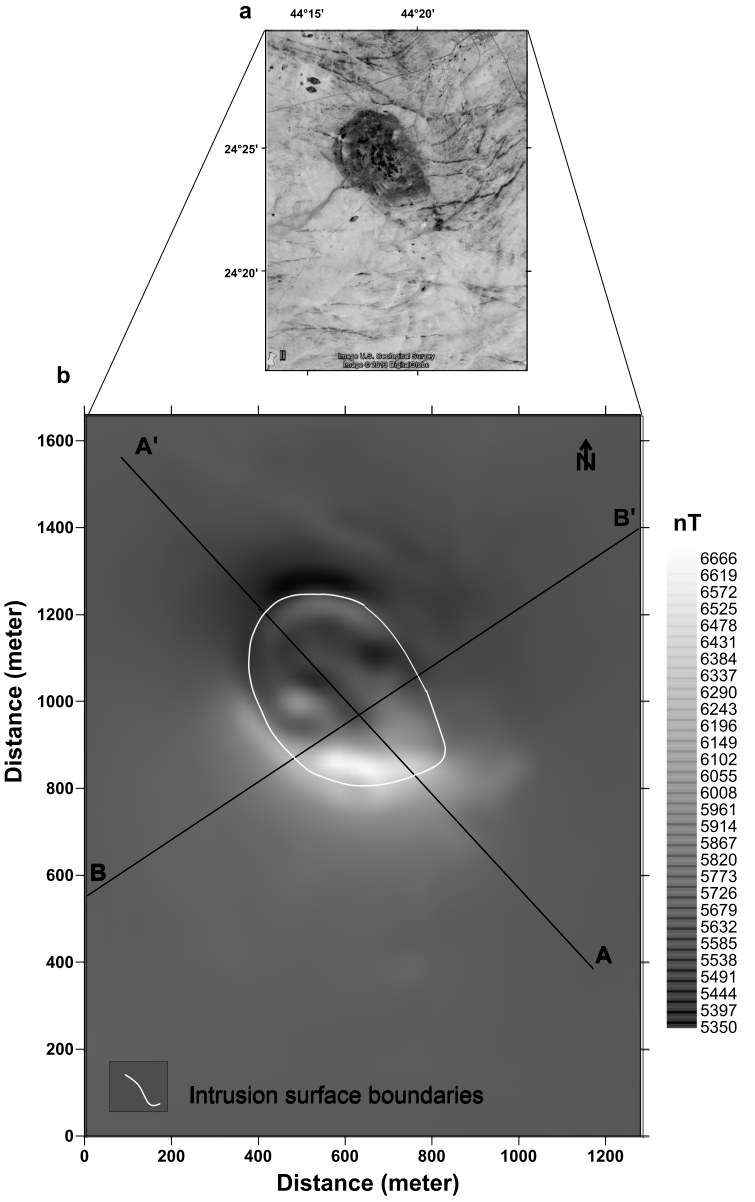

Fig. 7. Al Ji'lani intrusion, Saudi Arabia. a) Location map with a satellite image retrieved from Google Earth. b) The RTP magnetic over the area under study with the two profiles subjected to inversion.

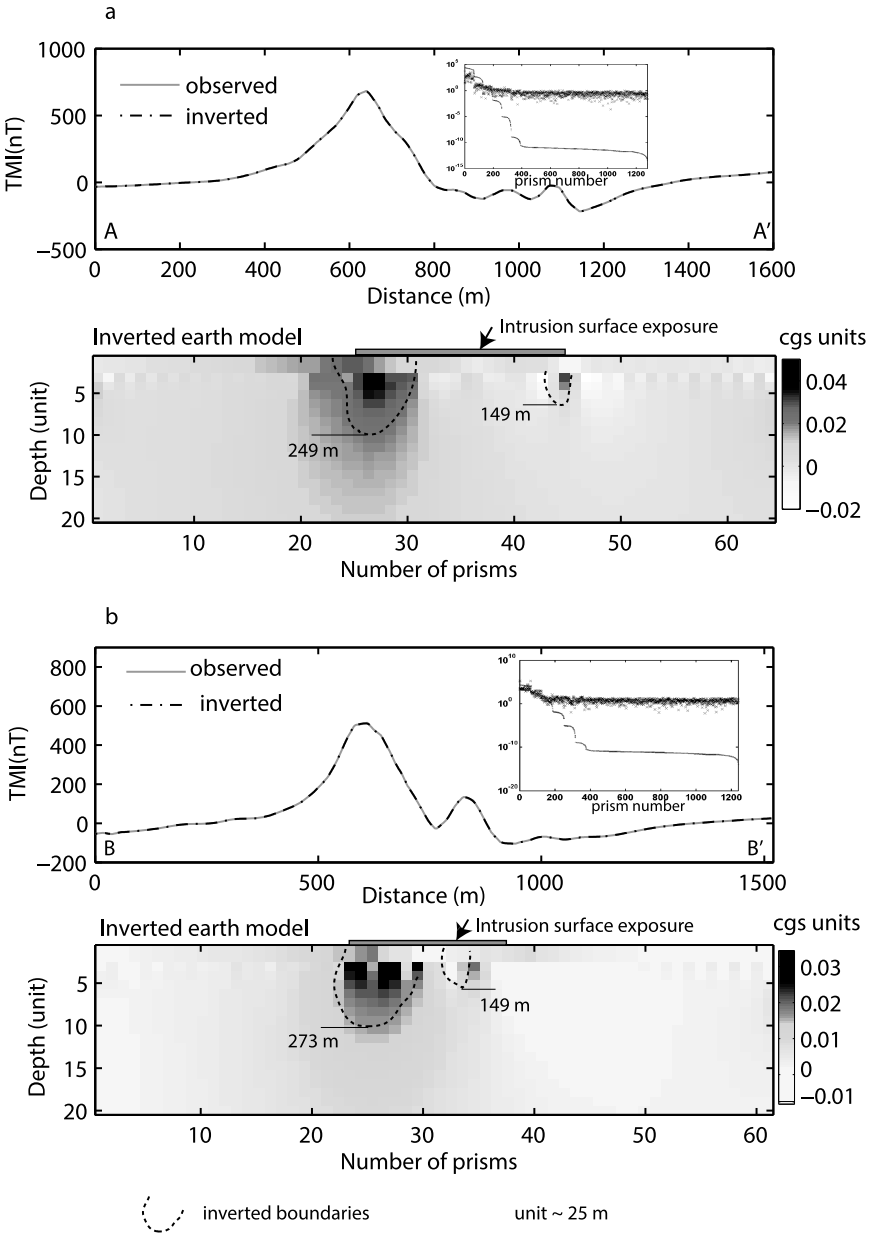

Fig. 8. Inversion results for field example 1 over a) profile A-A' and b) profile B-B'. Picard plots are shown as sub-plots.

The regional trend is subtracted from profiles A-A' and B-B' before inversion tool is used. Fig. 8a shows the profile A-A' and the inverted model together with the Picard plot as a sub-plot. The profile A-A' is of total length 1598 m. The model Earth is subdivided into 1280 square cells (M), arranged in 20 rows and 64 columns. The data points (N) are interpolated to 1280 data points. The Picard plot proves the ill-posedness of the problem represented by the fast decaying of the σ_i (condition number $\sim 10^{20}$) with respect to slower decay of $\left|U_i^T d\right|$. The Picard condition is only satisfied in the first 200 cells. Consequently, PTRS method is applied to solve this highly ill-posed problem. The inverted earth model suggests two bodies. One is to the left with maximum depth of 249 m and the other to the right with maximum depth of 149 m. The profile B-B' is of total length 1515 m. The earth model is subdivided into 1220 square cells arrange as 20 rows and 61 columns. So, the unit is nearly the same as that in first model (~ 25 m). Inverted model over profile B-B' is shown in Fig. 8b with its Picard plot also showing severe ill-posedness. The condition number $\sim 10^{20}$, which is more than that appeared in the synthetic examples. The inverted model, using PTRS method, suggests also two near bodies, the one to the left one extends to 273 m and the right one has a maximum depth of 149 m. This result confirms the roof bendent intrusion hypothesis over the deep rooted base mass.

5.2. Field example 2

The PTRS has also been applied to magnetic data in a well-studied area of the Sabine Necropolis at Motelibretti, Rome, Italy (*Stocco et al., 2009*). This archeological site is characterized by chamber tombs, and we have to find its position and size. A N–S profile is extracted from the vertical gradient field of the vertical component map of the area and subjected to inversion using PTRS technique. Although no constraints are added except the method's powerful dynamic trust region estimation, the results show a remarkable compatibility to previous results (*Stocco et al., 2009*). Fig. 9a demonstrates Stocco's inversion results, whereas the inverted earth model using PTRS is shown in Fig. 9b. The ill-posedness of the problem is obvious from the Picard plot. The inversion results show a depth and shape of the two buried rooms very close to Stocco's model.

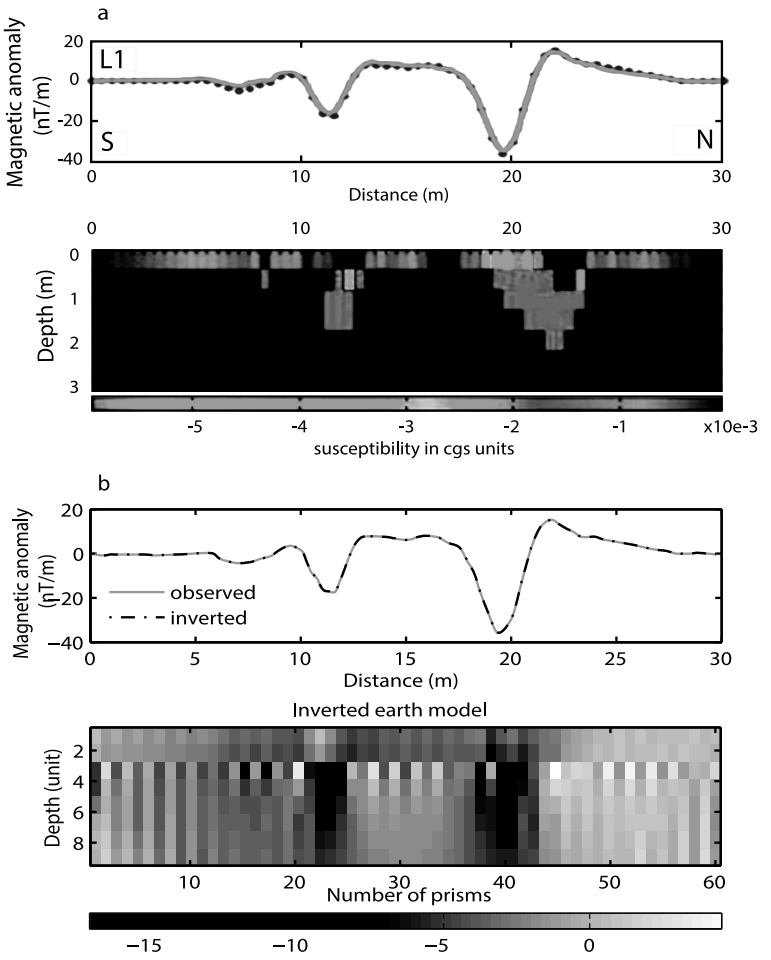

Fig. 9. Inversion results for field example 2 (Sabine Necropolis at Motelibretti, Rome, Italy). a) Inverted model of magnetic field profile over the Sabine Necropolis, at Montelibretti, Rome, Italy (*Stocco, 2009*). b) Inverted earth model using PTRS for the same profile.

6. Conclusion

Some magnetic inverse problems cannot be solved with standard inversion tools. This is due to instability, sensitivity to noise content in data or ill-

conditioned kernel matrix. The ill-posedness of the problem appears when the condition number is in the order of $\sim 10^5$ or higher. The higher the condition number, the stronger the ill-posedness of the problem. This ill-posedness will appear clearly in the Picard plot represented by the fast decay of the σ_i with respect to slower decay of $\left|U_i^T d\right|$. In such cases we should use regularizing techniques. In this paper a computationally efficient Parameterized Trust Region Sub-problem technique (PTRS) has been applied to the magnetic inverse problem. A comparison between TSVD with adaptive pruning L-curve technique and the newly proposed PTRS approach, using two synthetic examples with different noise levels, suggests higher stability of the PTRS against higher noise levels. As shown in the examples, the dynamically changed trust-region radius ε is a key element to find the satisfying minimum to the objective function by steering the algorithm to the elbow of the L-curve.

Successful use of the proper weighting to the kernel function minimizes the tendency of the calculated model to cluster near the surface. PTRS approach appears to work well in practice as illustrated by application to different field examples of various degrees of ill-posedness.

In summary this inversion approach seems promising for real magnetic inverse problem solution where much noise content in the data is expected. The potential of this approach across a range of applications merits further testing on more complicated geologic problems.

Acknowledgments. I am grateful for Prof. Dr. Hanfy Debees from National Research Institute of Astronomy and Geophysics (NRIAG) for reviewing the manuscript. My great appreciation to Prof. Nasser Sweilam (Department of Mathematics) and Prof. Mohamed Gobashy (Department of Geophysics) from Cairo University for their constructive and helpful suggestions. Thanks also to Prof. El-Dogdog (King Abdulaziz University, Faculty of Earth Sciences) for the valuable geological discussion of the first field example. Sincere thanks go also to the reviewers and Editor, who helped me to improve the manuscript.

References

Abdelazeem M., Sweilam N., Bayoumi A. I., Refai E. M., 1998: Application of Linear Quadratic Programming to the Inverse Gravity Problem, Africa/Middle East. Second International Geophysical Conference & Exposition, Cairo, Egypt, Feb. 17-19.

Abdelazeem M., Sweilam N. H., Gobashy M., Nagy A. M. A., 2007: Two dimensional gravity inverse problem using adaptive pruning L-curve technique. Bull. Fac. Sci., Cairo Univ., **75**, (A), 93–115.

Al Shanti A. M., 1974: Al Ji'lani layered basic intrusion, Ad Dawadmi District, Kingdom of Saudi Arabia. Mineral resources Bulletin, **12**, Directorate General of Mineral Resources, Kingdom of Saudi Arabia.

Ardalan A. A., Zamzam D., Karimi R., 2011: An alternative method for density variation modeling of the crust based on 3-D inversion. Journal of Applied Geophysics, **75**, 355–362.

Baker C. T. H., 1977: The numerical treatment of integral equations. Clarendon Press, Oxford.

Blakley R. J., 1996: Potential theory in gravity and magnetic applications. Cambridge University press.

Blaschek R., Hördt A., Kemna A., 2008: A new sensitivity-controlled focusing regularization scheme for the inversion of induced polarization data based on the minimum gradient support. Geophysics, **73**, F45–F54.

Boulanger O., Chouteau M., 2001: Constraints in 3D gravity inversion. Geophys. Prospect., **49**, 265–280.

Dennis J. E. Jr., Schnabel B. R., 1983: Numerical methods for unconstrained optimization and nonlinear equations. Prentice-Hall, Englewood Cliffs, New Jersey.

Fedi M., Hansen P. C., Paoletti V., 2005: Analysis of depth resolution in potential-field inversion. Geophysics, **70**, A1–A11.

Fortin C., Wolkowics H., 2004: The trust region sub-problem and semidefinite programming. Optimization methods and software, **19**, 41–67. (Special issue dedicated to Jochem Zowes 60^{th} birthday, Guest editors: Florian Jarre and Michal Kocvara).

Gander W., 1978: On the linear least squares problem with a quadratic constraints. Technical report STAN-CS-78-697, Department of Computer Sciences, Stanford University, Stanford, CA.

Grodzevich O., 2004: Regularization using Parameterized Trust Region Sub-problem. Master Thesis in mathematics, University of Waterloo, Ontario, Canada.

Grodzevich O., Wolkowicz, H., 2009: Regularization using parameterized trust region sub-problem. Math. Program., Ser. B, **116**, 193–220.

Guillen A., Menichetti V., 1984: Gravity and magnetic inversion with minimization of a specific functional. Geophysics, **49**, 1354–1360.

Hansen P. C., 1990: The Discrete Picard Condition for discrete ill-posed problems. BIT, **30**, 658–672.

Hansen P. C., 1998: Rank-deficient and discrete ill-posed problems, numerical aspects of linear inversion. Technical university of Denmark, Lyngby, SIAM, Philadelphia.

Hansen P. C., 1999: The L-curve and its use in the numerical treatment of inverse problems. Technical report, Technical University of Denmark.

Hansen P. C., Jensen T. K., Rodrigues G., 2007: An adaptive pruning algorithm for the discrete L-curve criterion. Journal of computational and applied mathematics, **198**, 483–492.

Lambolez B., 1968: Aeromagnetic and scintillometric survey 1966-67; Report on starting operations. Saudi Arabian Gen. Mineral Resources open-file rept.

Last B. J., Kubik K., 1983: Compact gravity inversion. Geophysics, **48**, 713–721.

Li Y., Oldenburg D. W., 1998: 3-D inversion of gravity data. Geophysics, **63**, 109–119.

Moré J. J., Sorensen D. C., 1983: Computing a trust region step. SIAM J. Sci. Stat. Comput., **4**, 3, 553–572.

Morse P. M., Fashbach H., 1953: Methods of theoretical physics. McGraw-Hill, New York.

Pašteka R., Karcol R., Kušnirák D., Mojzeš A., 2012: REGCONT, A Matlab based program for stable downward continuation of geophysical potential fields using Tikhonov regularization. Computer and Geosciences, **49**, 278–289.

Portniaguine O., Zhdanov M. S., 2002: 3-D magnetic inversion with data compression and image focusing. Geophysics, **67**, 1532–1541.

Rojas M., Sorensen D., 2002: A trust region approach to the regularization of large-scale trust region sub-problem. M. SIAM J. Sci. Comput., **23**, 6, 1842–1860 (electronic).

Silva J. B. C., Oliveira F. S., Barbosa V. C. F., Velho H. F. C., 2007: Apparent density mapping using entropic regularization. Geophysics, **72**, 4, 151–160.

Stocco S., Godio A., Sambuelli L., 2009: Modelling and compact inversion of magnetic data: A Matlab code. Computers and Geosciences, **35**, 2111–2118.

Tezkan B., Hoerdt A., Gobashy M., 2000: Two dimensional radiomagnetotelluric investigation of industrial and domestic waste sites in Germany. Journal of Applied Geophysics, **44**, 2–3.

Tikhonov A. N., Arsenin V. Y., 1977: Solutions of ill-posed problems. V. H. Winston & Sons.

Zhdanov M. S., 1993: Regularization in inversion theory: Tutorial, Colorado School of mines.

Contributions to Geophysics and Geodesy Vol. 43/2, 2013 (125–140)

Substitution for lost one-hour means of the geomagnetic elements for the first half of the 20-th century at the Hurbanovo Geomagnetic Observatory by means of neural networks

Fridrich VALACH[1], Magdaléna VÁCZYOVÁ[1], Peter DOLINSKÝ[1], Melinda VAJKAI[1]

[1]Geomagnetic Observatory, Geophysical Institute of the Slovak Academy of Sciences Komárňanská 108, 941 07 Hurbanovo, Slovak Republic; e-mail: fridrich@geomag.sk

Abstract: The existence of long-acting observatories by itself does not guarantee that their historical magnetograms are available or complete. In the archive of the Hurbanovo Geomagnetic Observatory (acronym HRB; geographical coordinates 47.86°N, 18.19°E), records of the geomagnetic field made on photo paper covering the period between the two World Wars were found for which the values of the baselines are unknown. We studied if a feed-forward neural network with one hidden layer can be used to supplement one-hour means of the geomagnetic elements D, H and Z of observatory HRB, using for this purpose the geomagnetic data of observatories Potsdam, Seddin and Niemegk (all of them being referenced to Niemegk). We focused our interest on the first half of the 20-th century. The neural-network model for element D proved to be applicable to substitute for the lost data of the magnetic declination at observatory HRB; however, the usability of the model for both elements H and Z turned out to be limited to a few years close to beginning or end of data gaps. Further we supplemented the time series of annual means of geomagnetic elements D, H and Z at observatory HRB with the model data.

Key words: geomagnetic observatory, historical data, hourly means, annual means, neural networks

1. Introduction

Long-lasting series of correct and continuous time series of the geomagnetic field records are crucial for studying secular changes of the geomagnetic field. Likewise, the magnetograms covering many years of observations are a useful material for analyses of relations between the geomagnetic activity

and some other phenomena, such as the solar activity or changes of the planetary climate. Such series of the geomagnetic data are provided by old magnetic observatories. Unfortunately, the existence of a long-acting and unceasingly working observatory by itself does not guarantee that the historical magnetograms of it are available or complete. There were many reasons for the incompleteness; the most important of them sprang from history: warfare or other rude events. The circumstances sometimes interrupted geomagnetic observations; another time, a part of valuable observed information was completely lost.

The data which we dealt with in the paper were those of the Geomagnetic Observatory at Hurbanovo (until 1948 called Stará Ďala, Ógyalla or Ó Gyalla in Hungarian). The acronym of the observatory is HRB. It is a mid-latitude magnetic observatory with geographical latitude 47.86^oN and longitude 18.19°E.

The initial stages of the observatory are connected with Dr. Miklós Konkoly-Thege, the director of the state Institute for Meteorology and Earth's Magnetism in Budapest. As the expansion of Budapest disturbed the geomagnetic observations made at Buda, Dr. Konkoly-Thege moved the observatory instruments to his astronomical observatory at Ógyalla/Stará Ďala in 1890. The geomagnetic observatory was officially founded ten years later, on September 30, 1900. The history of the observatory had been narrated in detail by *Ochabová and Ochaba (1977)* as well as *Prigancová and Vörös (2001)*. From their papers we can learn about the periods which were covered with the registrations of the complete sets of the geomagnetic field; when, on the other hand, data gaps occurred; and which years had registered only one or two elements (Fig. 1).

Beginning in 1893, the results of the geomagnetic observations were published in monthly and annual reports. In 1894, the observatory obtained new magnetic variation instruments of the Mascart type, manufactured by Carpentier. In 1898 (*Prigancová and Vörös, 2001*) or 1899 (*Ochabová and Ochaba, 1977*), the new variation pavilion was built in which the Carpentier's magnetographs were installed. One of the instruments was made for photographic recording. In 1903 the equipment of the observatory was furnished with new absolute instruments – the Wild theodolite together with an earth inductor enabled determining three magnetic elements; D, H and I. Starting with this year, the photographic magnetograms are available

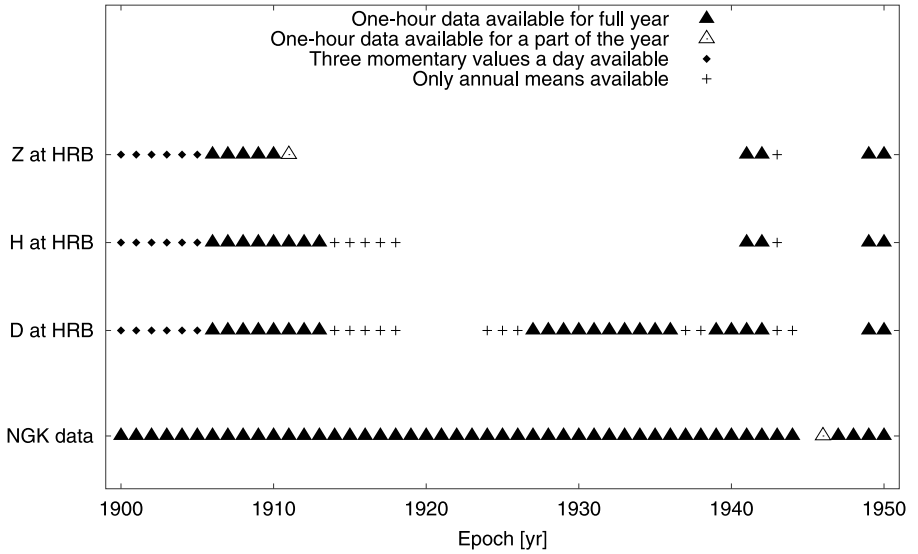

Fig. 1. Time periods when the values of geomagnetic elements D, H and Z are available for observatory HRB in the first half of the 20-th century. Intervals with one-hour means obtainable for observatory NGK (all geomagnetic elements) are also indicated. The years for which the annual means of the HRB geomagnetic elements are known, but at the same time the one-hour means have been lost, are shown as well. Momentary values of the geomagnetic elements D, H and Z observed three times in a day; at 7:00, 13:00 and 21:00; are available instead of one-hour means at observatory HRB prior to 1906.

in the archives of the Hurbanovo Geomagnetic Observatory. In 1911 the records of the vertical variometer became unreliable and observations of the inclination lost their significance, but the observations and recordings of the declination and horizontal intensity went on until the end of World War I in 1918.

Observations of the declination were renewed in 1924. Somewhere in 1938 registrations of the horizontal intensity restarted. Then stormy events leading up to World War II came. Despite the turbulent period, the observatory succeeded to develop and continue the observations. However, at the end of 1944 the absolute instruments were taken away from the observatory and a new gap in the observations commenced. In 1948 a set of instruments for recording the geomagnetic elements D, H and Z was reconstructed and absolute instruments were obtained. That year the name of

Stará Ďala changed to Hurbanovo. Since January 1, 1949, a complete series of the records of all geomagnetic elements are available for the Hurbanovo Geomagnetic Observatory (*Ochabová and Ochaba, 1977*).

In the archive of the Hurbanovo Geomagnetic Observatory magnetograms were found covering virtually the whole period between the two World Wars, including most of the wartime. They were the records of the geomagnetic field elements made on photo paper; however, a part of them was of poor quality. Some registered only incomplete set of geomagnetic elements, in certain cases only the magnetic declination. Moreover, the values of their baselines are unknown. So far we have not answered the question whether absolute measurements were not carried out that time, or their results were lost by misadventure. Probably the different answers are true for the different periods.

This paper studies if neural networks can be used to supplement the geomagnetic data for the data gaps of the Hurbanovo Observatory, using for this purpose the geomagnetic data of the observatories Potsdam, Seddin and Niemegk (all of them being referenced to Niemegk). These observatories belong to the oldest magnetic observatories in the world, and their one-hour means are available for the time period which we need for the supplement. Our interest was focused on the first half of the 20-th century, since the geomagnetic observatories were rare in Central Europe that time, and Stará Ďala Observatory was one of them. This uniqueness adds to the value of the geomagnetic data of the observatory.

Applicability of artificial neural networks, especially so-called recurrent networks, to similar tasks has been showed by *Barkhatov et al. (2002)*. He produced one-hour geomagnetic data for the Alma Ata Observatory, Kazakhstan, on the base of Japanese observatory Kakioka. Nevertheless, we could not use his method without adaptation – his recurrent network requires continuous time series of training patterns, which are not at our disposal.

Therefore, the purpose of this paper is to show that the supplementation of the HRB geomagnetic data based on data from the observatories Potsdam, Seddin and Niemegk can be achieved by means of simpler neural networks than those used by *Barkhatov et al. (2002)*. Then the supplemented one-hour data are produced to fill the gap in time series of the geomagnetic field observed at HRB.

2. Data used

We used the data collected by the Hurbanovo Geomagnetic Observatory, which belongs to the Geophysical Institute of the Slovak Academy of Sciences. In order to avoid confusion, we used the present-day name of the observatory, that means Hurbanovo (HRB), also for the older epochs of the observatory's history. The data which we used were one-hour means of the magnetic declination D, and the horizontal and vertical components H and Z, respectively.

Along with the the data of HRB, we used one-hour means of elements D, H and Z observed at observatories Potsdam, Sedding and Niemegk, all of them referenced to Niemegk. Again, in order to simplify the orientation within the text, we named all the data from these three observatories as the data of Niemegk (NGK). We obtained them from the web page of the World Data Center for Geomagnetism, Kyoto, Japan (`http://wdc.kugi.kyoto-u.ac.jp/hyplt/index.html`).

For assessment of the proposed neural-network model, we used also geomagnetic data observed at observatories Munich (MNH), Maisach (MAS) and Fuerstenfeldbruck (FUR). They were annual means which we took from the Version 1.3. of the CD-ROM distributed by Geophysical Observatory Fuerstenfeldbruck, University of Munich, Germany, in 2002. Other data used for the assessment were the annual means observed at observatory Wien Auhof (WIA), which are available through the World Data Center for Geomagnetism, Edinburgh, UK (`http://www.geomag.bgs.ac.uk/data_service/data/annual_means.shtml`).

Further data which were compared with the modeled ones were those of the 11th Generation International Geomagnetic Reference Field (IGRF11), which has been released by Working Group V-MOD of the International Association of Geomagnetism and Aeronomy, and is available at web page `http://www.ngdc.noaa.gov/IAGA/vmod/igrf.html`.

3. Method of neural networks

In this paper we used artificial neural networks to fill the data gaps which occurred in the time series of one-hour means of geomagnetic elements for

observatory HRB. A similar problem was considered by *Barkhatov et al. (2002)*, who employed a neural network in order to produce substitutes for missing data at observatory Alma Ata. They produced one-hour means of the horizontal component. As inputs to their model, they used the corresponding values of H observed at observatory Kakioka. The neural network used by them was the recurrent network, which is able to grasp temporal relations inherent in time series through a layer of hidden neurons called a context layer (*Gurney, 1997*). Concerning the long distance between Kakioka and Alma Ata, such an advanced type of neural network was necessary.

The recurrent networks, however, have a fundamental disadvantage: the training patterns need to be arranged without gaps in chronological sequence. Such a requirement stems from the training algorithm according to which, in addition to learning from new patterns applied in a new training step, these networks learn from the preceding steps as well.

In our study, however, we had training patters from different periods which were considerably distant from one another. The data gaps between them lasted years or even decades. Thus, we were compelled to employ another type of neural networks which does not require long unbroken series of training patters. A feed-forward network with one hidden layer (*Demuth et al., 2007; Gurney, 1997*) appeared to be a good alternative. A more technical introduction to the neural network is given in Appendix A.

Replacing the recurrent network by the network of a simpler architecture was permitted by reason of the distance between Niemegk (52.07°N, 12.67°E) and Hurbanovo (47.86°N, 18.19°E), which is substantially shorter comparing with that in *Barkhatov et al. (2002)*. The difference in geographical longitudes of NGK and HRB is 5.52°, which means that the phenomena due to the diurnal variation of the geomagnetic field occur at Hurbanovo 22 minute before they are recorded at Niemegk. We considered this time shift in the structure of patterns which the neural networks were fed with: When the value of a geomagnetic element at HRB for an one-hour interval t was produced, the values of the geomagnetic element at NGK for both intervals t and $t + 1$ hour entered the neural networks as input parameters.

In order to provide their neural network some time marker, *Barkhatov et al. (2002)* supplemented the input parameters with a sawtooth function, the period of which was set to 24 hours. We used their idea; however, we dealt with much longer time series as did *Barkhatov et al. (2002)* hence we

needed to consider the annual and the secular variations of the geomagnetic field in addition to its diurnal variation. Consequently, two sawtooth functions were included to our input parameters, with periods of 24 hours and 1 year, respectively, together with a strictly increasing function.

The structure of the patterns for our neural networks consisted of five input and one output parameters, which entered the networks through one of five input neurons, or emerged from a single output neuron. The input parameters were as follows:

1. one-hour mean of the geomagnetic element E at NGK for the t-th one-hour period;
2. one-hour mean of the geomagnetic element E at NGK for the $(t+1)$-th one-hour period;
3. consecutive number t of the one-hour period since the beginning of the time series;
4. consecutive number of the one-hour period within a day;
5. day of year.

There was only one output parameter:

– one-hour mean of the geomagnetic element E at HRB for the t-th one-hour period.

Geomagnetic element E means magnetic declination D, horizontal component H, or vertical component Z.

The work with the neural networks consisted of three standard steps described, for instance, in (e.g. *Demuth et al., 2007*):

1. The aim of the first step was to determine an optimal number of the neurons contained in the hidden layer. For this purpose 4000 patterns were assigned by random choice, which were used for training the neural networks holding various numbers of neurons in their hidden layers. Only the patterns based on data of years 1906–1953 could be used for which both NGK and HRB data were available – such a restriction was applied to all patterns used in steps 1 and 2. The performances of the networks were compared on the base of some other 800 randomly assigned patterns. We found that for all geomagnetic elements, D, H and Z, the best results were achieved if the hidden layers consisted of three neurons.

2. The following step was a training of neural networks. At this point, only the networks containing three hidden neurons were adapted to their task. The training was based on 4000 new randomly chosen training patterns while the proper number of training iterations were estimated by means of some other 800 patterns, called validation patterns, selected by random choice. The whole procedure of creating training and validation patterns as well as neural network training was repeated ten times for each of the geomagnetic elements D, H, and Z.
3. In the final step, one-hour means of geomagnetic elements D, H and Z for observatory HRB were produced. This time the patterns provided to neural networks were incomplete – they consisted of the input parts only. The patterns were created for those of the intervals within 1911–1948 for which only one-hour means of NGK were available, and gaps in HRB data occurred. For each geomagnetic element, the medians computed from the outputs of ten independently trained networks were considered as final model data.

In steps 1 and 2, we used the back propagation algorithm, which is based on the generalized delta rule, improved with a momentum term (*Gurney, 1997*). The results of step 3 are discussed in the following section.

4. Results and discussion

Feeding the trained neural networks with one-hour means of geomagnetic elements D, H and Z from observatory NGK, we obtained model values of the corresponding geomagnetic elements, one-hour means, for observatory HRB. We produced the model data for those periods of the first half of the 20-th century when some data gaps occurred in the time series of HRB. Listing the data in the paper would be highly unwieldy. Instead we stored the data on the web page of the Hurbanovo Geomagnetic Observatory (`http://www.geomag.sk/nn-model-old-data`).

In order to assess the performance of the neural network model, we carried out a test for 4000 randomly chosen complete test patterns selected in the periods for which both NGK and HRB data were available. According to the test, the model for the magnetic declination seems to be the best (Table 1). Nice agreement between the model data and the ones observed

Table 1. Statistics made for 4000 test patterns chosen within the periods when one-hour means of both HRB and NGK were available. Correlation coefficient (CC), root mean squared error (RMSE), and mean absolute error (MAE) are listed in the table. In order to enable mutual comparison of the statistics between different geomagnetic elements, besides the values for the magnetic declination given in arc minutes we indicated corresponding values in nanoteslas, too.

Measure of agreement	Geomagnetic element		
	D	*H*	*Z*
CC	0.9998	0.9973	0.9992
RMSE	2.53' (15.3 nT)	16.5 nT	24.2 nT
MAE	1.61' (9.8 nT)	10.7 nT	16.7 nT

at HRB is present in two examples for the magnetic declination (Figs. 2 and 3); the former shows the time series during some disturbed days, the latter displays quiet days with distinct diurnal variations. The model series are

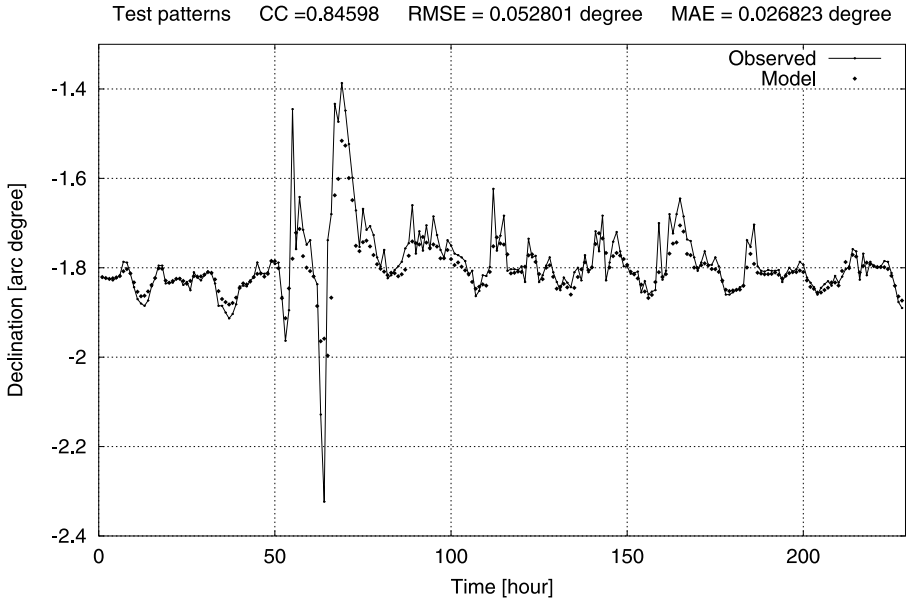

Fig. 2. Time series of both model and observed values of the magnetic declination for period 27/02/1941 – 10/03/1941, during which a geomagnetic storm occurred.

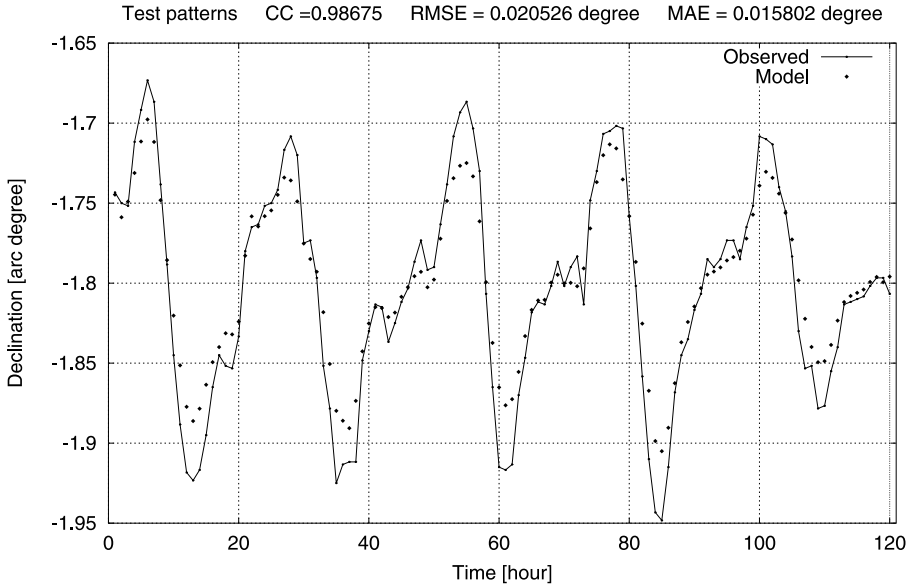

Fig. 3. Time series of both model and observed values of the magnetic declination for quiet period 26/06/1941 – 30/06/1941. A distinct diurnal variation is visible in this summer-time interval.

mildly smoothed as we compare them with the observations – that is a common shortage when modeling by neural networks. Such a good coincidence is not typical for modeled geomagnetic elements H and Z. Nevertheless, the years for which the test data were created coincide with those for which the training and the validation patterns were prepared; therefore, the results of this test should not be overestimated.

An alternative opportunity to estimate the quality of the neural-network model was given by the following: For some years in the first half of the last century the annual means of geomagnetic elements are known, but at the same time the one-hour means have been lost (Fig. 1). We believe that the valuable data from which the annual means were determined were irretrievably lost during the stormy historical events affecting the territory of Slovakia in the 20-th century. For all of those years one-minute values of the geomagnetic elements observed at NGK were preserved, which allowed our neural-networks to produce the corresponding HRB data. The

annual means computed from the model one-minute means could be compared with the HRB annual means which were upheld (Table 2). The upheld data of HRB were also compared with the annual means produced by model IGRF11. For the magnetic declination our neural-network model provided markedly better results. For both horizontal and vertical components, however, the accuracies of the model values are comparable with the IGRF11 model data, but they does not superior them. This is probably due to those long data gaps that occurred in the time series of elements H and Z – the patterns based on such an imperfect data base contained likely insufficient information for more successful training of the neural networks.

Table 2. The accuracy of neural-network model annual means of geomagnetic elements D, H and Z compared with the accuracy of the IGRF11 model for the same geomagnetic elements. The measures of agreement of the IGRF11 model were calculated for the same years as were those of the neural-network model. (Note*: We had only a single value of the difference between the neural-network model value and the observed value of vertical component Z. Thus the values of RMSE and MAE related to Z in the table are mere single absolute differences)

Measure of agreement	Geomagnetic element					
	D [']		H [nT]		Z [nT]	
	NN model	IGRF11	NN model	IGRF11	NN model	IGRF11
RMSE	1.03	9.45	12.6	17.6	12.8*	20.0*
CC	0.75	9.11	11.5	13.7	12.8*	20.0*

We displayed obtainable annual means of the geomagnetic elements of observatories Hurbanovo; Wien Auhof; Munich; Maisach; Fuerstenfeldbruck; and Niemegk, including Potsdam and Seddin referenced to Niemegk, together with the annual means produced by both the IGRF11 and the neural-network models (Figs. 4, 5 and 6 display the observed annual means of geomagnetic elements D, H and Z, respectively.) The neural-network models for elements H and Z (Figs. 5 and 6) turned out to be unreliable in the midst of long data gaps – discontinuities occurred in the time series of H and Z near epochs 1930–1932, which seem to be unnatural and improbable. On the other hand, the neural-network model of the magnetic declination shows a more convincing course (Fig. 4) than that provided by the IGRF11.

The above-mentioned assessment indicates that the neural-network model

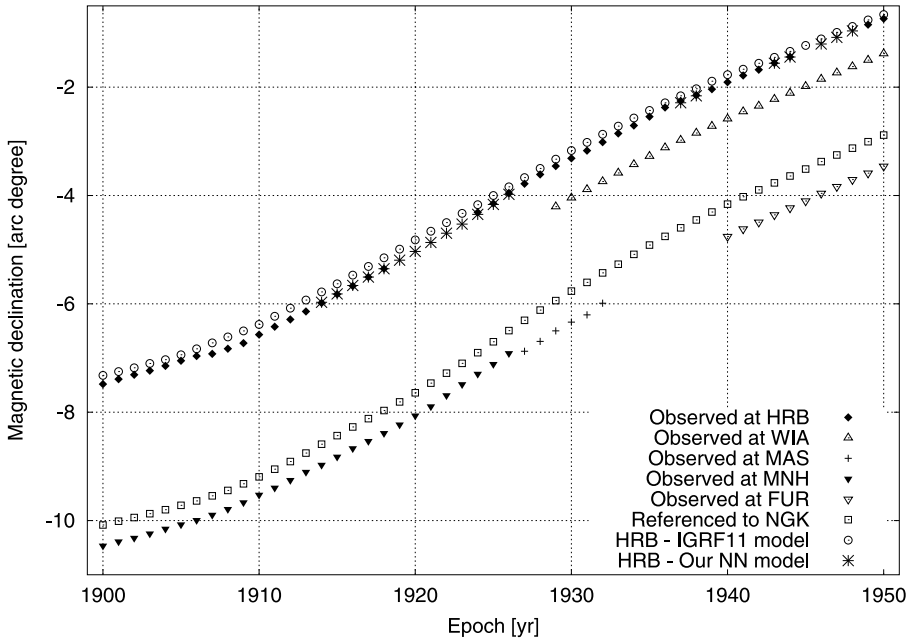

Fig. 4. Time series of annual means of the magnetic declination D computed for observatory HRB from the neural-network model displayed together with the observed annual means of D at observatories HRB, NGK (including observatories at Potsdam and Seddin referenced to NGK), Wien Auhof (WIA), Munich (MNH), Maisach (MAS), and Fuerstenfeldbruck (FUR). The time series of model IGRF11 for HRB is also shown in the picture.

for element D is applicable to substitute for the lost data of the magnetic declination at observatory HRB. The usability of the model for both elements H and Z is limited to a few years close to beginning or end of data gaps.

5. Conclusions

Substitution for the missing one-hour means of geomagnetic elements at observatory HRB was studied in this paper. The proposed method relied on the one-hour means of the geomagnetic field observed at NGK, including data of Potsdam and Seddin referenced to NGK, and it employed artificial

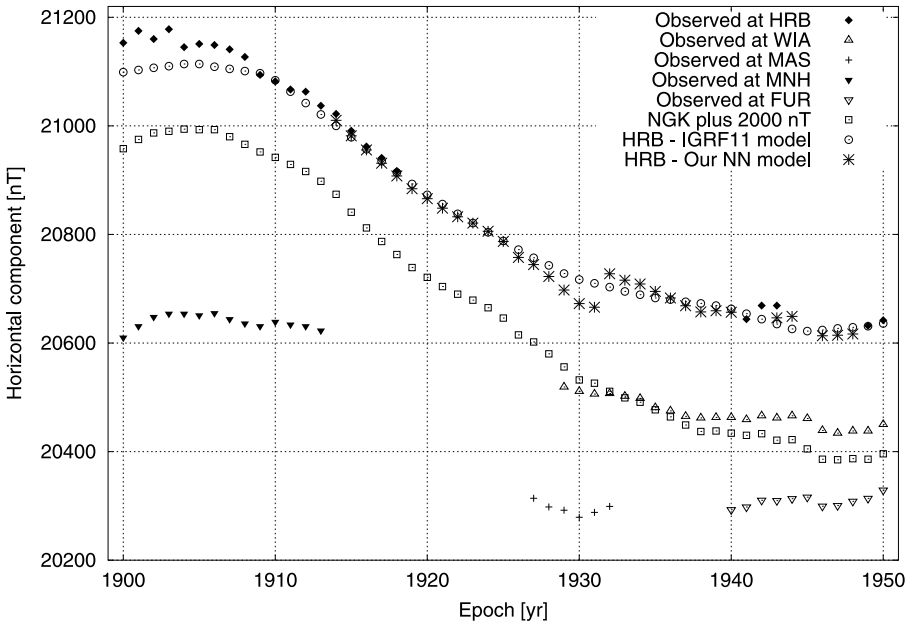

Fig. 5. Time series of annual means of the horizontal component H computed for observatory HRB from the neural-network model displayed together with the observed annual means of H at observatories HRB, NGK (including observatories at Potsdam and Seddin referenced to NGK), WIA, MNH, MAS, and FUR. The time series of model IGRF11 for HRB is also shown.

neural networks. The performance of the method was examined in three different ways: using test patterns, comparing the model annual means with the IGRF11 model quantitatively, and comparing the courses of time series of annual means with data observed at several old observatories besides the the IGRF11 data visually. We found that the neural-network model provided credible results for the geomagnetic declination, for which the data gaps were not so long as were the gaps of the other geomagnetic elements. The results made for both horizontal and vertical components were less satisfactory, particularly in the midst of the long data gap, which occurred between the two World Wars.

The method was used to substitute for lost one-hour means of geomagnetic elements at observatory HRB. The data gaps in question occurred in the first half of the 20-th century, and they took about one or two

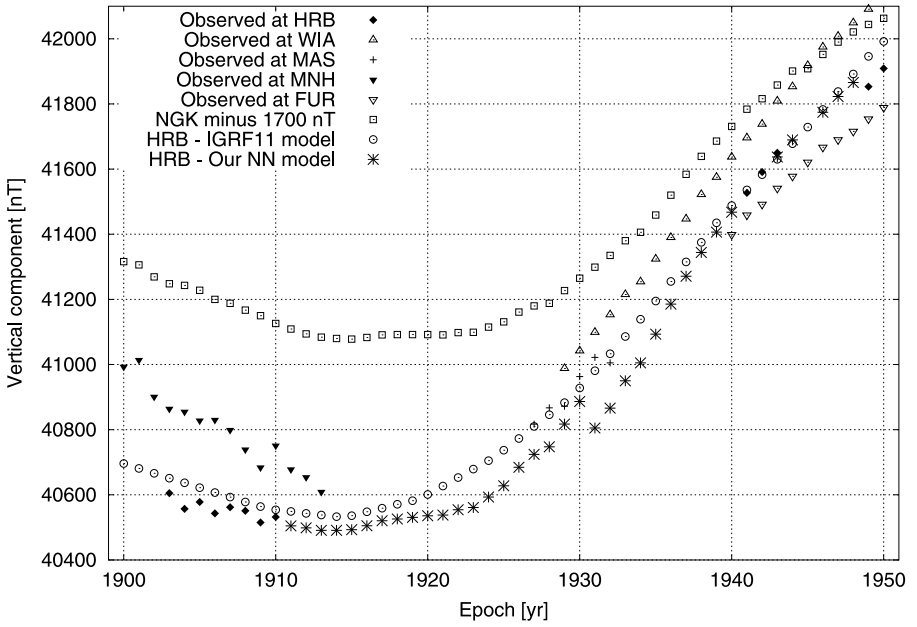

Fig. 6. Time series of annual means of the vertical component Z computed for observatory HRB from the neural-network model displayed together with the observed annual means of Z at observatories HRB, NGK (including observatories at Potsdam and Seddin referenced to NGK), WIA, MNH, MAS, and FUR. The time series of model IGRF11 for HRB is also shown.

decades, depending on the geomagnetic element considered. The substitute geomagnetic elements constitute large amount of data; we made them available on the web page of the Hurbanovo Geomagnetic Observatory (`http://www.geomag.sk/nn-model-old-data`).

In the future, the substitute one-hour means will be utilized to complete information about baselines of the HRB magnetograms for which heretofore the baselines could not be calculated because the absolute measurements disappeared.

Further, we made the time series of annual means of geomagnetic elements D, H and Z at observatory HRB more complete. The network of magnetic observatories was sparse in the middle of the last century; therefore, we believe that these additional data are valuable for the research of geomagnetic secular variations.

Acknowledgments. The results presented in this paper rely on the data collected at Niemegk Magnetic Observatory. We thank GFZ German Research Centre for Geosciences, for supporting its operation. We wish to thank Barbara Leichter for suggesting to use the data of Wien Auhof in this study. We also wish to acknowledge collecting the geomagnetic data by the World Data Centers for Geomagnetism, Kyoto, Japan, and Edinburgh, UK. Further we give thanks to Geophysical Observatory Fuerstenfeldbruck, University of Munich, Germany, for gathering the geomagnetic data of observatories Munich, Maisach and Fuerstenfeldbruck. We appreciate the 11th Generation International Geomagnetic Reference Field Model released by Working Group V-MOD of the International Association of Geomagnetism and Aeronomy. This work was supported by VEGA grant 2/0015/11 of the Scientific Grant Agency of the Ministry of Education of the Slovak Republic and the Slovak Academy of Sciences.

References

Barkhatov N. A., Levitin A. E., Sakharov S. Y., 2002: The method of artificial neuron networks as a procedure for reconstructing gaps in records of individual magnetic observatories from the data of other stations. Geomagnetism and Aeronomy, **42**, 184–186.

Demuth H., Beale M., Hagan M., 2007: Neural Network Toolbox 5, User's Guide. The MathWorks, Natick.

Gurney K., 1997: An Introduction to Neural Networks. UCL Press, London.

Hertz J., Krogh A., Palmer R. G., 1991: Introduction to the Theory of Neural Computation. Addison-Wesley, Reading, MA.

Nørgaard M., 1997: Neural Network Based System Identification Toolbox. Tech. Report. 97-E-851, Department of Automation, Technical University of Denmark, Copenhagen, Denmark.

Ochabová P., Ochaba S., 1977: The origin and development of the Geomagnetic Observatory in Hurbanovo. Contribution of the Geophysical Institute of the Slovak Academy of Sciences, **7**, 13–30.

Prigancová A., Vörös Z., 2001: On 100-year history of the Hurbanovo Geomagnetic Observatory. Contrib. Geophys. Geod., **31**, 1, 1–241.

APPENDIX A

A neural network represents an independent alternative to nonlinear modeling. The functioning of the neural network is based on the ability to learn input-output relations from a database organized in the form of patterns

(*Hertz et al., 1991; Gurney, 1997*). We have used a neural network which is known as feed forward neural network or multilayer perceptron network, which is represented by:

$$g : R^N \rightarrow R^n. \tag{1}$$

It consists of one input layer with N inputs, one hidden layer with q units and one output layer with n outputs. The output of the model with a single output neuron (output layer represented by only one neuron, i.e. $n = 1$) can be expressed according to *Nørgaard (1997)* by:

$$y = f\left[\sum_{j=1}^{q} W_j f\left(\sum_{l=1}^{N} w_{j,l}\, x_l + w_{j,0}\right) + W_0\right], \tag{2}$$

where W_j is the weight between the j-th neuron in the hidden layer and the output neuron, $w_{j,l}$ is the weight between the l-th input and j-th hidden neuron. We have used the same nonlinear activation function for all the neurons of the hidden layer, as well as for the output neuron in the form of the sigmoid

$$f(z) = \frac{1}{(1 + e^{-z})}. \tag{3}$$

For a given set of M patterns we define the normalized mean square error ($NMSE$) by

$$NMSE = \frac{\sum_{s=1}^{M} \left(y_s^{actual} - y_s\right)^2}{M^2}, \tag{4}$$

where y_s^{actual} denotes the actual given output and y_s the neural network output for the s-th pattern. The network is trained to minimize the $NMSE$ by a gradient method.

Contributions to Geophysics and Geodesy Vol. 43/2, 2013 (141–155)

Changes in snowfall/precipitation-day ratio in Slovakia and their linkages with air temperature and precipitation

Nina NIKOLOVA[1], Pavol FAŠKO[2], Milan LAPIN[3], Marek ŠVEC[2]

[1] Faculty of Geology and Geography, St. Kliment Ohridski University of Sofia
Tsar Osvoboditel Blvd. 15, Sofia 1504, Bulgaria; e-mail: nina@gea.uni-sofia.bg

[2] Slovak Hydrometeorological Institute
Jeséniova 17, 833 15 Bratislava, Slovak Republic; e-mail: pavol.fasko@shmu.sk

[3] Faculty of Mathematics, Physics and Informatics, Comenius University
Mlynská dolina, 842 48 Bratislava, Slovak Republic; e-mail: lapin@fmph.uniba.sk

Abstract: Knowledge on snowfall and precipitation variability is one of the most important information about climate changes. The presented study is based on daily data for precipitation totals and new snow cover depths and monthly air temperature from 29 meteorological stations in Slovakia. The aim is to determine to what extent the change of monthly air temperature mean affects the snowfall in the mountainous area of Slovakia. In order to achieve the aim of the research work, the snow days and precipitation days (SD/PD) ratio is calculated for the months from October to April and the trend is investigated. On the basis of correlation analysis it is determined that the main factor for changes in the SD/PD ratio is the mean monthly air temperature while precipitation plays an important role only for the stations with the altitude above 1300 m. Spatial distribution of the changes in the SD/PD ratio for the winter time (December – January – February) during the period 1981–2011 was investigated by cluster analyses. The results show that the stations are grouped according to their geographical location and relief of the territory.

Key words: snowfall, snow days, precipitation, air temperature

1. Introduction

Precipitation is a key element of climate which determines the availability of drinking water and the level of the soil moisture. Changes in precipitation could have a significant impact on society and on different aspects of man activity. Snowfall and snow cover in the mountainous areas are the main

factors also for determining the development of winter sports and tourism. Knowledge about precipitation variability is therefore one of the most important information about climate changes. Meteorological observations show that there is an increasing of extremely weather events during the last decades. This is very likely connected with global climate change both due to natural processes and anthropogenic changes in the composition of the atmosphere and in land use.

Studies on precipitation variability show a decreasing trend of precipitation totals in the Central and Southern Europe and an increasing trend in the Northern Europe. The analysis of the trend of annual precipitation shows an increase of about 20% to 40% in many regions of the Northern hemisphere (*IPCC, 2007*). Despite of this the negative tendency in annual precipitation for the period 1979–2005 has been established in Central and Southern Europe.

Because of importance of the problem and the increasing interest in skiing and winter tourism, the variability of precipitation and snow cover in the mountainous area in Slovakia has received increasing attention in recent years and it was analyzed by many authors. The dependence of snow cover duration and solid precipitation on the altitude was investigated by *Vojtek et al. (2003)*. The authors pointed out the general tendency to decreasing of snow cover duration and solid precipitation occurrence in Slovakia but in the higher altitudes and the northern part of the country there is an opposite trend which is in coincidence with some studies about the Alps (*Beniston et al., 2003*). *Lapin et al. (2007)* pointed out that the variability and trend in snow cover are influenced not only by precipitation but also by air temperature. And this influence is related to the geographical position as altitude and topography. Similar results were showed by *Cazacioc (2007)* who studied the impact of temperature and atmospheric circulation on snow cover duration in Romania. According to *Krasteva and Koleva (2008)* snow pattern depends mainly on circulation conditions and the temperature conditions are decisive factor for the formation and persistence of the snow cover.

The aim of work is to determine to what extent the change of monthly air temperature mean affects the snowfall in the mountainous area of Slovakia. In order to achieve this aim the following tasks have been solved: 1) determination of the number of snowfall (SD) and precipitation (PD)

days for the months from October to April at each of investigated stations; 2) estimation of the trend in the SD/PD ratio; 3) calculation of the correlation between the SD/PD ratio and air temperature means and precipitation totals; and 4) analysis of possible change of the SD/PD ratio according to alternative climate change scenarios for Slovakia up to the year 2100.

The results from this research could be useful for assessment of climate change impacts and especially impacts of precipitation and snowfall variability on winter sports, tourism, water resources or forestry sector.

2. Data and methods

The presented study is based on daily data for precipitation totals and new snow cover depths from 29 meteorological stations in Slovakia. These stations are situated mostly in the mountainous area of the country. Geographical distribution of the stations is shown in Fig. 1 (detailed information is in Table 1). According to the data availability the analysis is made for two periods: 1961–2011 (for 16 stations) and 1981–2011 (for all 29 stations).

The stations are grouped into three groups from the point of view of altitude as follows: 1) with altitude bellow 600 m a.s.l., 2) with altitude between 600 and 1000 m a.s.l., and 3) above 1000 m a.s.l. In order to determine the

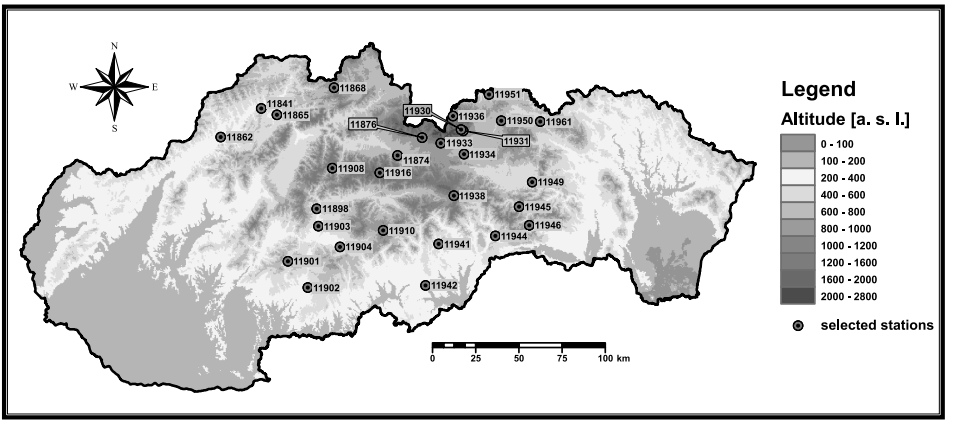

Fig. 1. Geographical distribution of meteorological stations used in the research.

Table 1. List of meteorological stations used in the research

Station number	Station	Altitude [a. s. l.]	Investigated period
11942	Rimavská Sobota	215	1961-2011
11862	Beluša	254	1961-2011
11841	Dolný Hričov, airport	309	1981-2011
11941	Ratková	311	1981-2011
11944	Rožňava	311	1981-2011
11903	Sliač, airport	313	1961-2011
11902	Bzovík	355	1981-2011
11865	Žilina	365	1981-2011
11904	Vígľaš - Pstruša	368	1981-2011
11949	Spišské Vlachy	380	1981-2011
11898	Banská Bystrica -Zelená	427	1961-2011
11951	Červený Kláštor	469	1961-2011
11945	Švedlár	477	1961-2011
11961	Plaveč	485	1961-2011
11950	Podolinec	573	1981-2011
11901	Banská Štiavnica	575	1981-2011
11946	Štós, kúpele	580	1981-2011
11908	Liptovská Osada	616	1981-2011
11874	Liptovský Hrádok	640	1961-2011
11934	Poprad, airport	694	1961-2011
11868	Oravská Lesná	780	1961-2011
11938	Telgárt	901	1961-2011
11876	Podbanské	972	1981-2011
11936	Tatranská Javorina	1013	1981-2011
11910	Lom nad Rimavicou	1018	1961-2011
11933	Štrbské Pleso	1322	1961-2011
11931	Skalnaté Pleso	1778	1961-2011
11916	Chopok	2005	1961-2011
11930	Lomnický Štít	2635	1961-2011

effects of mean air temperature change on snowfall, the monthly data for all investigated stations are used. All needed data were provided by the Slovak Hydrometeorological Institute in Bratislava (SHMI).

The studied area is typical of complex climate varying form moderately warm to moderately cold climate (according to Slovak national climatic classification). The lowest altitudes within the studied area are characterized by moderately warm climate, without regular long-lasting snow cover during the winter, while higher locations are characterized by moderately cold climate, which has regular snow cover during the majority of winter. Great variability of weather linked to the cyclonal activity is typical for the entire region. The highest regions, represented by three stations with the highest altitude have climate characteristic typical for mountain areas of medium latitudes.

Close to big ski resorts are several stations included in the analysis: stations Podbanské and Štrbské Pleso (ski resorts Interski and Solisko from 1350 m a.s.l. up to 1850 m a.s.l.) station Tatranská Javorina (ski resort Ždiar from from 1000 m to 1200 m), stations Skalnaté Pleso and Lomnický štít (ski resort Lomnické sedlo from 1700 m to 2200 m and ski resort Tatranská Lomnica from 800 m to 1700 m) and also station Chopok (ski resort Kosodrevina from 1100 m to 2000 meters, ski resort Jasná from 1200 m to 2000 m.)

The snowfall/precipitation-days ratio (SD/PD) is computed following *Serquet et al. (2011)* methodology. The number of PD and SD is calculated for each of studied meteorological stations and for every month from October to April although at the stations with low altitude there are usually only few snowfall days in October and April. As the SD we consider all days with new snow which formed 1cm or more of new snow cover at the 7h MLT term even if precipitation totals for some of these days are less than one mm. Therefore the number of snowfall days is only some fraction of the number of precipitation days (with daily precipitation total one mm or more). After calculation of monthly number of snowfall and precipitation days the ratio between them for each station and each month is determined. The temporal changes in the SD/PD ratio are determined by linear regression for the periods 1961–2011 and 1981–2011. In order to estimate the effect of temperature change on snowfall days we calculated the correlation between SD/PD and monthly air temperature means and precipitation totals.

Cluster analysis has been applied in order to study spatial and geographical changes in the variability of the SD/PD ratio. This method gives us a tool for classifying the investigated meteorological stations according to the

variability of snowfall and precipitation days. We have applied complete linkage and Euclidean distances for winter season (December – January – February) of the period 1981–2011.

3. Results and discussions

The trend of SD/PD for the period 1961–2011 is investigated on the basis of 16 stations because of availability of complete data series. This trend is negative for most of cases and the values of trend are higher during the winter months (December, January and February), Fig. 2. Similar results were found for Bulgarian mountains by *Petkova and Alexandrov (2012)* who show overall decrease in snow cover duration and maximum snow cover depth during the period 1931–2005. Positive tendencies in the SD/PD changes occur only at some stations in high altitude: (Lomnický Štít (2635 m a.s.l.) – December, January and February and Skalnaté Pleso (1778 m a.s.l.) – January and February but this trend is not statistically significant. On the other hand the negative trend at the stations Chopok (2005 m a.s.l.) and Telgárt (901 m a.s.l.) makes impression and it is statistically significant from December to March. The negative trend for station Chopok, which with its altitude of 2005 m also belongs to the group of the highest mountain stations may be caused by the fact that the most of precipitation at Chopok comes from humid air masses flowing from the southwest and south, including cyclones and frontal pressure waves advancing from the Mediterranean to the northeast. However at the stations Lomnický Štít and Skalnaté Pleso the most of precipitation usually comes from air masses advancing from the northwest and west. Station Chopok also lies more to the south so the influence of warm sector of cyclones or frontal pressure waves advancing from the southwest is more significant, resulting in increase of the portion of mixed and liquid precipitation in the total precipitation during the winter months.

From the first group of stations (with the altitude bellow 600 m a.s.l.) the positive but not statistically significant trend of SD/PD is observed only in a few cases: in February at the stations Švedlár (477 m a.s.l.) and Červený Kláštor (469 m a.s.l.) and in March at the stations Banská Bystrica – Zelená (427 m a.s.l.) and Sliač (313 m a.s.l.). This may be caused by generally more continental climate at stations Švedlár and Červený Kláštor, while at

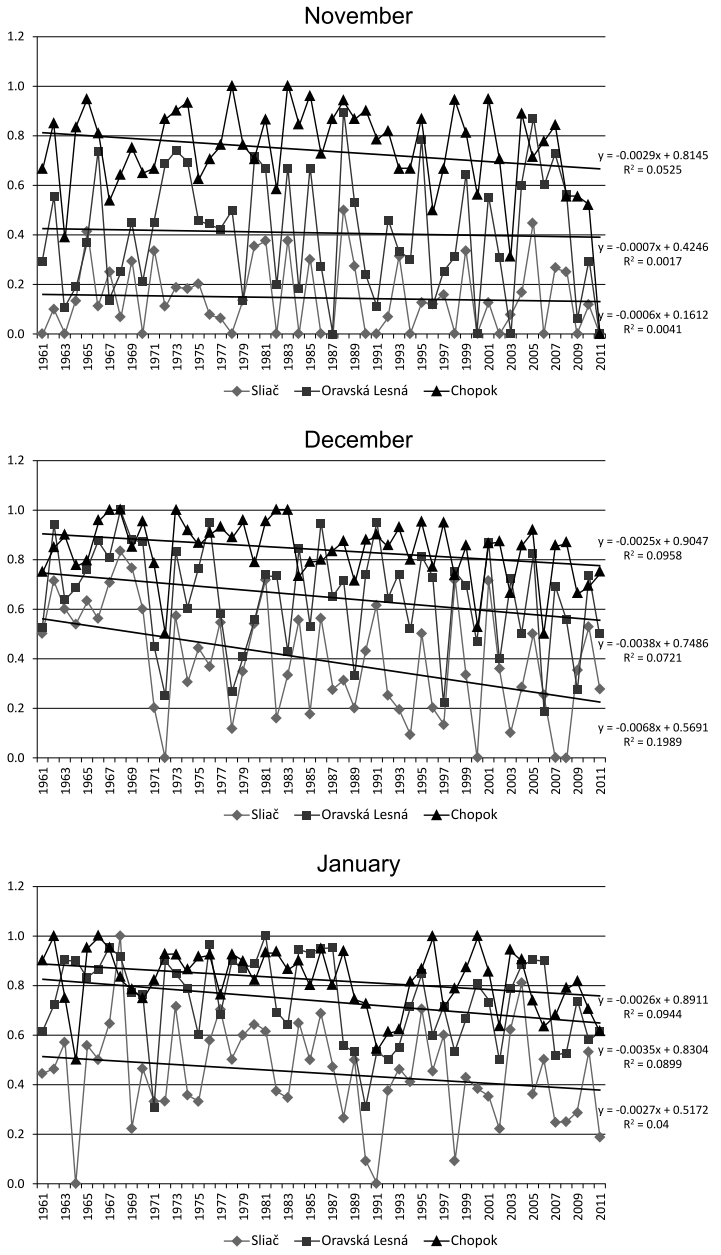

Fig. 2. Continuation on the next page.

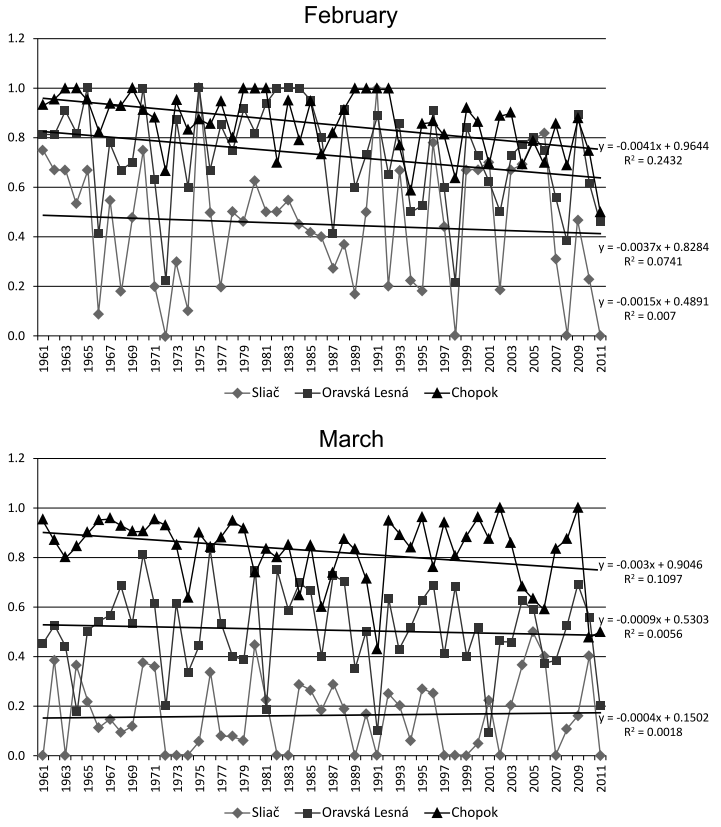

Fig. 2. Ratio of snow days and precipitation days and trend at selected stations for the period 1961–2011.

stations Banská Bystrica and Sliač this can be related to the higher amount of precipitation in the early spring.

There are only few cases with snowfall during April and October in average at the stations with the altitude bellow 600 m a.s.l. (Fig. 3), therefore we did not calculate the trend for these cases (more than 20% of days with no new snow cover in average). The stations with altitude above 600 m have a negative trend of SD/PD in April and October (Fig. 3).

The negative trend in the SD/PD ratio is determined for most of cases at all investigated 29 stations for the period 1981–2011. The main difference for the period 1981–2011 in comparison to the period 1961–2011 is the pos-

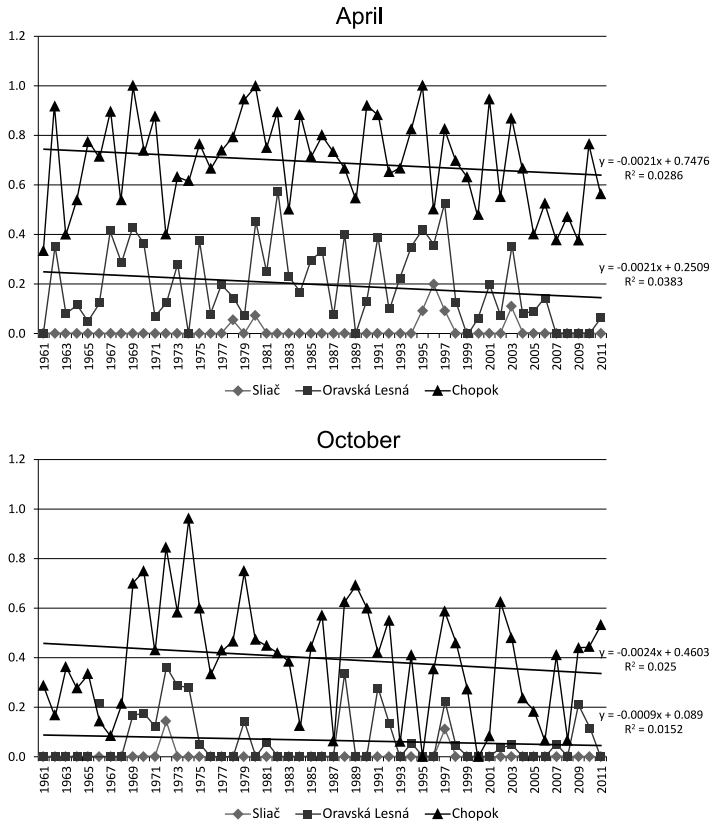

Fig. 3. Ratio of snow days and precipitation days and trend at selected stations for April and October for the period 1961–2011.

itive trend in March for most of stations. Nevertheless the most of stations with altitude above 600 m keep the negative trend of SD/PD in March for the period 1981–2011. All of investigated stations situated above 1000 m a.s.l. have a positive trend of SD/PD in January and February. The positive trend in February is observed also at some stations with altitude less than 600 m a.s.l. as Vígľaš – Pstruša, Ratková, Rožňava and Švedlár. According to the coefficient of determination the trend is statistically significant only in a very few cases. In these cases the continentality of climate mentioned earlier comes into play and at the end of the winter in some enclosed valleys where stations are situated, it causes more stable and colder climate.

The results from correlation analysis between monthly air temperature and the SD/PD ratio and between precipitation and the SD/PD ratio show that the changes in the SD/PD ratio are determined by air temperature means and only for the stations with altitude above 1300 m the correlation between SD/PD and monthly precipitation totals is well established. The correlation coefficients between the SD/PD and monthly air temperature for the period 1961–2011 are negative and for the stations with the altitude up to 1000 m the values are higher for November, December, March and April as for the stations situated in altitudes above 1000 m the highest values occur in January and February. Less significant relation between air temperature and the SD/PD ratio in the territories above 1000 meters in autumn months and in early winter (October, November, December) may be linked to the presence of temperature inversions frequently occurring in Central Europe in this time of the year[1]. This effect is strong and evident at lower altitudes in January and February and it is clearly expressed by the low correlation coefficient between SD/DP and air temperature at stations up to 600 meters. At the stations above 600 meters the trends of rising air temperature are evident and this causes noticeable decrease in the number of days with snow in January, February and March. The correlation between the SD/PD and monthly precipitation totals is positive but the correlation coefficients are statistically significant only for the stations with altitude above 1300 m. High altitude is therefore critical in this case, since during situations with high precipitation it guarantees temperature conditions below the freezing point which are necessary for the presence of snow.

For the period 1981–2011 we studied the correlation between SD/PD, temperature and precipitation at 29 stations (Table 2). The results are similar with those for the period 1961–2011. In low (up to 600 m a.s.l.) and middle (601–1000 m a.s.l.) altitudes the mean temperature affects the changes in the SD/PD mainly at the beginning and the end of the winter as well as in October and April. In the higher part of study area a statistically significant correlation between the SD/PD and air temperature is established for the January – April months nevertheless some stations with the

[1] Temperature inversions are caused by retaining layers of the atmosphere where there is temperature rise with the altitude, which is inconsistent with the standard conditions in the atmosphere. If in the analysed period and area, are these inversions presented very frequently, they can affect the average monthly air temperature.

Table 2. Correlation between air temperature and SD/PD ratio for the period 1981–2011

Station	Altitude [a. s. l.]	Correlation of temperature and SD/PD						
		X	XI	XII	I	II	III	IV
Rimavská Sobota	215	**-0.53**	**-0.72**	**-0.54**	0	-0.31	**-0.39**	**-0.57**
Beluša	254	**-0.68**	**-0.72**	**-0.52**	-0.32	**-0.37**	**-0.59**	**-0.71**
Dolný Hričov, airport	309	**-0.69**	**-0.64**	**-0.64**	**-0.44**	**-0.38**	**-0.66**	**-0.78**
Ratková	311	**-0.47**	**-0.5**	-0.48	-0.25	-0.3	-0.33	**-0.73**
Rožňava	311	**-0.51**	**-0.56**	**-0.61**	**-0.44**	-0.29	**-0.49**	**-0.75**
Sliač, airport	313	**-0.39**	**-0.63**	**-0.54**	-0.23	**-0.41**	**-0.58**	**-0.7**
Bzovík	355	**-0.56**	**-0.49**	**-0.5**	-0.2	**-0.5**	**-0.42**	**-0.68**
Žilina	365	**-0.62**	**-0.68**	**-0.72**	**-0.51**	-0.12	**-0.66**	**-0.76**
Vígľaš - Pstruša	368	-0.35	**-0.63**	**-0.68**	**-0.4**	-0.27	-0.43	**-0.7**
Spišské Vlachy	380	**-0.63**	**-0.6**	**-0.66**	-0.36	**-0.49**	**-0.67**	**-0.65**
Banská Bystrica, Zelená	427	**-0.54**	**-0.55**	**-0.65**	**-0.39**	-0.19	-0.36	**-0.72**
Červený Kláštor	469	**-0.72**	**-0.64**	**-0.81**	**-0.51**	-0.33	**-0.55**	**-0.43**
Švedlár	477	-0.28	**-0.54**	**-0.77**	**-0.52**	-0.09	**-0.59**	**-0.68**
Plaveč	485	**-0.42**	**-0.66**	**-0.6**	**-0.51**	-0.31	**-0.68**	**-0.65**
Podolinec	573	**-0.49**	**-0.56**	**-0.64**	**-0.71**	-0.3	**-0.77**	**-0.6**
Banská Štiavnica	575	**-0.5**	**-0.67**	**-0.65**	**-0.4**	-0.18	**-0.59**	**-0.57**
Štós, kúpele	580	**-0.46**	**-0.7**	**-0.68**	**-0.56**	**-0.4**	**-0.62**	**-0.65**
Liptovská Osada	616	**-0.61**	**-0.66**	**-0.69**	**-0.41**	**-0.33**	**-0.67**	**-0.45**
Liptovský Hrádok	640	**-0.45**	**-0.67**	**-0.61**	**-0.63**	**-0.37**	**-0.66**	**-0.53**
Poprad, airport	694	-0.31	**-0.63**	**-0.52**	**-0.68**	**-0.54**	**-0.68**	**-0.5**
Oravská Lesná	780	**-0.61**	**-0.56**	**-0.59**	**-0.73**	**-0.52**	**-0.66**	**-0.51**
Telgárt	901	**-0.52**	**-0.45**	**-0.54**	**-0.58**	**-0.59**	**-0.61**	**-0.6**
Podbanské	972	**-0.58**	**-0.55**	**-0.61**	**-0.72**	**-0.7**	**-0.61**	**-0.65**
Tatranská Javorina	1013	**-0.42**	-0.19	-0.5	**-0.74**	**-0.73**	**-0.65**	**-0.57**
Lom nad Rimavicou	1018	**-0.56**	**-0.55**	**-0.66**	**-0.63**	**-0.49**	**-0.45**	**-0.72**
Štrbské Pleso	1322	**-0.46**	-0.07	**-0.46**	**-0.7**	**-0.78**	**-0.65**	**-0.5**
Skalnaté Pleso	1778	-0.26	0.02	-0.21	**-0.63**	**-0.66**	**-0.65**	-0.07
Chopok	2005	**-0.39**	-0.1	-0.07	**-0.71**	**-0.58**	**-0.74**	**-0.38**
Lomnický Štít	2635	0.06	0.16	-0.18	**-0.36**	**-0.62**	**-0.53**	-0.33

Statistically significant coefficients are in Bold

altitude between 1013–1322 m show good correlation between the SD/PD and temperature for the October – December months as well. The most noticeable are high negative correlation values for the month of April and

stations below 600 meters. In April also the most significant increases in air temperature at selected stations were recorded since 1981. In the high mountain areas this does not apply, because this period is just after the culmination of winter in these areas, therefore despite of the increase in air temperature since 1981, local conditions still cause precipitation to fall in the form of snow. The correlation analysis shows that for the period 1981-2011 precipitation totals are important for changes in the SD/PD at the stations in altitude above 1000 m. Only at a few stations with altitude lower than 1000 m correlation between the SD/PD and precipitation is statistically significant for the months from February to April. This tighter relationship may result from the geographic location of some of these stations and from the specific dependencies between monthly rainfall and number of days with snow.

Spatial distribution of changes in the SD/PD ratio for the winter time (December – January – February) during the period 1981–2011 was investigated also by cluster analyses. By means of complete linkage and Euclidean distances we clustered stations that had similar features during the period 1981–2011 in regards of changes in the SD/PD ratio (Fig. 4). The stations are classified into four groups. In two of the groups, three and four subgroups of stations are determined.

The first group of stations ("green" in Fig. 4) includes 15 stations divided in four subgroups as follows: 1) Rimavská Sobota and Bzovík; 2) Telgárt; Poprad and Spišské Vlachy; 3) Ratková, Rožňava, Vígľaš – Pstruša, Banská Štiavnica, Banská Bystrica – Zelená and Sliač, and 4), Beluša, Žilina and Dolný Hričov. The second group (Fig. 4, "blue") includes 10 stations situated mainly in altitude above 600 m. Three subgroups of stations are in this group: 1) Tatranská Javorina and Skalnaté Pleso; 2) Štrbské Pleso and Podbanské, and 3) Červený Kláštor, Štós – kúpele, Lom nad Rimavicou, Liptovský Hrádok, Plaveč and Oravská Lesná. Only two stations (Podolinec and Švedlár) are in the third group of stations (Fig. 4 "orange") and other two stations (Lomnický Štít and Chopok) are included in the fourth group (Fig. 4 "red").

The results of cluster analysis show that the main factor for including stations into a given cluster is geographical location, relief and distance between the stations.

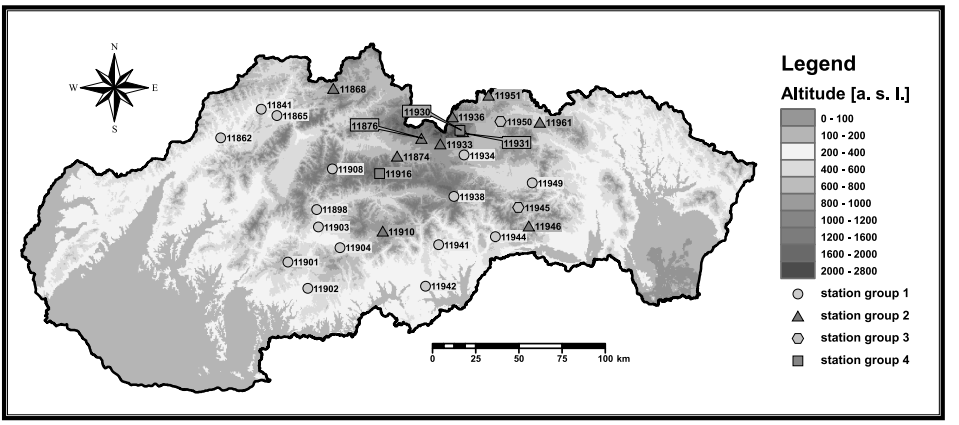

Fig. 4. Groups of stations according to the spatial distribution of the changes in SD/PD ration for the winter-time during the period 1981–2011.

4. Conclusion

The actuality of presented research is determined by the facts that snowfall and snow cover in the mountainous areas are one of the main factors for determining the development of winter sports and tourism. From the other side, these elements have also importance for availability of water resources and in general hydrologic balance as well.

The following conclusion can be pointed out on the basis of the investigation of the SD/PD ratio in the mountainous part of Slovakia for the period 1961–2011.

The trend of SD/PD for the period 1961–2011 is negative for most of cases and the values of trend are higher during the winter months (December, January and February). This negative trend in the SD/PD ratio is determined for most of cases at all investigated 29 stations for the period 1981–2011. The main difference for the period 1981–2011 in comparison to the period 1961–2011 is the positive trend in March for the most of stations.

There are only few cases with snowfall during April and October at the stations with the altitude bellow 600 m a.s.l. The stations with altitude above 600 m have a negative trend of SD/PD in April and October.

The results from the correlation analysis between monthly air temper-

ature, precipitation and the SD/PD ratio show that the changes in the SD/PD ratio are determined predominantly by air temperature. Only for the stations with altitude above 1300 m the correlation between SD/PD and monthly precipitation totals is well established and statistically significant.

The results of cluster analysis of the winter-time SD/PD ratio for the period 1981–2011 show that the main factor for inclusion stations into a given cluster is the geographical location, relief and distance between the stations.

Acknowledgments. The authors would like to express their gratitude to the Slovak Hydrometeorological Institute for providing the meteorological data for the research work. The research was performed during the short-term research visit of assoc. prof. N. Nikolova at the Comenius University, and SHMI Bratislava, Slovakia, in the frame of bilateral cooperation in the field of education, science and culture between Bulgaria and Slovakia.

References

Beniston M., Keller F., Goyette S., 2003: Snow pack in the Swiss Alps under hanging climatic conditions: an empirical approach for climate impacts studies. Theoretical and Applied Climatology, 73, 19–31.

Cazacioc L., 2007: Spatial Differences over Romania of the Snow Cover Variability in Relationship to Temperature and Atmospheric Circulation. In: 29-th International Conference on Alpine Meteorology. Extended Abstracts. Oral Sessions, 1, Toulouse, Meteo France.

IPCC Climate Change, 2007: Synthesis Report. Contribution of Working Group I, II and III to the Fourth Assessment Report of the International Panel on Climate Change (Core Writing Team, Pachuari R. K. and Reisinger A., eds.). IPCC, Geneva, Switzerland.

Krasteva Z., Koleva E., 2008: Analysis of Winter Climatological Parameters in Rila-Mountain. BALWOIS 2008 – Ohrid, Republic of Macedonia – 27–31, May 2008. `http://balwois.com/balwois/administration/full_paper/ffp-1114.pdf` (Accessed by 3 March 2012).

Lapin M., Faško P., Pecho J., 2007: Snow Cover Variability and Trend in the Tatra Mountains in 1921–2006. In: 29-th International Conference on Alpine Meteorology. Extended Abstracts. Oral Sessions, 1, Toulouse, Meteo France, 175–178.

Petkova N., Alexandrov V., 2012: Snow Cover in Bulgarian Mountainous Regions: Observed Variations and Future Activities. BALWOIS 2012 – Ohrid, Republic of Macedonia – 28 May, 2 June 2012. `http://balwois.com/2012/USB/papers/1062.pdf` (Accessed by 3 March 2012).

Serquet G., Marty Ch., Dulex J. P., Rebetez M., 2011: Seasonal trends and temperature dependence of the snowfall/precipitation-day ratio in Switzerland. Geoph. Res. Let., **38**, L07703, doi:10.1029/2011GL046976

Vojtek M., Faško P., Šťastný P., 2003: Some selected snow climate trends in Slovakia with respect to altitude. Acta Meteorologica Univ. Comenianae, XXXII. 17–2.

Contributions to Geophysics and Geodesy Vol. 43/2, 2013 (157–177)

Changes of characteristics of daily precipitation and runoff in the High Tatra Mountains, Slovakia over the last fifty years

Svetlana BIČÁROVÁ[1], Ladislav HOLKO[2]

[1] Geophysical Institute of the Slovak Academy of Sciences
Meteorological Observatory Stará Lesná
059 60 Tatranská Lomnica, Slovak Republic; e-mail: bicarova@ta3.sk

[2] Institute of Hydrology of the Slovak Academy of Sciences
Ondrašovská 16, 031 05 Liptovský Mikuláš, Slovak Republic; e-mail: holko@uh.savba.sk

Abstract: The article presents the results of the analysis of time series of daily precipitation and runoff at selected places in the highest part of the Western Carpathians. It was focused on both wet and dry periods in precipitation and runoff data series. The precipitation data were analysed for a period 1961–2010. They revealed a significant increase of the number of days with daily precipitation 40–60 mm. Trend analysis for 67 analysed flow characteristics did not show statistically significant changes over the studied period. The focus was given particularly to the characteristics of the maximum and minimum flows, i.e. 3- and 7- day minimum flows, 1-, 3- and 7-day maximum flows. We found an increase of flows classified as small floods in two of three mountain catchments in the study area in the last decade (2001–2010). It may be linked to the above increased number of days with daily precipitation reaching 40–60 mm.

Key words: time-series analysis, daily precipitation, daily runoff, wet and dry periods, mountains

1. Introduction

Climate-related risks and occurrence of extreme weather events during last years is understood as a serious problem in many countries of the world. In 2010, 385 natural (climatological, hydrological, meteorological and geophysical) disasters were reported worldwide. They killed 297 000 persons, affected more than 217 million others and caused over US$ 123.9 billion economic damages (*Guha-Sapir et al., 2011*). The United Nations International

Strategy for Disaster Reduction (*UN/ISDR, 2010*) emphasizes the necessity to improve the knowledge-base methods and integrated frameworks for the assessment of hazards, vulnerability and risk at national and regional level.

In Europe, mountain regions along with coastal zones, wetlands and the Mediterranean region are particularly vulnerable (*EEA, 2005*). Study of extreme meteorological phenomena by *Ustrnul and Czekierda (2009)* documented occurrence of the heaviest rainfalls in southern mountainous part of Poland. *Ceglar et al. (2009)* concluded that extreme precipitation events are frequent in mountains of the north-western Slovenia. *Lapin et al. (2003)* noted that interrelations among atmospheric circulation indices, air pressure and precipitation totals show great importance of changing atmospheric circulation on climate in Central Europe, mainly in the areas with complex topography. Climate in the northern mountainous part of Slovakia has become more humid and some shifts of climatic regions and subregions towards the higher altitudes were registered in the 20$^{\text{th}}$ and at the beginning of the 21$^{\text{st}}$ century (*Melo et al., 2009*).

Interactions between land and atmosphere are of fundamental importance for hydrological cycle. Climate and weather drive a precipitation process in the atmosphere, while the landscape features determine distribution of water on the land surface. There are evidences of the impact of human activities and climate on changing hydrological cycle, including the observed large-scale patterns of precipitation changes over the 20$^{\text{th}}$ century (e.g. *IPCC, 2007*). Changes in precipitation and temperature lead to changes in runoff and water availability. *IPCC (2007)* states that runoff is projected with high confidence to increase by 10 to 40% by mid-century at higher latitudes and decrease by 10 to 30% over some dry regions at mid-latitudes due to decrease in rainfall and higher rates of evapotranspiration.

While the analyses of measured data clearly indicate recent changes in air temperatures, conclusions on changes of precipitation and runoff are not so consistent (*Blöschl and Montanari, 2010*). *Mudelsee et al. (2003)* argued that observations in Europe did not show a clear increase in flood occurrence rate during the last decades. *Robson (2002)* concluded that in the UK there have been trends towards more protracted high flows in the last 30–50 years, but they could be accounted for as part of climatic variation rather than climate change. *Holko et al. (2006)* did not find changes in discharges from selected small mountainous catchments of central Slovakia,

northern Czech Republic and central Germany. A number of studies related to changes in streamflow were performed in Switzerland. *Birsan et al. (2005)* demonstrated complex changes in streamflow regime in Switzerland (48 stations), especially in the more recent periods. Annual runoff increased due to increases of winter, spring and autumn runoff while the behavior in summer showed both upward and downward trends. The authors concluded that mountain areas are the most vulnerable from the point of view of streamflow change. *Allamano et al. (2009)* reported that large floods in mountain basins of the Swiss Alps are now more frequent than in the past. They have found a significant increase of flood peaks during the last century and attributed it to simultaneous increase of air temperature and precipitation. *Schmocker-Fackel and Naef (2010)* found out that annual series of streamflow from Switzerland (83 stations) showed only few negative trends. The number of stations with positive trends was especially high, when the period of 2001–2007 was included into the analysis. Over the last 150 years, periods with a large amount of larger floods (return period over 10-years) alternated with periods poor in floods. They have also documented spatial differences in the frequency of floods and indicated that changes in large-scale atmospheric circulation might be responsible for the fluctuations in flood frequency. *Cunderlik and Ouarda (2009)* reported on weak signals of climate variability and/or change present in the timing of floods in Canada during the last three decades. Most of the significant trends in the timing of spring snowmelt floods were the negative ones, i.e. earlier flood occurrence, found in the southern part of Canada. They did not find significant trends in the timing of autumn rainfall floods. However, the significance of the autumn rainfall-dominated flood season has been increasing in several analyzed watersheds. *Villarini and Smith (2010)* found little evidence for increasing flood peaks in the eastern USA. *Halmová and Pekárová (2011)* concluded that daily discharges (1928–2008) of the Belá river draining the westernmost part of the High Tatra Mts., Slovakia did not show important changes in the number of extreme floods and the temporal extent of droughts.

The objective of this paper was to investigate temporal variability of daily precipitation and runoff in the highest part of the Carpathian Mountains (the High Tatra Mts., Slovak Republic) over the last almost 50 years. Changes in occurrence of potentially hazardous rainfall events (from the

point of view of possible flood generation), and wet and dry periods in both precipitation and runoff data series were examined as well.

2. Study area and data

The High Tatra Mountains are located in northern part of Slovakia on the border with Poland (Fig. 1). They are the highest part of the whole Carpathians. The main ridge of the High Tatra Mts. has the west-east direction. It is 26 km long and 17 km wide. Its mean elevation is about 2300 m a.s.l. and it varies from 2200 m a.s.l. (saddles) to 2400 m a.s.l. (peaks).

Šamaj (1973) reported that the first meteorological measurements (air temperature) in the High Tatra Mts. and its vicinity were made in the year 1720. The oldest documented observations are from the years 1789–1800 and systematic measurements are archived since 1873. Meteorological measurements in Starý Smokovec started in 1875. Stations in Tatranská Lomnica, Poprad and Štrbské Pleso were established at the turn of the 19^{th} and 20^{th} centuries. Important high mountain stations were established between 1936 and 1940 at the Kasprowy Wierch mountain (Poland), the Skalnaté Pleso lake and at the Lomnický štít mountain (all above information from *Šamaj, 1973*).

We analysed daily precipitation from six stations located in the central, western and eastern parts of the Slovak High Tatra Mts. (Fig. 1). Data from years 1961–2010 were used in the study. The altitude of the precipitation stations varied from 694 to 2635 m a.s.l., mean annual precipitation ranged from 600 to 1500 mm (Table 1). Precipitation was measured by standard rain gauge of the Czechoslovak meteorological service with orifice 500 cm^2 that is elevated 1 m above the ground. All stations are part of the national network of the Slovak Hydrometeorological Institute (SHMI).

The High Tatra Mts. create part of the European water divide between the Black Sea and the Baltic Sea. Most of the area in Slovakia is drained by the Poprad river which is one of only two Slovak rivers that are in the Baltic Sea basin. The western part of the High Tatra Mts. is drained by the longest Slovak river Váh that flows to the Danube river and eventually to the Black Sea. In this study we focused on the upper Poprad river catchment and

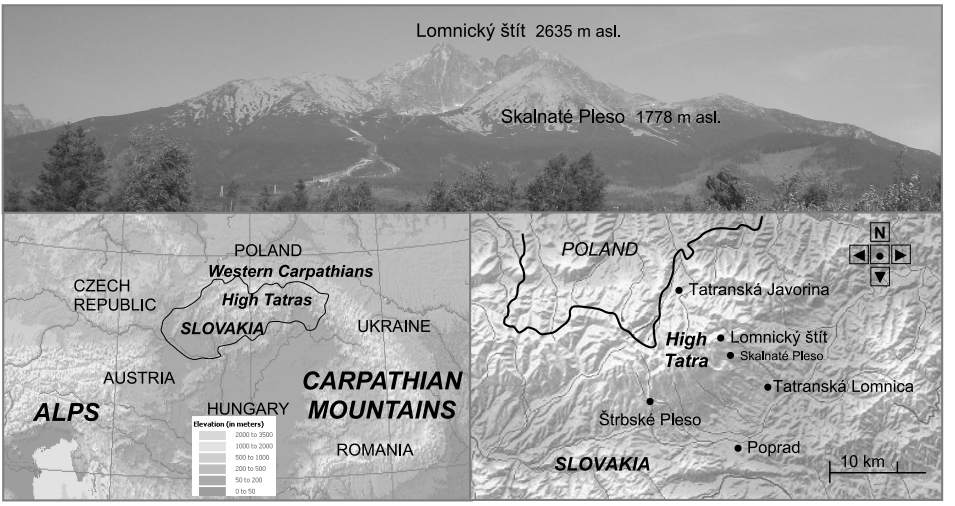

Fig. 1. The geographical position of the High Tatras in the Carpathian Mountains (left) and location of precipitation stations (right).

its subcatchments. While meteorological measurements in the High Tatra Mts. started already in the 19th century, hydrological measurements in the Poprad river catchment are much younger. The gage at Poprad-Matejovce was installed in 1921 (*Pacl, 1973*) and other gages in the area were installed in the following decades. We have analysed daily runoff from four catch-

Table 1. Precipitation stations used in the study; P is the mean annual precipitation (1961–2010)

Position of measurement sites in the High Tatra Mts.			Latitude	Longitude	Altitude [m a.s.l.]	P [mm]
Central part The Skalnatá dolina valley	LS	Lomnický štít	49°12' 00" N	20°13' 00" E	2635	1496
	SkP	Skalnaté Pleso	49°11' 22" N	20°14' 03" E	1778	1345
	TL	Tatranská Lomnica	49°09' 46" N	20°17' 17" E	827	794
The Popradská kotlina basin	PP	Poprad	49°04' 06" N	20°15' 58" E	694	598
Western part	StP	Štrbské Pleso	49°07' 09" N	20°03' 26" E	1354	1025
Eastern part	TJ	Tatranská Javorina	49°15' 02" N	20°09' 29" E	1030	1303

ments in the High Tatra Mts. area that had data series comparable in length with those of precipitation. Three of them were smaller catchments nested within the fourth one – the Poprad river at Matejovce (Fig. 2). The data series did not have the same length, because the measurements in the catchments started in different years. Furthermore, measurements at Poprad-Matejovce had to finish at the end of 2009 due to infrastructure construction. Therefore, the daily runoff was analysed only for hydrological years 1963–2010 (1963–2009 for the Poprad-Matejovce catchment). Hydrological year in Slovakia starts on 1st November and ends on 31st October. Basic characteristics of the catchments are given in Table 2. Mean annual runoff in the catchments varied between 219 and 504 mm. Mean evapotranspiration calculated from the water balance equation varied approximately between 351 and 572 mm (*Holko et al., 2009*).

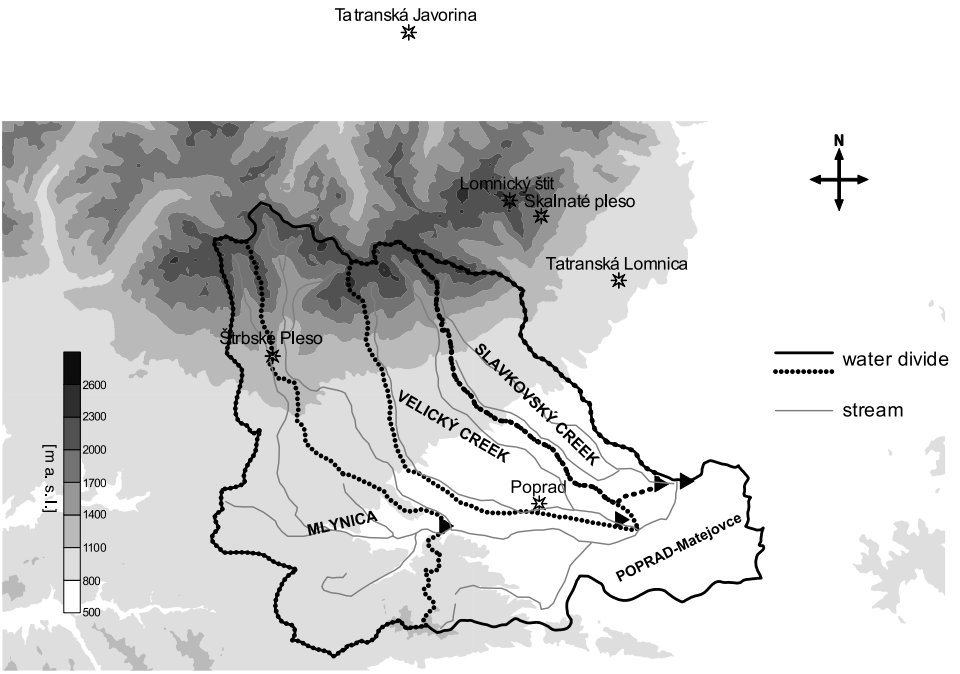

Fig. 2. Water divides of the studied subcatchments of the upper Poprad river and precipitation stations (asterisks); the stream gages are marked by the triangles.

Table 2. Studied catchments and their basic characteristics derived from gridded digital maps with resolution 50 m, R is mean annual runoff for the period given in the table; C is runoff coefficient, NA means there were no data available to calculate catchment mean precipitation

Catchment – gage	Area [km^2]	Mean altitude [m a.s.l.]	Mean slope [°]	Runoff data from period	R [mm]	C [–]
Mlynica – Svit	83	991	9.2	1963 – 2010	219	0.28
Velický creek – Veľká	58	1094	9.3	1963 – 2010	505	0.59
Slavkovský creek – Matejovce	43	1017	8.6	1963 – 2010	358	0.43
Poprad – Matejovce	315	1018	9.2	1963 – 2009	399	0.50

3. Methodology

The purpose of the work was to analyze both precipitation as the input into the hydrological cycle of a catchment and runoff representing integrated result of all processes acting in a catchment. The rationale behind including runoff is that runoff and its extremes, i.e. floods and droughts, have a direct impact on catchment environment including human society. It is therefore important to study the evolution of this phenomenon over time.

Statistical analysis was used to obtain characteristics of daily precipitation and runoff and their variability in the studied period. Daily runoff was expressed for some analysis as runoff depth in millimeters, e.g. to allow intercomparison of the catchments and comparison with precipitation.

Directly measured data are the best descriptors of natural phenomena. However, they inevitably include uncertainties. In case of precipitation and runoff the uncertainties or even errors may arise, e.g. from measurement methods, equipment, changes of sensors, replacement of stations, etc. Therefore, the analysis of the long-time data series should be accompanied by the tests of homogeneity. A number of methods were used to test the homogeneity of meteorological data (*Kang and Yousuf, 2012*). Bivariate test, standard normal homogeneity test (SNHT), von Neuman ratio test, Pettit test, Kruskal-Wallis test are perhaps the ones which have been mostly used in the analysis of precipitation and runoff data (e.g. *Firat et al., 2010; Kang and Yousuf, 2012*). In this study, the homogeneity of the precipitation data was tested by means of the SNHT Alexandersson tests (*Alexandersson, 1986*) and Bivariate test Maronny and Yohaie (*Maronna and Yohai, 1978*)

method using the ProClimDB software (*Štepánek, 2010*). Homogeneity of runoff data was tested by the von Neumann test, because the data did not have normal distribution required for the SNHT test.

Numerous indices are used in different studies to monitor changes of daily precipitation (e.g. *Zhang et al., 2011*). In this study we have calculated 1^{st} and 3^{rd} quartiles (q1, q3), median, mean, 95^{th} and 99^{th} percentiles (p95, p99) for the daily precipitation and daily runoff data. They were used to characterize the differences among the precipitation stations and catchment runoff from different subcatchments. Quartiles are special percentiles corresponding to 25% (q1) and 75% (q3) cumulative relative frequency. Second quartile or median is the number in the middle of sorted dataset. The 95^{th} (99^{th}) percentile is the value of precipitation or runoff such that 95% (99%) of the relevant population is below that value.

Analysis of temporal variability of precipitation and runoff focused on dry and wet periods. In case of precipitation we counted the frequency of successive periods without precipitation (dry periods) and frequency of successive periods with precipitation (wet periods), respectively. The results were then summarized for each station and duration of dry and wet periods in the following categories:

- ST (short-term wet/dry period) with duration in range between 1 and 5 days,
- MT (middle-term wet/dry period) with duration in range between 6 and 10 days,
- LT (long-term wet/dry period) with duration more than 10 days.

Temporal evolution of the wet and dry periods was evaluated for decades (1961–1970, 1971–1980, 1981–1990, 1990–2000, 2001–2010). Relation between decadal wet/dry period frequency and decadal precipitation totals was examined by correlation analysis and the P-values (see below).

Daily discharge data (i.e. catchment runoff expressed in m^3s^{-1}) was analysed with the IHA (Indicators of Hydrologic Alteration) software (*The Nature Conservancy, 2009*). Daily discharges for hydrological years 1963–2010 (1963–2009 for Poprad-Matejovce) were processed as one period. The IHA provides a number of statistics and metrics. After the non-parametric analysis of the data we first found all characteristics that had exhibited

a statistically significant trend in the studied period. The criterion was that the coefficient of correlation (linear regression between time and studied statistics) exceeded the value of 0.55 and the P-value was below 0.05. Second analysis was focused on characteristics of minimum and maximum discharges (3– and 7– day minimum flows, 1–, 3– and 7–day maximum flows) and the following flow components:

- duration of extreme low flows – extreme low flow was the flow less than or equal to the 10th percentile of daily flows,
- duration of small floods – a small flood was a flow event that had flows exceeding the 75^{th} percentile of the daily flows and the return interval of the peak flow greater than 2 years,
- duration of high floods – a high flood was a flow event that had flows exceeding the 75^{th} percentile of the daily flows and the return interval of the peak flow greater than 10 years.

Classification of the Integrated Warning Service System (*IWSS*) of the Czech Hydrometeorological Institute (`http://pocasi.chmi.cz/en/`) was used for evaluation of the number of potentially dangerous rainfalls. Only data from warmer period of the year (May to October) were analyzed, because solid precipitation may be rather frequent in the High Tatra Mts. in the other months. Three degrees of the risk were determined:

1. low risk – daily precipitation between 40 and 60 mm (occurrence of potentially dangerous situation),
2. high risk – daily precipitation from 60 to 90 mm (potential of material damage on large area),
3. extreme risk – daily precipitation above 90 mm (potential of enormous material damage and hazard to human life).

The IWSS criteria assess the risk of damages in human society including disruption of settlements, commerce and transport due to flooding, waterlogging and erosion of soil, contamination of surface and groundwater sources, increased risk of injuries, infectious, skin diseases and deaths (public health).

4. Results and discussion

4.1. Homogeneity of the data series

Data quality control of the precipitation series did not indicate any suspicious values. Detection of inhomogeneities was done on monthly, seasonal and annual precipitation totals. The test found great inhomogeneity at station Lomnický štít mountain in 1991. Correction of the inhomogeneity was done with the help of reference series from neighbouring stations (SkP, TL, PP, StP, TJ). After the correction, correlation between homogenized values of annual precipitation for the Lomnický štít mountain and reference series slightly increased (+0.044). The increase was bigger for the winter (+0.100) than for the summer (+0.008) periods (*Mačutek et al., 2011*).

All runoff data series exhibited inhomogeneities. Data from the Mlynica, Velicky creek and Poprad-Matejovce catchments had inhomogeneities in the first 7, 5 and 5 years, respectively. Data from the Slavkovsky creek catchment had inhomogeneities in the first 17 and last 5 years. Since the independent homogeneous data from a neighbouring catchment were not available, we have excluded the first seven years from the runoff data series of Mlynica, Velicky creek and Poprad-Matejovce. Data from the Slavkovsky creek were not further analyzed. The High Tatra Mts. region was hit by an extraordinary wind in November 2004 that caused spacious forest destruction. The highest windfall-induced deforestation occurred in the Slavkovsky and the Velicky creek catchments. Although the data measured in the following years did not indicate significant impacts on the runoff regime (*Holko et al., 2009*), the homogeneity test performed here indicated inhomogeneities in the runoff data series of the Slavkovsky creek.

4.2. Ranges of measured precipitation and runoff

The Box-Whisker plots in Figs. 3 and 4 show the ranges of daily precipitation and runoff. Precipitation at the lowest altitude (PP) had the smallest range (Fig. 3). The highest ranges and the highest number of outliers were not observed at the highest station (LS). They occurred at station of TJ which is on the windward side of the High Tatra Mts. and at station SkP which is located at high altitude on the leeward side of the Lomnický Štít mountain. Mean values of precipitation did not significantly vary among

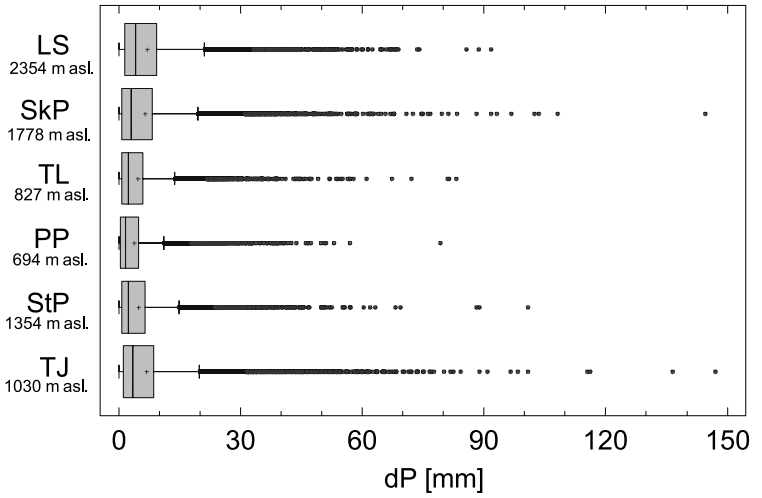

Fig. 3. Box-Whisker plot of daily precipitation at the studied stations in period 1961-2010; the statistics from the left to right represent QL-1.5*IRQ (the left whisker), 25% quartile, median, mean (the plus sign), 75% quartile, QU+1.5*IRQ (the right whisker); outliers (circles) are the points that fall below QL-1.5*IRQ or above QU+1.5*IRQ, where IRQ is the interquartile range (the difference between the first and the third quartiles), QL and QU are the values of the lower and upper quartiles, respectively.

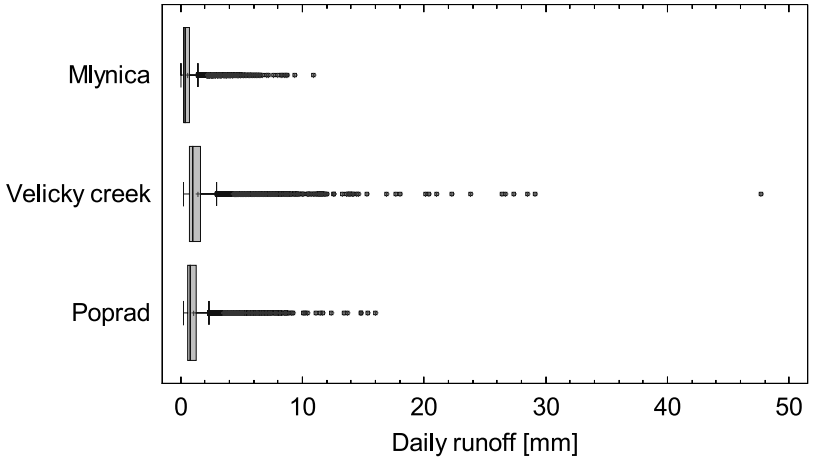

Fig. 4. Box-Whisker plot of runoff in the upper Poprad river subcatchments in hydrological years 1970–2010 (Mlynica, Velicky creek) and 1970–2009 (Poprad-Matejovce); descriptions of individual parts of the graphs are given in Fig. 2.

the stations (Table 3). Median values were lower than the means. Station StP seems to have comparatively less precipitation considering its altitude.

Figure 3 shows that 75% of daily precipitation (the 3rd quartile) was below 10 mm. Moderate precipitation between 10–20 mm was still relatively frequent at all stations. Higher daily precipitation in range from 20 to 30 mm and above 30 mm, respectively was less frequent – from statistical point of view these values appeared as outliers. Maximum daily precipitation was close to 150 mm. Such an extreme value was observed only at two stations (TJ, SkP). Maximum precipitation at other four stations (LS, TL, PP, StP) ranged from about 90 mm to about 110 mm. TJ is the only station where daily precipitation above 110 mm was observed more than once. This is consistent with the results published by *Cebulak et al. (2000)* and *Faško et al. (2000)*, focused on extreme precipitation events and daily precipitation maxima, respectively. Both concluded that events with precipitation equal or higher than 100 mm are rare. Such precipitation was usually observed in mountainous region at the border between Poland and Slovakia.

Table 3. Summary statistics of daily precipitation (dP) for period 1961–2010 and polynomial regressions of mean, 95p and 99p with altitude

Site	Altitude H [m a.s.l.]	dP > 0 mm rel. freq. [%]	q1	median	mean	q3	95p	99p	Maximum
LS	2635	59	1.4	4.1	6.9	9.3	23.5	41.2	92
SkP	1778	56	0.8	3.1	6.5	8.3	24.8	43.7	145
TL	827	46	0.8	2.4	4.7	6.0	17.3	30.4	83
PP	694	42	0.5	1.6	3.9	4.8	15.6	28.4	79
StP	1354	57	0.7	2.4	4.9	6.4	17.9	30.9	101
TJ	1030	52	1.2	3.5	6.9	8.7	24.4	50.0	147

Skalnatá dolina valley (LS, SkP, TL, PP) elevation profile: relation between x = H and y = dP			
dP statistics	Regression	R	P-value
number of dP [%]	**y = 38.08 + 0.008542*x**	**0.9614**	**0.0386**
q1	y = 0.32 + 0.000376*x	0.9034	0.0966
median	**y = 1.12 + 0.001133*x**	**0.9680**	**0.0320**
mean	y = 3.28 + 0.001497*x	0.9479	0.0521
q3	**y = 3.84 + 0.002198*x**	**0.9661**	**0.0339**
95p	**y = 3.29 + 0.021259*x - 5.157E-6*x^2**	**0.9999**	**0.0077**
99p	y = 7.07 + 0.036187*x - 8.810E-6*x^2	0.9984	0.0557

R – correlation coefficient
P-value < 0.05 – statistically significant relationship

Prevailing flow of humid air originated over Atlantic Ocean invokes more effective formation of precipitation on the northern slopes of the High Tatra Mts. compared to the southern slopes (*Konček et al., 1974*). Summer heavy rainfalls over the High Tatra Mts. were formed in air masses controlled particularly by the northeastern cyclonic situation (NEc) and other air circulation types as eastern cyclonic situation (Ec), wake of low pressure (Bp) and southwestern anticyclonic situation (*Bičárová and Čepčeková, 2011*). Windward position of the TJ station is probably the reason for higher precipitation maxima compared to the SP, LS or StP stations. It is in agreement with observation of maximum daily precipitation in Poland (*Ustrnul and Czekierda, 2009*) that shows high frequency of daily precipitation exceeding 100 mm in the Polish part of the mountains. Absolute daily maxima 232 mm and 300 mm recorded at the Kasprowy Wierch mountain and the nearby station Hala Gasienicova, respectively in June 1973 represent the highest recorded daily precipitation in Poland. Both stations are situated in the Western Tatra Mts. that form one mountain range with the High Tatra Mts. Substantially lower daily precipitation (between 47 and 103 mm) occurred at the same time in the Slovak High Tatra Mts.

Daily runoff in the studied catchments was most frequently below 1 mm (Fig. 4). The observed range was smallest in the Mlynica catchment, which has the lowest mean altitude. It may be caused by comparatively smaller precipitation in the western part of the High Tatra Mts. (precipitation at station StP was mentioned above). The highest number of outliers as well as the highest observed daily runoff (47.7 mm) occurred in the Velicky creek catchment.

Statistics of daily precipitation show high correlations with altitude (Table 3). Statistically significant correlations with the altitude were found for the relative frequency of days with precipitation, median and 3^{rd} quartile of daily precipitation. Polynomial regressions for 95^{th} and 99^{th} percentiles reflect slight decrease of high dP values in altitude between 1800–2600 m a.s.l. Statistics of the daily runoff are given in Table 4. The highest values of all statistics were found in the Velicky creek catchment that has the highest mean altitude.

The IHA software calculated regression parameters for 67 flow statistics. When we applied the criteria given in the Methodology, we did not find any strong statistically significant trend for the calculated statistics.

Table 4. Summary statistics of daily runoff; hydrological years 1970–2010 for the Mlynica and the Velicky creek catchments, hydrological years 1970–2009 for the Poprad-Matejovce catchment

Catchment	Statistics of daily runoff [mm]						
	q1	median	mean	q3	95p	99p	Maximum
Mlynica	0.2	0.4	0.6	0.7	1.7	3.3	10.9
Velicky creek	0.7	1.0	1.4	1.6	3.5	6.5	47.7
Poprad-Matejovce	0.6	0.8	1.1	1.3	2.6	4.5	16.0

4.3. Occurrence and duration of dry and wet periods

As expected, the total number of dry and wet periods that varied between 540 and 650 was similar for individual decades and precipitation stations (Table 5). The longest period without precipitation that lasted 36 days was observed at the lowest station PP. The longest wet period (43 days) occurred at the highest station LS. Not-pronounced changes were found for the short-term dry and wet periods. Dry/Wet share for middle-term and long-term periods suggest more frequent occurrence of wet periods at stations situated in altitude above 1000 m a.s.l. (LS, SkP, StP, TJ). Substantial increase of decadal precipitation during the last decades was observed at these stations. The increase of decadal precipitation may be associated with higher frequency of the long-term wet periods in the higher layer of the lower troposphere that is illustrated in Fig. 5. The correlation coefficient ($R = 0.913$) indicates a strong relationship between the variables.

Durations of extremely low flows, and small and large floods in individual decades are given in Table 6. Decrease of duration of extremely low flows in the last two decades was observed in two of the three catchments. On the contrary, significant increase occurred in the third catchment (Mlynica) in the last decade. Number of days with flows classified as small floods in the Velicky creek and the Poprad-Matejovce catchments significantly increased in the last decade. The increase should not be attributed to the windfall that hit the High Tatra Mts. in November 2004, because quite many small floods occurred also before (in June–July 2001, July–August 2002, July–August 2004). Small floods after the windfall occurred in March–July 2005 (snow-rich winter), March–July 2006 (long winter with untypical simultaneous snowmelt in both mountains and river valley), July-August 2008 and in April 2010 (snowmelt period after a snow-poor winter).

Large floods did not seem to be the best descriptors in the studied catchments, because they occurred very rarely. There were two such events in the Mlynica catchment (October–December 1974, July–August 2001). Three events were observed in the Velicky creek catchment (July 1973, July–

Table 5. Characteristics of dry and wet periods for precipitation stations (1961–2010)

site	decade	Dry periods[1]					Precipitation	Wet periods[1]				
		ST	MT	LT	total	max[2]	[mm/decade]	ST	MT	LT	total	max[2]
LS	1961-1970	546	43	11	600	24	16475	505	74	22	601	25
	1971-1980	500	50	17	567	20	14756	460	83	23	566	22
	1981-1990	504	47	8	559	21	14742	431	106	22	559	31
	1991-2000	498	53	3	554	13	17763	422	94	39	555	34
	2001-2010	513	38	8	559	13	19908	434	81	43	558	25
SkP	1961-1970	532	55	15	602	21	13024	515	72	15	602	16
	1971-1980	500	44	16	560	25	12753	438	98	24	560	19
	1981-1990	529	51	13	593	23	12526	477	102	14	593	24
	1991-2000	525	50	5	580	19	13748	464	83	34	581	23
	2001-2010	522	51	12	585	17	15194	472	83	29	584	24
TL	1961-1970	535	66	26	627	23	7954	571	52	4	627	13
	1971-1980	509	70	28	607	34	8098	556	46	6	608	22
	1981-1990	485	97	25	607	22	7353	563	38	6	607	20
	1991-2000	550	74	15	639	22	7739	583	48	8	639	18
	2001-2010	531	70	19	620	29	8622	551	60	8	619	23
PP	1961-1970	524	68	32	624	36	5933	585	38	2	625	9
	1971-1980	501	75	26	602	28	5956	550	46	5	601	16
	1981-1990	522	86	22	630	26	5484	590	37	4	631	13
	1991-2000	525	90	19	634	26	5832	592	41	1	634	11
	2001-2010	541	83	19	643	26	6706	602	37	3	642	19
StP	1961-1970	527	51	7	585	21	9898	474	84	27	585	23
	1971-1980	488	41	15	544	26	9808	409	111	24	544	20
	1981-1990	509	56	17	582	17	9094	475	88	19	582	21
	1991-2000	508	62	5	575	18	10878	470	73	33	576	26
	2001-2010	515	54	11	580	22	11583	466	83	30	579	25
TJ	1961-1970	570	66	13	649	22	12161	583	53	12	648	31
	1971-1980	474	79	25	578	26	12364	508	55	15	578	20
	1981-1990	544	65	11	620	18	12341	526	79	15	620	22
	1991-2000	536	51	12	599	15	13507	502	80	18	600	25
	2001-2010	545	59	13	617	22	15127	528	70	18	616	25

[1] number of periods per decade; ST – short-term period (duration 1-5 days); MT – middle-term period (duration 6-10 days); LT – long-term period (more than 10 days)
[2] duration of the longest period in days in a decade

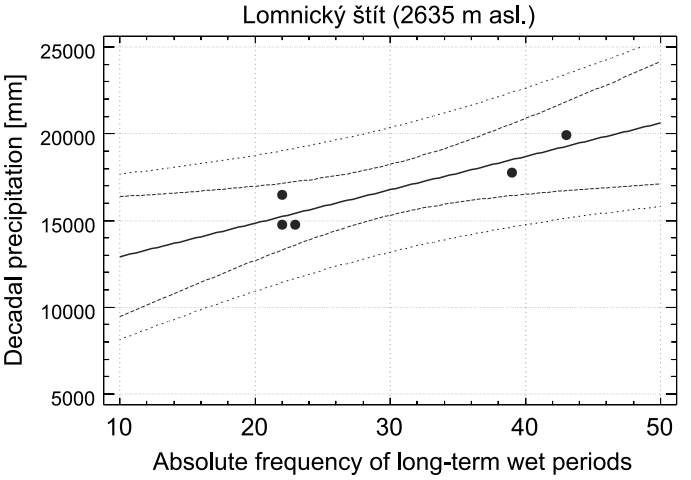

Fig. 5. Simple regression between the frequency of the long-term wet periods and decadal precipitation.

August 2001 and May–August 2010). Two events classified as large floods were observed in the Poprad-Matejovce catchment (July–August 1997, July–August 2001). The event in May-August 2010 most probably occurred at Poprad-Matejovce too, but since the measurements finished in 2009, the measured data were not at disposal. It is obvious that an apparent signif-

Table 6. Numbers of days with flows classified as extremely low, small floods and large floods; the definitions of flow characteristics are given in methodology

Catchment	Decade	Extremely low	Small floods	Large floods
Mlynica	1971-1980	283	166	80
	1981-1990	360	229	0
	1991-2000	282	141	0
	2001-2010	456	179	27
Velicky creek	1971-1980	311	109	28
	1981-1990	625	90	0
	1991-2000	360	144	0
	2001-2010	173	234	122
Poprad-Matejovce	1971-1980	287	195	0
	1981-1990	523	134	0
	1991-2000	323	51	38
	2001-2009	271	176	33

icant increase between decade 1991–2000 and 2001–2010 is caused just but the occurrence of one large flood event in the extremely wet spring 2010. Thus, such a change should not be classified as a trend.

Evaluation of precipitation data series according to the IWSS criteria shows a significant increase of the number of potentially dangerous daily precipitation, i.e. reaching 40–60 mm (Fig. 6). It may be related to the increase of precipitation at the highest altitudes. The increase of precipitation at higher altitudes may be the reason of increase of flows classified as small floods in the last two decades. Occurrence of days with precipitation exceeding 60 mm, i.e. potentially large or enormous hazard consequences suggested irrelevant changes, although approximately twofold increase of the absolute frequency was recorded at stations SkP and TJ in last two decades (Fig. 6). The highest number (4) of daily precipitation connected with the extreme risk, i.e. more than 90 mm was observed at station TJ during decade 2001–2010. Thus, the area close to the Polish-Slovak border is probably the most vulnerable area in the High Tatra Mts.

5. Conclusions

Frequent occurrence of extreme weather events reported over the world during last years is a serious reason for regional research of the associated potential hazard. It is generally acknowledged that mountains are particularly vulnerable to possible changes of weather patterns. Hydrological research performed near the study area showed that runoff response of the small mountain catchments in the warm period of a year (i.e. the one associated with precipitation maximum) primarily depends on the amount of precipitation (*Kostka and Holko, 2003*). The results of this study indicated an increased precipitation at higher altitudes in the High Tatra Mts. It may be related to a significant increase in the number of days with daily precipitation 40–60 mm and more frequent occurrence of the long-term wet periods during last two decades in the upper layer of lower troposphere. Significant increase of small flood events found for two catchments in the last decade (2001–2010) may be linked to it as well.

Simultaneous analysis of the time series of meteorological and hydrological data is useful in extending knowledge on hydrological response of

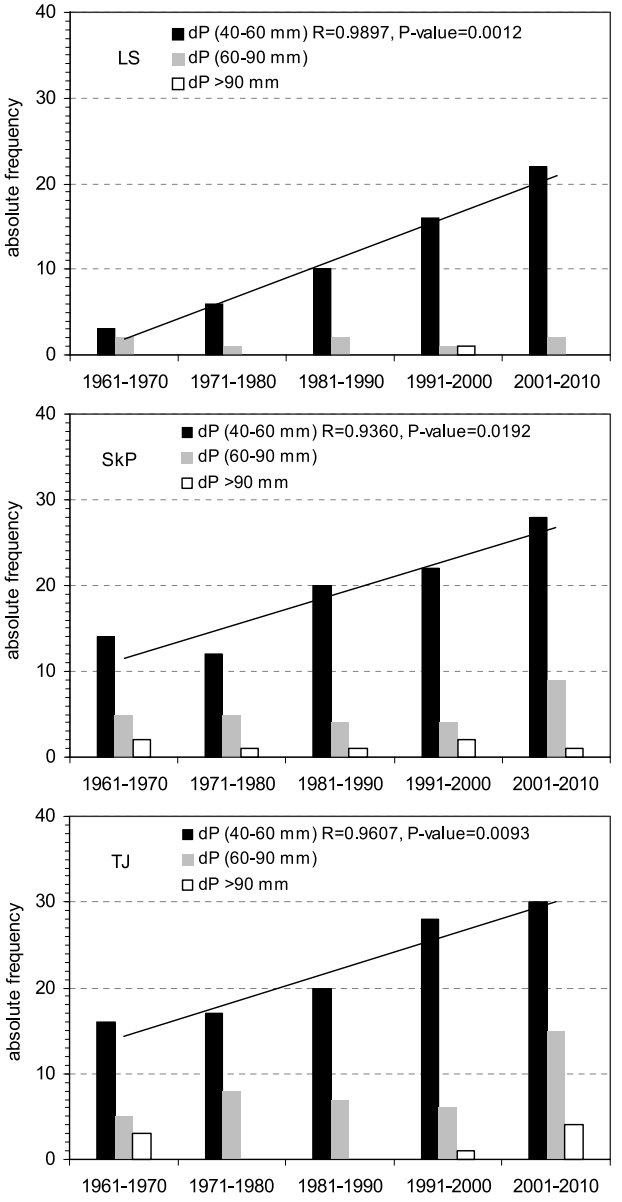

Fig. 6. Decadal changes of extreme and potentially dangerous rainfalls at the most sensitive sites LS, SkP and TJ for warm seasons (MJJASO) of period 1961–2010 (line – statistically significant increase).

mountain catchments. However, the results should not be extrapolated beyond the study period. Dry year of 2011 that was not analysed here would for example not negligibly change the statistics of the dry periods.

Acknowledgments. This research was supported by the Grant Agency of the Slovak Republic under the projects VEGA No. 2/0079/11, 2/0042/11, and APVV No. 0429-12. The authors are grateful to the Slovak Hydrometeorological Institute for providing data.

References

Alexandersson A., 1986: A homogeneity test applied to precipitation data. Journal of Climatology, **6**, 661–675.

Allamano P., Claps P., Laio F., 2009: Global warming increases flood risk in mountainous areas. Geophys. Res. Lett., **36**, L24404, doi:10.1029/2009GL041395.

Bičárová S., Čepčeková E., 2011: Decadal precipitation totals (1961–2010) in the High Tatras region and occurrence of atmospheric circulation types. Scientific conference Bioclimate – source and limit of social development. Conference proceedings, Topoľčianky, Slovakia, 6th–9th September 2011.

Birsan M. V., Molnar P., Burlando P., Pfaundler M., 2005: Streamflow trends in Switzerland. Journal of Hydrology, **314**, 312–329.

Blöschl G., Montanari A., 2010: Climate change impacts – throwing the dice? Hydrol. Process., **24**, 374–381, doi:10.1002/hyp.7574.

Cebulak E., Faško P., Lapin M., Šťastný P., 2000: Extreme precipitation events in the Western Carpathians. Prace Geograficzne, **108**, 117–124.

Ceglar A., Črepinšek Z., Zapanc V., Kajfež-Bogataj L., 2009: Evaluation of the rainfall characteristic for a mountainous location in western Slovenia. Meteorological Journal, **12**, 4, 157–161.

Cunderlik J. M., Ouarda T. B. M. J., 2009: Trends in the timing and magnitude of floods in Canada. Journal of Hydrology, **375**, 471–480.

EEA – European Environment Agency, 2005: Vulnerability and adaptation to climate change in Europe. Technical report, 7.

Faško P., Lapin M., Šťastný P., Vivoda J., 2000: Maximum daily sums of precipitation in Slovakia in the second half of the 20th century. Prace Geograficzne, **108**, 131–138.

Firat M., Dikbas F., Cem Koç A., Gungor M., 2010: Missing data analysis and homogeneity test for Turkish precipitation series. Sãdhanã **35**, Part 6, 707–720.

Guha-Sapir D., Vos F., Below R., Ponserre S., 2011: Annual Disaster Statistical Review 2010: The Numbers and Trends. Centre for Research on the Epidemiology of Disasters, Brussels, http://www.cred.be/sites/default/files/ADSR_2010.pdf

Halmová D., Pekárová, P., 2011: Statistical evaluation of the extreme flood and drought changes in the Belá river basin. Influence of Anthropogenic Activities on Water Regime of Lowland Territory. Physics of Soil Water, Vinianske jazero Lake, May, 17–19, 2011, Slovak Republic.

Holko L., Herrmann A., Kulasova A., 2006: Changes in runoff regimes in small catchments in Central Europe: Are there any? Climate Variability and Change – Hydrological Impacts. (Proceedings of the 5th Friend World Conference held at Havana, Cuba, November 2006) IAHS Publ., 308, 508–513.

Holko L., Hlavatá H., Kostka Z., Novák J., 2009: Hydrological regimes of small catchments in the High Tatra Mountains before and after the large wind-induced deforestation. Folia Geographica ser. Geographica-Physica, **XL**, 40, 33–44.

IPCC – Intergovernmental Panel on Climate Change, 2007: The Sienfic basis. `http://www.ipcc.ch/publications_and_data/ar4/wg1/en/contents.html`

IWSS – Integrated Warning Service System. Czech Hydrometeorology Institute. `http://pocasi.chmi.cz/en/`

Kang H. M., Yusof F., 2012: Homogeneity Tests on Daily Rainfall Series. Int. J. Contemp. Math. Sciences, **7**, 1, 9–22.

Konček M., Bohuš I., Briedoň V., Chomicz K., Intribus R., Kňazovický L., Kolodziejek M., Kurpelová M., Murínová G., Myczkowski S., Orlicz M., Orliczowa J., Otruba J., Pacl J., Peterka V., Petrovič Š., Plesník P., Pulina M., Smolen F., Sokolowska J., Šamaj F., Tomlain J., Volfová E., Wiszniewski W., Wit-Jozwikowa K., Zych S., Žák B., 1974: Climate of the Tatra Mountains (Klíma Tatier). VEDA – Publishing House of the Slovak Academy of Sciences, 856 p. (in Slovak).

Kostka Z., Holko L., 2003: Analysis of rainfall-runoff events in a mountain catchment. Technical Documents in Hydrology, Unesco Paris, 19–25.

Lapin M., Damborská I., Gaál L., Melo M., 2003: Possible precipitation regime change in Slovakia due to air pressure and circulation changes in the Euro-Atlantic area until 2100. Contrib. Geophys. Geod., **33**, 3, 161–189.

Mačutek J., Zahradníček P, Bičárová S., Štěpánek P., 2011: Homogenisation of precipitation data at peak mountain site Lomnický štít (1961–2010). In Bioclimate – source and limit of social development: Conference proceedings, Eds.: B. Šiška, M. Hauptvogl, M. Eliášová – Nitra: Slovak Agricultural University Nitra, ISBN 978-80-552-0640-0.

Maronna T., Yohai V. J., 1978: A bivariate test for the detection of a systematic change in mean. Journal of the American Statistical Association, **73**, 640–645.

Melo M., Lapin M., Damborská I., 2009: Shifts in Climatic Regions in the Mountain Parts of Slovakia. In: Pribullová A., Bičárová S. (Editors). Sustainable development and bioclimate, Stará Lesná, Slovakia: Geophysical Institute of the Slovak Academy of Sciences and Slovak Bioclimatological Society, 42–43.

Mudelsee M., Börngen M., Tetzlaff G., Grünewald U., 2003: No upward trends in the occurrence of extreme floods in central Europe. Nature, 425, www.nature.com/nature.

Pacl J., 1973: Hydrology of the Tatra National Park (Hydrológia Tatranského národného parku). Treatises concerning the Tatra National Park (Zborník prác o Tatranskom národnom parku), **15**, 181–238 (in Slovak).

Robson A., 2002: Evidence for trends in UK flooding. Phil. Trans. R. Soc. Lond, 360, 1327–1343.

Schmocker-Fackel P., Naef F., 2010: More frequent flooding? Changes in flood frequency in Switzerland since 1850. Journal of Hydrology, 381, 1–8.

Šamaj F., 1973: Climatic conditions in the High Tatra Mountains. Meteorological observations.(Klimatické pomery Tatier. Vývoj meteorologických pozorovaní). Treatises concerning the Tatra National Park (Zborník prác o Tatranskom národnom parku), **15**, 239–241. (in Slovak).

Štěpánek P., 2010: ProClimDB – software for processing climatological datasets. CHMI, regional office Brno (http://www.climahom.eu/ProcData.html)

The Nature Conservancy, 2009: Indicators of Hydrologic Alteration Version 7.1 User's Manual.

UN/ISDR – United Nations, International Strategy for Disaster Reduction, 2010: Strengthening climate change adaptation through effective disaster risk reduction. http://www.unisdr.org/preventionweb/files/16861_ccbriefingnote3.pdf

Ustrnul Z., Czekierda D., 2009: Atlas of extreme meteorological phenomena and synoptic situations in Poland. Instytut Meteorologi i Gospodarki Wodnej, Warszawa, ISBN 978-83-61102-22-9.

Villarini G., Smith J. A., 2010: Flood peak distributions for the eastern United States. Water Resour. Res., 46, W06504, doi:10.1029/2009WR008395.

Zhang X., Alexander L., Hegerl G. C., Jones P., Tank A. K., Peterson T. C., Trewin B., Zwiers F. W., 2011: Indices for monitoring changes in extremes based on daily temperature and precipitation data. WIREs Clim Change 2011, **2**, 851–870, doi: 10.1002/wcc.147.